

Preface

On behalf of all members of the Walter Schottky Institut of the Technische Universität München, I am pleased to present you this annual report and hope that you will find it informative and interesting. The report gives an overview of the research and teaching activities of the institute during the year 2004. As in the previous years, the efforts have been focussed on the four main areas of semiconductor electronics research:

- basic semiconductor physics combined with the development of new experimental approaches
- semiconductor materials science including the growth and manipulation of semiconductors with micro- and nanometer resolution
- biochemical semiconductor applications, and
- realization and modelling of novel semiconductor devices.

Throughout 2004, an average of 14 faculty and scientific staff members, 16 members of the administrative and technical staff, 47 doctorate candidates, 39 diploma students, and some 4 short and long term international guests belonged to the institute. 8 PhD theses, 25 diploma and 2 master theses were completed in 2004. 130 journal and conference papers, and 81 invited talks again demonstrate the scientific productivity of the institute.

2004 was a year with several considerable acknowledgements for members of the institute. Marc Tornow was awarded an independent Junior Research Group “Nanotechnology” funded by the BMBF up to 5 years. Markus C. Amann and Markus Ortsiefer (now with Vertilas GmbH) won the Karl-Heinz Beckurts prize 2004 for the invention and commercialization of the long-wavelength BTJ-VCSEL. Our PhD students Georg Steinhoff and Ulrich Rant were awarded the Chorafas prize 2004, and Felix Hofbauer received the Edison prize issued by General Electric Company. Andreas Kress and Ulrich Rant gained the Best Student Paper Awards at the ICPS in Flagstaff and the MRS meeting in San Francisco, respectively. Also, Martin Stutzmann renounced a distinguished and attractive offer by Rensselaer Polytechnic Institute, Troy, New York, which we all greatly appreciate.

The year 2004 showed an increased cooperation with industrial partners on fundamental research as well as on the transfer of device research into production. While the technological cooperation with our spin-off company Vertilas succeeded in the development of further improved single-mode long-wavelength VCSELs for sensing and communication applications, the continued successful cooperation with Rhode&Schwarz led to the realization of unique zero-bias Schottky diodes (nomen est omen!) used for precise and sensitive microwave power measurement applications. In the field of nano-biotechnology, finally, a well funded collaboration with the Fujitsu Laboratories of Europe was extended for three further years.

Let me finally thank all colleagues, collaborators, students, and post-docs for their participation and extensive work carried out in teaching and research and express my appreciation to our friends and sponsors for their continuous support and interest in our work.

1. The Walter Schottky Institut

History

The Walter Schottky Institut (WSI) is a Central Institute of the Technical University of Munich (TUM). It was founded in order to strengthen the interaction between basic physics and semiconductor electronics research and development. After the decision was made to create such an interdisciplinary research institute in early 1986 it took about two years until the new laboratories became operational in May 1988. This exceptionally short time for planning and construction of a modern institute building was made possible by the excellent cooperation between the Siemens AG, the Bavarian ministries, and the TUM.

Resources

The WSI building contains laboratories and offices with a total area of about 2400 m². It is well equipped with state-of-the-art facilities for semiconductor preparation, characterization, and device technology. The main resources are listed in the following:

Materials preparation and semiconductor technology

Epitaxy systems for GaAs, InP, GaSb, GaN/AlGaN, and SiGe based heterostructures (MBE, CBE, plasma-induced MBE, MOCVD)

Ultrahigh purity GaAs MBE machine (electron mobilities > 10 Mio cm²/Vs)

UHV evaporation equipment for SiGe on glass

Plasma-enhanced Si-CVD

Pulsed laser processing

Laboratory for surface modification / biofunctionalization

250 m² class 100 clean room facility with photolithography, e-beam lithography, reactive ion etching, metallization

Characterization and spectroscopy tools

High resolution X-ray diffraction

Atomic force microscopy

Electron microscopy and EDX equipment

Photoluminescence and Raman spectroscopy (from IR to UV)

DLTS, Optical DLTS, CV-profiling

Hall measurements and magneto-transport

FTIR spectroscopy

X-ray photoelectron spectroscopy

High frequency parameter analyzers

Electron spin resonance (ODMR, EDMR)

He³ cryostats with magnetic fields up to 15 and 17 Tesla

Special characterization facility for laser diodes

Computational facilities

High end workstations

Research groups

The WSI accommodates four research groups headed by **Gerhard Abstreiter**, **Markus-Christian Amann**, **Martin Stutzmann**, and **Peter Vogl**, with a total headcount of about 90 including scientific and technical staff, secretaries, and doctorate as well as diploma (master) students. Out of these, about 25 permanent positions are funded by TUM, while basically all the doctorate positions are financed via external research projects with external funding. The main research interests are:

- fabrication and characterization of new semiconductor materials, material combinations, as well as hetero- and nanostructures
- basic physics with emphasis on electronic and optical properties of low dimensional systems
- realization of new semiconductor devices for application in ultrafast electronics, optoelectronics, and sensors
- theory and simulation of modern semiconductor materials and devices

Experimental Semiconductor Physics I (Gerhard Abstreiter, Jonathan J. Finley):

Research projects of this group deal with various aspects of electronic and optical properties of low-dimensional, mesoscopic semiconductor structures, the heteroepitaxy of group IV and III-V semiconductors, the development of novel methods for lateral patterning and of analytical tools for the characterization of nanometer-size structures, as well as the fabrication and test of new, unconventional electronic and optoelectronic devices. Examples for basic research are optical spectroscopy of single quantum dots, cleaved edge overgrowth on GaAs, magnetotransport in ultrahigh mobility GaAs heterostructures as well as electronic transport and tunneling in edge channels and one-dimensional systems. Device and technology oriented work aims at novel concepts for charge and spin storage in quantum dots, coherent devices based on quantum dots for future quantum information technology, photonic crystal microcavities for efficient single photon sources and the test of semiconductor nanostructures for chemical/biological sensors. A new area of research is the controlled manipulation of oligonucleotides on gold surface for possible protein detection and the development of SOI based lab-on-a-chip systems.

Semiconductor Technology (Markus-Christian Amann):

The research activities in this group are concentrated on modern technologies for III-V compound semiconductors and their use for developing advanced electronic and optoelectronic devices. This comprises the development of epitaxial, patterning, microstructuring, etching and coating techniques as well as the design and fabrication of semiconductor laser diodes and other photonic components. The applied material systems are GaAs-AlGaAs, InGaAsP-InP and antimonide based compounds that are grown with molecular beam epitaxy (MBE) and chemical beam epitaxy (CBE) with an accuracy in the nanometer regime. Device structuring in the 100-nm-range is obtained by using electron-beam lithography. Reactive ion etching enables the well-defined processing of the various devices with a high

material selectivity of the etching rate. The group is also well equipped with evaporation and sputtering techniques for passivation and contacting of the devices. Among the key devices are single-mode and wavelength-tunable laser diodes for the wavelength range between 1300 and 2200 nm using lattice-matched and strained InGaAsP layers on InP substrates, InGaAsP and AlInGaAs vertical cavity surface-emitting laser diodes in the 1300-2000 nm wavelength range. Recent work also covers the development of wavelength-tunable laser diodes for wavelengths above 2 μm using antimonide based compounds and quantum cascade lasers in the range of 5 to 15 μm for gas sensing. In the field of high-frequency electronic devices, the generation of rf-output power at millimeter-wave frequencies up to 300 GHz is aspired. Active transit-time diodes as well as passive varactor structures for multipliers are investigated.

Experimental Semiconductor Physics II (Martin Stutzmann):

The work of this semiconductor physics group deals with various aspects of new and non-conventional semiconductor materials and material combinations:

- semiconductors with a wide bandgap (GaN, InGaN, AlGaN, diamond, SiC),
- disordered semiconductors (amorphous, nanocrystalline, and polycrystalline),
- advanced thin film systems (silicon-based luminescent layers, thin film solar cells, organic/anorganic heterosystems, biofunctionalized semiconductors, semimagnetic semiconductors)

Most of these material systems are prepared by suitable deposition techniques (MBE, Plasma-enhanced CVD, e-beam evaporation, sputtering). Their efficient optimization is based on the large pool of structural, optical, and electrical characterization techniques available in our institute. Complementary to the usual spectroscopic techniques we have developed and employ a variety of highly sensitive methods which enable us to study in particular the influence of defects on the electronic performance of materials and devices. Such techniques include subgap absorption spectroscopy, optically induced capacitance spectroscopy and, in particular, modern spin resonance techniques which are applied to various materials systems and devices for spintronics.

In addition to the preparation and characterization of new semiconductor materials we also work on the modification and processing of semiconductors with pulsed high power laser systems (laser-crystallization, holographic nanostructuring, laser-induced etching) and investigate the potential of new material systems for novel device structures. Recent examples include nanostructured thin film solar cells, high electron mobility transistors based on AlGaN/GaN heterostructures, as well as UV-detectors, sensors and biosensors.

Theoretical Semiconductor Physics (Peter Vogl):

The activity of this group focuses on the theoretical study of structural, electronic and optical properties of semiconductors. The work deals with mesoscopic structures, new materials, and novel devices, in the attempt to understand their basic physics and to predict their

behavior. The research conducted in the group aims at the development of theoretical tools which can support present experimental activities and propose new ideas and solutions for the future, as indicated by the strong interaction with industrial laboratories and with engineering university departments. Sophisticated quantum mechanical calculations are used for determining the electronic structures and the optical properties of a variety of semiconductor materials and systems. The information from such fundamental studies constitute the basis for the analysis of the transport properties of such materials and for the development of reliable numerical tools for device modeling. Recent activities in this group include ab-initio studies of spin devices, prediction of novel magnetic field effects, development of multiscale methods for film growth, and the design and modeling of semiconductor based quantum information devices.

The research activity of the institute thus covers a wide spectrum from basic physics in low-dimensional semiconductor structures to the development of novel or improved electronic, optoelectronic and sensor devices based on semiconductor hetero- and nanostructures. The close collaboration between the different groups and the availability of various experimental techniques are the essential basis for the successful development of novel semiconductor devices. Close contacts with industrial partners have also proven to be very fruitful and stimulating in developing new ideas and in following new directions which may be relevant for future applications.

Apart from the extensive research activities all groups are involved in teaching within their respective departments. Besides the usual teaching responsibilities in undergraduate and graduate courses, special emphasis is put on the education of diploma and doctoral students in the physics and technology of present and future devices and of low dimensional semiconductor structures.

Optical initialization and readout of electron spin in self-assembled semiconductor quantum dots

Miro Kroutvar, Dominik Heiss*, Max Bichler, Dieter Schuh, Gerhard Abstreiter, and Jonathan J. Finley

We have investigated the potential to optically generate individual *electrons* in self-assembled quantum dots and program their spin orientation via the polarization of the laser excitation source.¹ The results of these measurements demonstrate that spin relaxation in QD nanostructures is strongly suppressed when compared with higher dimensional systems and, moreover, show that spin relaxation is driven by spin-orbit coupling of the Zeeman levels mediated by single phonon scattering processes.

Fig. 1 shows the schematic structure and operating principles of the devices investigated. A single layer of self assembled InGaAs QDs is embedded in the intrinsic region of a p-i-Schottky photodiode.^{1,2} In the charge storage condition (Fig. 1a), a negative potential is applied to the semitransparent Schottky gate with respect to the p-contact leading to a large static electric field along the growth axis of the dots. Single electron hole pairs are generated by selective optical excitation of the QD ground states. The spin orientation of these excitons is determined

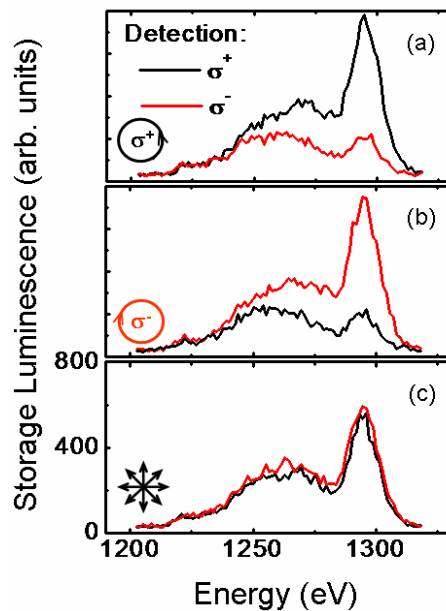


Fig. 2: Example spin storage spectra

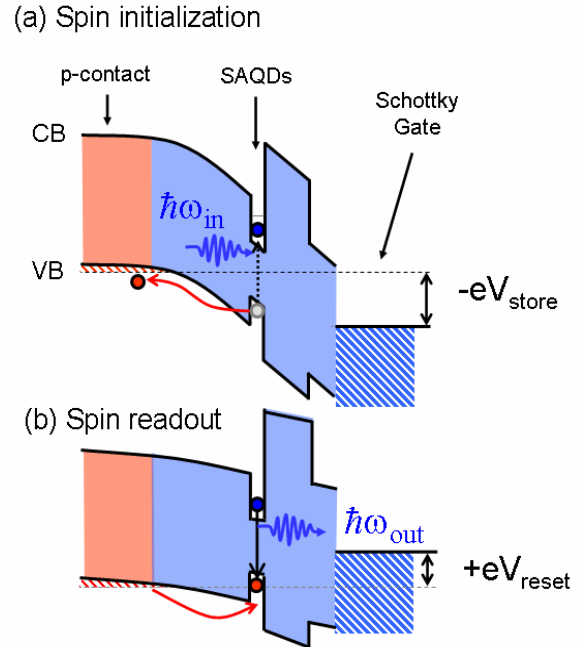


Fig. 1: Operating principle of the spin memory devices investigated

via the optical polarization due to the QD transition selection rules. Excitation with circularly polarized light with σ^+ helicity creates excitons with total angular momentum $J_x = S_e + J_h = +1$ ($S_e = -1/2$, $J_h = +3/2$) whereas σ^- excitation generates $J_x = -1$ ($S_e = +1/2$, $J_h = -3/2$). Whilst holes readily escape from the QDs by tunneling into the p-contact, electron escape is prevented due to the much smaller tunneling probability through the AlGaAs barrier. This process leaves single electrons with spin orientation $S_e = -1/2$ ($+1/2$) in the dots following σ^+ (σ^-) excitation. The distribution of electron spins in the QD sub-ensemble is tested after a storage time Δt by forward biasing the Schottky junction. Holes then drift into the negatively charged dots and generate a time delayed electroluminescence (EL) signal with a spectral distribution that directly reflects the spectral distribution of charges and polarization corresponding to their spin orientation.

*phone: +49-89-289-12717, fax: +49-89-3206620, email: heiss@wsi.tum.de

We performed spin storage measurements with circular polarization discrimination in both excitation and detection channels and large static magnetic fields applied parallel to the QD growth axis. Selected examples of these measurements are presented in Figs 2a and 2b. After spin initialization with circularly polarized light the storage EL-spectrum consists of a peak (labeled-R in Fig. 2) close to the excitation energy corresponding to resonantly generated electron spins. The storage EL signal in the vicinity of peak-R is found to be predominantly copolarized with a degree of circular polarization $\sim 65\%$ as shown by Figs 2a and 2b. This indicates that the spin orientation of the optically generated single electrons is preserved over the $\Delta t = 2\mu\text{s}$ storage time. In contrast, following excitation with randomly linearly polarized light (Fig. 2c) we observe zero degree of circular polarization demonstrating that spin alignment due to inter-Zeeman level thermalisation does not occur over such short storage times.² These results show a pronounced “polarization memory” effect for both spin orientations arising from the reversible transfer from optical polarization to electron spin orientation, spin storage for $\Delta t = 2\mu\text{s}$ and back-transfer from spin orientation to optical polarization. Fig. 3 shows the temporal dynamics of the spin storage EL, recorded at $T = 1\text{K}$ and $B = 8\text{T}$ and detected with σ^- (open squares) or σ^+ (open circles) discrimination. Data following excitation of the lower (Fig. 3a) or upper (Fig. 3b)

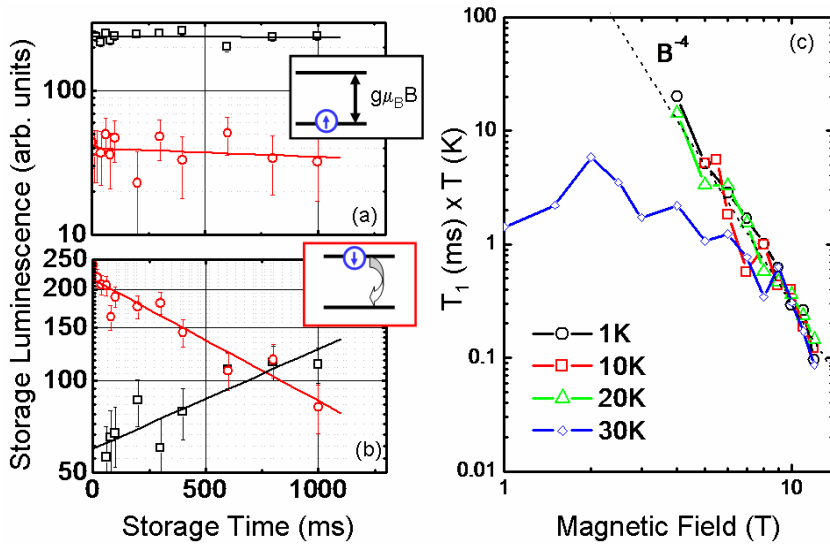


Fig 3: Spin dynamics following creation of spins in lower (a) or upper (b) Zeeman levels. (c) Spin relaxation times measured by time resolved EL at $T = 1\text{-}30\text{K}$

magnetic field and temperature to determine the mechanism responsible for spin flip scattering. The results of these investigations are presented in Fig. 3c on a double logarithmic representation. At $T = 1\text{K}$ and $B = 4\text{T}$, the spin lifetimes are found to be extremely long ($T_1 = 20 \pm 6\text{ms}$), decreasing with increasing field according to a power-law $T_1 \propto B^{-4.4 \pm 0.2}$. Furthermore, we observed a linear temperature dependence (Fig. 3c) confirming that spin relaxation is due to spin-orbit interaction mediated by single piezoelectric phonons.³

1 M. Kroutvar, Y. Ducommun, D. Heiss, D. Schuh, M. Bichler, G. Abstreiter and J. J. Finley. Nature **432**, 81 (2004)

2 Y. Ducommun, M. Kroutvar, M. Reimer, M. Bichler, D. Schuh, G. Abstreiter, and J. J. Finley. Appl. Phys. Lett. **85**, 2592 (2004)

3 A. V. Khaetskii and Y. Nazarov. Phys. Rev. B **64** 125316-1 (2001)

7. Invited Talks

Gerhard Abstreiter

1. *Novel semiconductor nano-devices: control of single charges, spins and photons*
Seminar, VDE VDI, Arbeitskreis Mikroelektronik, Mikro- und Feinwerktechnik
Munich, Germany (2.2.2004)
2. *Optical control of charge and spin in semiconductor quantum dots*
Research Conference on “Advancing Frontiers of Optical and Quantum Effects in
Condensed Matter”, Trieste, Italy (12.-15.5.2004)
3. *Novel semiconductor nano-devices: control of single charges, spins and photons*
EMRS 2004 Spring Meeting, Strasbourg, France (24.-28.5.2004)
4. *Optical control of charge and spin in semiconductor quantum dots*
Intern. Symposium on “Quantum Hall Systems and Quantum Materials”
Hamburg, Germany (22.-24.9.2004)
5. *Single charge, spin, exciton and photon in self assembled quantum dots*
Spin QSIT Meeting, Castasegna, Switzerland (4.-6.10.2004)
6. *Control of charge and spin in quantum dots*
Quantum Heterostructures Symposium, TU Vienna, Austria (8.10.2004)
7. *Optical control of single charge and spin in self-assembled semiconductor
quantum dots*
FNST Workshop, Harvard University, USA (25.-26.10.2004)
8. *Novel semiconductor nanostructures and nanodevices fabricated by cleaved edge
overgrowth*
University of Tokyo, Komaba, Japan (17.11.2004)
9. *Dynamic switching of DNA on a metal surface – novel perspectives for biosensing
applications*
AIST, Diamond Center, Tsukuba, Japan (18.11.2004)
10. *Single dot spectroscopy and optical control of charge, spin and photon in self-
assembled quantum dots”*
NTT Basic Research Lab., Atsugi, Japan (19.11.2004)
11. *Dynamic switching of DNA on gold-novel perspectives of biosensing applications*
University of Tokyo, Komaba, Japan (22.11.2004)

12. *Optoelectronic control of single charge, spin and photon in semiconductor quantum dots*
University of Tokyo, Hongo, Japan (24.11.2004)
13. *Single dot spectroscopy and electron spin storage in self-assembled quantum dots*
University of Tokyo, Komaba, Japan (25.11.2004)
14. *Special lecture on “Quantum Hall effect and fractional Quantum Hall effect”*
University of Tokyo, Komaba, Japan (25.11.2004)
15. *Novel semiconductor devices for quantum information technology*
Fujitsu Laboratories, Atsugi, Japan (26.11.2004)
16. *Optical properties of quantum dots – from fundamentals to recent topics*
University of Tokyo, Komaba, Japan (29.11.2004)
17. *Spin storage and spin lifetime in self-assembled semiconductor quantum dots*
Tokyo Institute of Technology, Japan (30.11.2004)
18. *Control of single charges, spins and photons in novel quantum dot devices*
11th Advanced Heterostructure Workshop, Hawaii, USA (05.-10.12.2004)

Markus-Christian Amann

1. *Single-mode and tunable VCSELs for sensing applications at 1.3 - 2 μ m*
Photonics Europe, Strasbourg, France (29.-30.4.2004)
2. *Einmodige und durchstimmbare VCSEL bei 1.3 - 2.05 μ m: Ein Durchbruch für die optische Sensorik*
Technische Universität Wien, Austria (28.05.2004)
3. *Laserdioden für die optische Kommunikationstechnik*
105. Tagung der Deutschen Gesellschaft für angewandte Optik, Bad Kreuznach, Germany (1.-5.6.2004)
4. *Single-mode and tunable VCSEL for the 1.3 - 2.0 μ m wavelength range*
MIOMD-VI, St. Petersburg, Russia (28.6.-1.7.2004)
5. *Anwendungen in der Gasanalyse*
“Halbleiterlichtquellen”, OTTI-Profiforum, Regensburg, Germany (18.-19.10.2004)
6. *Applications of and advances in long-wavelength (>2 μ m) lasers*
19. International Semiconductor Laser Conference, Matsue-shi, Simane, Japan (21.-25.10.2004)

Martin S. Brandt

1. *Halbleiter für die Bioelektronik und Spintronik*
Seminar, Universität Erlangen, Germany (29.1.2004)
2. *Mn in GaN: Prospects for carrier-induced ferromagnetism in group-III nitrides*
German-Polish Workshop on Physics and Technology of Nitride Semiconductors,
Berlin, Germany (1.-3.3.2004)
3. *Ferromagnetische Halbleiter: Ordnung durch bewegliche Ladung*
Seminar über neuere Arbeiten der Physik, Universität Marburg, Germany
(10.5.2004)
4. *Detection of spin resonance via electronic transport*
Nanoscience Seminar, Technical University Delft, The Netherlands (2.6.2004)
5. *Ferromagnetische Halbleiter: Ordnung durch bewegliche Ladung*
Physikalisches Kolloquium, Universität Giessen, Germany (7.6.2004)
6. *Beeinflussung der magnetischen Eigenschaften von GaMnAs durch Wasserstoff und elektrische Felder*
Seminar, Universität Regensburg, Germany (22.6.2004)
7. *Ferromagnetische Halbleiter: Ordnung durch bewegliche Ladung*
Seminar, Hahn-Meitner-Institut Berlin-Adlershof, Germany (24.6.2004)
8. *Hydrogen control of ferromagnetism in magnetic semiconductors*
27th International Conference on the Physics of Semiconductors, Flagstaff, USA,
(25.-30.7.2004)
9. *Spinabhängiger Transport: Elektrische Detektion magnetischer Resonanz*
Seminar, Universität Leipzig, Germany (18.10.2004)

Martin Eickhoff

1. *Chemical and biochemical sensing with group III-nitride devices*
Seminar, Lehrstuhl für Mikrosensorik und Mikrofluidik, Universität des
Saarlandes, Saarbrücken, Germany (3.5.2004)
2. *Semiconductor biosensors*
“Soft Matter Meets Solids – Perspectives in Multidisciplinary Research”,
Workshop organized by SFB 563, Donaustauf, Germany (21.5.2004)
3. *Properties and applications of AlGaIn/GaN solution gate field effect transistors*
EMRS Fall-Meeting, Warsaw, Poland (7.9.2004)

4. *Chemical sensing with wide bandgap semiconductors*
“Nanostructured and Advanced Materials for Applications in Sensor, Optoelectronic and Photovoltaic Technology”, NATO Advanced Study Institute, Sozopol, Bulgaria (6.9.-17.9.2004)
5. *Basics and applications of AlGaIn/GaN solution gate field effect transistors*
Seminar, Ångström Laboratories, Uppsala University, Sweden (15.11.2004)

Jonathan Finley

1. *Probing charge and spin states in InGaAs self-assembled quantum dots*
Intern. Conference on Semiconductor Physics, Jaszowiec, Poland (3.-5.5.2004)
2. *Physics of semiconductor quantum dot nanostructures*
MPQ Kolloquim, Garching, Germany (18.5.2004)
3. *Semiconductor artificial atoms*
Münchner Physik Kolloquim LMU, München, Germany (7.6.2004)
4. *Ultra long electron spin lifetime in semiconductor quantum dots*
Intern. Workshop on Solid State Quantum Information Processing(QIP2004), Herrsching, Germany (13.-17.9.2004)
5. *Charge and spin excitations in semiconductor quantum dots*
EQUONT-3, International Conference, University of Cambridge, U.K. (19.-23.9.2004)
6. *Controlling charge and spin states in semiconductor quantum dots*
MIQIP 2004 Workshop on Quantum Optics, Ringberg Castle, Germany (21.-24.9.2004)
7. *An optically programmable quantum dot spin memory*
Seminar, Universität Linz, Austria (22.11.2004)
8. *Quantum dot nanostructures for solid state quantum optics*
Seminar, ETH-Zürich, Switzerland (2.12.2004)

Matthew Grayson

1. *Introducing the bent quantum well: Quantum Hall physics in a two-dimensional system bent by 90°*
Seminar, Cambridge University, United Kingdom (26.1.2004)
2. *Momentum resolved tunnel spectroscopy of quantum Hall edges*
Mauterndorf Winterschool, Austria (17.2.2004)

3.-7. *Bending the quantum Hall effect by 90°: Evidence for a one-dimensional system with attractive interactions*

Seminar, Max-Planck-Institut, Stuttgart, Germany (9.6.2004)

Seminar, University of Geneva, Switzerland (6.7.2004)

Seminar, University of Tokyo, Japan (16.8.2004)

Seminar, RIKEN Laboratories, Japan (23.8.2004)

Seminar, Universität Bochum, Germany (25.11.2004)

Jacek A. Majewski

1. *Semiconductor spintronics: recent achievements and prospects*
XV Ural Int. School on the Physics of Semiconductors, Ekaterinburg, Russia
(19.2.2004)
2. *Nitrides for spintronics - magnetic moments & spin lifetimes in nitrides*
E-MRS Fall Meeting, Warsaw, Poland (10.9.2004)

Markus Maute

1. *Long-wavelength VCSELs*
16th International Conference on Indium Phosphide and Related Materials,
Kagoshima, Japan, (31.5.-4.6.2004)

Ralf Meyer

1. *Langwellige Laser-Dioden für das nahe und mittlere Infrarot - Konzepte und Realisierungen*
Bayerische Laser-Seminare, Bayerisches Laser-Zentrum, Erlangen, Germany
(11.2.2004)

Sebastian Roth

1. *A new quantum wire structure realized by double cleaved-edge overgrowth*
Seminar, Universität Regensburg, Germany (12.3.2004)

Dieter Schuh

1. *GaAs (110), an interesting surface for molecular beam epitaxy*
Seminar, LMU München, Germany (19.1.2004)

2. *Dots and devices grown by molecular beam epitaxy on (110) oriented GaAs surfaces*
Seminar, University of Sheffield, UK (31.8.2004)
3. *Molecular beam epitaxy on (110) oriented GaAs surfaces*
Seminar, MPI Stuttgart, Germany (22.11.2004)

Martin Stutzmann

1. *Biofunctionalization of group-III-nitrides*
WOCSEMMAD, Pasadena, USA (17.2.2004)
2. *AlN/diamond heterojunctions*
9th Int. Conf. on New Diamond Science and Technology (ICNDST-9) Tokyo, Japan (30.3.2004)
3. *Heterostructures devices based on diamond*
Diamond Research Center Workshop, Tsukuba, Japan (31.3.2004)
4. *Hydrogen in amorphous silicon: a simple atom in a complex environment*
MRS Spring Meeting, San Francisco, USA (13.4.2005)
5. *Novel devices for bioelectronics*
Colloquium, Rensselaer Polytechnic Institute, Troy, USA (30.4.2004)
6. *AlGaN/diamond heterostructures*
E-MRS Spring Meeting, Strasbourg, France (25.5.2004)
7. *Diamond based nanoelectronics: physics and applications*
12th Int. Symposium on Nanostructures, St. Petersburg, Russia (25.6.2004)
8. *III-nitride bioelectronic devices*
IEEE Lester Eastman Conference on High Performance Devices, Troy, USA (5.8.2004)
9. *Wege in die Halbleiternanotechnologie*
NanoNetzwerkHessen, Giessen, Germany (29.9.2004)
10. *The Alexander von Humboldt Foundation*
Latin American Symposium on Solid State Physics, Havana, Cuba (7.12.2004)

Marc Tornow

1. *Molekular funktionalisierte „intelligente“ Substrate für die Nano-Biotechnologie*
Physikalisches Kolloquium, Universität Essen, Germany (4.2.2004)

2. *Surface functionalized III-V heterostructures of biosensor applications*
Lehrstuhlseminar Institut für Angewandte und Experimentelle Physik, Universität Regensburg, Germany (9.2.2004)
3. *Electro-manipulation of DNA oligonucleotide layers on gold*
WE-Heraeus-Seminar “Nano physics of DNA”, Physikzentrum Bad Honnef, Germany (22.-24.3.2004)
4. *Dynamic manipulation of oligonucleotide layers on gold*
Seminar of the Department of Chemistry, Technical University of Denmark, Lyngby, Denmark (20.8.2004)
5. *Orientation switching of DNA layers as a new detection scheme in bio-sensing*
Seminar der Material Science Group, MPI für Polymerforschung, Mainz, Germany (16.11.2004)

Alexandros Trellakis

1. *Nextnano³: A large software project for the simulation of 3D nanometer semiconductor structures*
SFB 348 Workshop, Schloss Ringberg, Tegernsee, Germany (2.3.2004)
2. *Nextnano³: Modeling nanometer-size semiconductor structures*
WE-Heraeus-Ferienkurs für Physik, Chemnitz, Germany (4.10.2004)

Peter Vogl

1. *Theory of electronic structure and optical properties in Megagauss fields*
The Xth International Conference on Megagauss Magnetic Field Generation and Related Topics, Berlin, Germany (18.-23.7.2004)
2. *Nonequilibrium electronic structure of semiconductor nano-devices*
WE-Heraeus-Ferienkurs für Physik, Technical University Chemnitz, Germany (3.-5.10.2004)
3. *Self-consistent contact Block reduction method for ballistic nanodevice*
10th International Workshop on Computational Electronics (IWCE – 10), Purdue University, West Lafayette, Indiana, USA (24.-27.10.2004)

8. Courses and Seminars

Lectures

Gerhard Abstreiter

- WS 2003/2004 Einführung in die Festkörperphysik
(Introduction to solid state physics)
- SS 2004 Festkörperphysik II (Solid state physics II)
- Halbleiterphysik II - Physik niedrigdimensionaler Systeme
(Semiconductor physics II - Low dimensional systems)
- WS 2004/2005 Sabbatical

Markus-Christian Amann

- WS 2003/2004 Werkstoffe der Elektrotechnik (Materials for electrical engineering)
- Technologie der III/V-Halbleiterbauelemente
(Technology of III/V semiconductor devices)
together with Ralf Meyer
- Optoelektronik II (Optoelectronics II)
- SS 2004 Optoelektronik I (Optoelectronics I)
- Optoelectronics
- WS 2004/2005 Werkstoffe der Elektrotechnik (Materials for electrical engineering)
- Technologie der III/V-Halbleiterbauelemente
(Technology of III/V semiconductor devices)
together with Ralf Meyer

Martin Brandt

- WS 2003/2004 Grundlagen der Halbleiterphysik
(Introduction to semiconductor physics)
- SS 2004 Halbleiterphysik II – Mikro- und Nanoelektronik
(Semiconductor physics II – Micro- and nanoelectronics)

Tutorium zu Halbleiterphysik II – Mikro und Nanoelektronik
(Tutorial Semiconductor physics II – Micro- and nanoelectronics)

WS 2004/2005 Quantum computing

Manfred Claassen

WS 2003/2004 Hochfrequenz-Elektronik (High-frequency electronics)

Partielle Differentialgleichungen in der Elektrotechnik
(Partial differential equations in electrical engineering)

Technische Elektrizitätslehre 1 (Electrical engineering 1)

SS 2004 Optische Schaltungen (Optical circuits)

Nichtlineare Schwingungsvorgänge (Nonlinear oscillations)

WS 2004/2005 Hochfrequenz-Elektronik (High-frequency electronics)

Partielle Differentialgleichungen in der Elektrotechnik
(Partial differential equations in electrical engineering)

Technische Elektrizitätslehre 1 (Electrical engineering 1)

Jonathan Finley

WS 2003/2004 Semiconductor nanoscience and technology I

SS 2004 Physics of semiconductor nanodevices II

WS 2004/2005 Semiconductor nanoscience and technology I

Matthew Grayson

WS 2003/2004 Tutorial Halbleiterphysik (Tutorial in Semiconductor physics)

SS2004 Tutorial Halbleiternanostrukturen (Tutorial in Semiconductor nanostructures)

Jacek Majewski

WS 2003/2004 Theoretical semiconductor physics I

SS 2004 Theoretical semiconductor physics II

Martin Stutzmann

WS 2003/2004 Experimentalphysik 1 (Experimental physics 1)

Micro-nanosensors-technology and applications
together with Martin Eickhoff und José Antonio Garrido Ariza

Aspects of modern semiconductor sensors
for biochemical applications
together with José Antonio Garrido Ariza und Martin Eickhoff

SS 2004 Experimentalphysik 2 (Experimental physics 2)

Biochemical sensors II
together with José Antonio Garrido Ariza

WS 2004/2005 Grundlagen der Halbleiterphysik
(Introduction to semiconductor physics)

Tutorium zu Halbleiterphysik
(Tutorial Semiconductor physics)

Bio- and nanoelectronic systems 1
together with Martin Eickhoff und Marc Tornow

Biochemical sensors
together with José Antonio Garrido Ariza

Alex Trellakis

WS 2004/2005 Theoretical physics 3 (Quantum mechanics)

Peter Vogl

WS 2003/2004 Theoretical physics 2 (Quantum mechanics and thermodynamics)

Theoretical semiconductor physics I

Computational physics
Alex Trellakis together with Walter Schirmacher

SS 2004	Theoretical solid states physics
WS 2004/2005	Theoretische Physik 4A (Quantenmechanik II) (Theoretical physics 4A (Quantum mechanics II))

Walter Schottky Seminars

Atomare Defekte und die Mechanismen der Diffusion in Halbleitern

Dr. Hartmut Bracht, Institut für Materialphysik, Universität Münster, Germany
(20.1.2004)

Single-shot read-out of a single electron spin

Prof. Lieven Vadersypen, Department of NanoScience, Technical University Delft,
The Netherlands
(27.1.2004)

Quasiparticle tunneling between fractional quantum Hall edges

Stefano Roddaro, NEST-INFM and Scuola Normale Superiore, Pisa, Italy
(3.2.2004)

Epitaxial high-k dielectrics: The example of praseodymium oxide

Prof. Dr. H. Joerg Osten, IHW, Universität Hannover, Germany
(10.2.2004)

Novel zero-resistance states induced by photoexcitation in the high mobility two-dimensional electron system

Dr. Ramesh Mani, Harvard University, Gordon McKay Laboratory of Applied Science
Cambridge, Massachusetts, USA
(2.3.2004)

Spin-splitting in symmetrical SiGe quantum wells

Dr. L. Golub, Ioffe Physico-Technical Institute, St. Petersburg, Russia
(20.4.2004)

Quantized Hall plateaus resulting from incompressible strips

Dr. Afif Siddiki, Max-Planck-Institut für Festkörperforschung, Stuttgart, Germany
(27.4.2004)

Design von Hochleistungslaserdioden für den telecom und industriellen Anwendungsbereich

Dr. Berthold Schmidt, Bokham Technology AG, Zürich, Switzerland
(11.5.2004)

Quantum Hall ferromagnetism of AlAs 2D electrons

Dr. J. G. S. Lok, Max-Planck-Institut für Festkörperforschung, Stuttgart, Germany
(18.5.2004)

EPR-spectroscopy and site-directed spin labelling: Watching membrane proteins at work

Prof. Dr. Heinz-Juergen Steinhoff, Fachbereich Physik, Universität Osnabrück, Germany
(25.5.2004)

Microscopic theory and the engineering of semiconductor lasers

Weng Chow, Sandia National Laboratories, New Mexico, z. Zt. Universität Marburg,
Germany
(24.6.2004)

Modenkopplung wechselwirkender eindimensionaler Wellenleiter

Dr. Saskia F. Fischer, Ruhr-Universität Bochum, Germany
(29.6.2004)

Modellierung von optischen Bauelementen mit der Method of Lines

Prof. Dr.-Ing. Reinhold Pregla, Allgemeine und Theoretische Elektrotechnik, Fern-
Universität Hagen, Germany
(13.7.2004)

Emergent excitonic fluids in bilayer quantum Hall ferromagnets

Stefano Luin, NEST-INFM and Scuola Normale Superiore, Pisa, Italy
(28.9.2004)

Coulomb blockade, Kondo effect and Fano resonances in three-leaded quantum dot systems

Armin C. Welker, Max -Planck-Institut für Festkörperforschung, Stuttgart, Germany
(26.10.2004)

Science citation index and impact factors: Gebrauch und Missbrauch

*Ist der Science Citation Index das ultimative Maß für die Qualität wissenschaftlicher
Veröffentlichungen?*

Claus Ascheron, Springer-Verlag, Berlin, Germany
(2.11.2004)

Atomic-scale electronics: Tunneling through dopant atoms

Sven Rogge, Kavli Institute of NanoScience, Delft University of Technology,
The Netherlands
(9.11.2004)

Electron-electron interaction in disordered multiwall carbon nanotubes

Dr. Ning Kang, Universität Konstanz, Germany
(16.11.2004)

Sapphire annealing and temperature calibration: Basic issues on high quality GaN growth

Yun Liu, Applied Semiconductor Physics Department of Microtechnology and
Nanoscience Chalmers, University of Technology, Göteborg, Sweden
(19.11.2004)

Ladungsträger-Tiefenprofile in GaMnAs

Dr. Wolfgang Limmer, Universität Ulm, Germany
(7.12.2004)

Electrically tunable mid-IR emission sources based on type II heterostructures
Dr. Yuri Vasilyev, Ioffe Physical Technical Institute, St Petersburg, Russia
(9.12.2004)

Deterministic coupling of a quantum dot to a photonic crystal nano-cavity
Dr. Mete Atature, ETH Zürich, Switzerland
(14.12.2004)

9. Selected Topics of Semiconductor Physics and Technology

Since 1997, all doctoral theses are published in the series: Selected Topics of Semiconductor Physics and Technology, eds.: G. Abstreiter, M.-C. Amann, M. Stutzmann, and P. Vogl. The following volumes appeared so far in this series:

- | | |
|---|--|
| <p>Vol. 1
Cornelia Engel
Si/SiGe basierende Phototransistoren
131 Seiten
ISBN 3-932749-01-4</p> | <p>Vol. 7
Markus Sexl
Verspannte und gitterrelaxierte In(GaAl)As Heterostrukturen
144 Seiten
ISBN 3-932749-07-3</p> |
| <p>Vol. 2
Peter Schittenhelm
Selbst-Organisation und Selbst-Ordnung in Si/SiGe-Heterostrukturen
151 Seiten
ISBN 3-932749-02-2</p> | <p>Vol. 8
Christian Obermüller
Photolumineszenzspektroskopie mit optischen Nahfeldmethoden an GaAs-Nanostrukturen
140 Seiten
ISBN 3-932749-08-1</p> |
| <p>Vol. 3
Andreas Nutsch
Selektive Epitaxie von (GaIn)(AsP) Schichtstrukturen
129 Seiten
ISBN 3-932749-03-0</p> | <p>Vol. 9
Edilson Silveira
Inelastische Lichtstreuung an niedrig-dimensionalen Halbleiterstrukturen
104 Seiten
ISBN 3-932749-09-X</p> |
| <p>Vol. 4
Peter Baumgartner
Optische und elektronische Eigenschaften lasergeschriebener GaAs-Nanostrukturen
180 Seiten
ISBN 3-932749-04-9</p> | <p>Vol. 10
Eberhard Christian Rohrer
Photoleitungs-Spektroskopie von Diamant
153 Seiten
ISBN 3-932749-10-03</p> |
| <p>Vol. 5
Walter Franz Rieger
Untersuchung der elektronischen und strukturellen Eigenschaften von GaNAIN und deren Legierungen
158 Seiten
ISBN 3-932749-05-7</p> | <p>Vol. 11
Thomas Wimbauer
Magnetische Resonanz-Untersuchungen an modernen Halbleitermaterialien
125 Seiten
ISBN 3-932749-11-1</p> |
| <p>Vol. 6
Markus Hauser
Oberflächenemittierende Laserdioden mit Mehrfachepitaxie
148 Seiten
ISBN 3-932749-06-5</p> | <p>Vol. 12
Herbert Verhoeven
Thermische Eigenschaften von CVD-Diamantschichten
154 Seiten
ISBN 3-932749-12-X</p> |

Vol. 13
Hans-Christoph Ostendorf
Trennung von Volumen- und Oberflächenrekombination in Silizium
128 Seiten
ISBN 3-932749-13-8

Vol. 14
Martin Städele
Dichtefunktionaltheorie mit exaktem Austausch für Halbleiter
202 Seiten
ISBN 3-932749-14-6

Vol. 15
Helmut Angerer
Herstellung von Gruppe III-Nitriden mit Molekularstrahlepitaxie
144 Seiten
ISBN 3-932749-15-4

Vol. 16
Wolfgang Heller
Spektroskopie einzelner Quantenpunkte in magnetischen und elektrischen Feldern
128 Seiten
ISBN 3-932749-16-2

Vol. 17
Molela Moukara
Pseudopotentiale mit exaktem Austausch
117 Seiten
ISBN 3-932749-17-0

Vol. 18
Ralph Oberhuber
Elektronische Struktur und Transport in verspannten Halbleiterschichtsystemen
110 Seiten
ISBN 3-932749-18-9

Vol. 19
Reiner Pech
High-Energy Boron-Implantation into Different Silicon Substrates
158 Seiten
ISBN 3-932749-19-7

Vol. 20
Christoph Martin Engelhardt
Zyklotronresonanz zweidimensionaler Ladungsträgersysteme in Halbleitern, Effekte der Elektron-Elektron-Wechselwirkung und Lokalisierung
317 Seiten
ISBN 3-932749-20-0

Vol. 21
Eduard Neufeld
Erbium-dotierte Si/SiGe-Lichtemitter und -Wellenleiter
136 Seiten
ISBN 3-932749-21-9

Vol. 22
Gert Schedelbeck
Optische Eigenschaften von Halbleiternanostrukturen hergestellt durch Überwachsen von Spaltflächen
154 Seiten
ISBN 3-932749-22-7

Vol. 23
Jürgen Zimmer
Optoelektronisches Verhalten von Dünnschichtbauelementen aus amorphem und mikrokristallinem Silizium
171 Seiten
ISBN 3-932749-23-5

Vol. 24
Berthold Schmidt
Leistungsoptimierung abstimmbarer InGaAsP/InP Halbleiterlaser
85 Seiten
ISBN 3-932749-24-3

- Vol. 25
Jianhong Zhu
Ordering of self-assembled Ge and SiGe nanostructures on vicinal Si surfaces
120 Seiten
ISBN 3-932749-25-1
- Vol. 26
Gerhard Groos
Herstellung und Charakterisierung von Silizium-Nanostrukturen
168 Seiten
ISBN 3-932749-26-X
- Vol. 27
Uwe Hansen
Theorie der Reaktionskinetik an Festkörperoberflächen
119 Seiten
ISBN 3-932749-27-8
- Vol. 28
Roman Dimitrov
Herstellung und Charakterisierung von AlGaIn/GaN-Transistoren
196 Seiten
ISBN 3-932749-28-6
- Vol. 29
Martin Eickhoff
Piezowiderstandsmechanismen in Halbleitern mit großer Bandlücke
151 Seiten
ISBN 3-932749-29-4
- Vol. 30
Nikolai Wieser
Ramanspektroskopie an Gruppe III-Nitriden
161 Seiten
ISBN 3-932749-30-8
- Vol. 31
Rainer Janssen
Strukturelle und elektronische Eigenschaften amorpher Silizium-Suboxide
275 Seiten
ISBN 3-932749-31-6
- Vol. 32
Martin W. Bayerl
Magnetic resonance investigations of group III-nitrides
155 Seiten
ISBN 3-932749-32-4
- Vol. 33
Martin Rother
Elektronische Eigenschaften von Halbleiternanostrukturen hergestellt durch Überwachsen von Spaltflächen
196 Seiten
ISBN 3-932749-33-2
- Vol. 34
Frank Findeis
Optical spectroscopy on single self-assembled quantum dots
156 Seiten
ISBN 3-932749-34-0
- Vol. 35
Markus Ortsiefer
Langwellige Vertikalresonator-Laserdioden im Materialsystem InGaAlAs/InP
152 Seiten
ISBN 3-932749-35-9
- Vol. 36
Roland Zeisel
Optoelectronic properties of defects in diamond and AlGaIn alloys
140 Seiten
ISBN 3-932749-36-7
- Vol. 37
Liwen Chu
Inter- und Intraband Spektroskopie an selbstorganisierten In(Ga)As/GaAs Quantenpunkten
124 Seiten
ISBN 3-932749-37-5
- Vol. 38
Christian Alexander Miesner
Intra-Valenzbandspektroskopie an SiGe-Nanostrukturen in Si
100 Seiten
ISBN 3-932749-38-3

Vol. 39

Szabolcs Kátai

Investigation of the nucleation process of chemical vapour deposited diamond films

178 Seiten

ISBN 3-932749-39-1

Vol. 40

Markus Arzberger

Wachstum, Eigenschaften und Anwendungen selbstorganisierter InAs-Quantenpunkte

236 Seiten

ISBN 3-932749-40-5

Vol. 41

Markus Oliver Markmann

Optische Eigenschaften von Erbium in Si/Si_{1-x}C_x, Si/Si_{1-x}Ge_x und Si/SiO_x Heterostrukturen

182 Seiten

ISBN 3-932749-41-3

Vol. 42

Rainer Alexander Deutschmann

Two dimensional electron systems in atomically precise periodic potential

210 Seiten

ISBN 3-932749-42-1

Vol. 43

Uwe Karrer

Schottky-Dioden auf Galliumnitrid: Eigenschaften und Anwendungen in der Sensorik

182 Seiten

ISBN 3-932749-43-X

Vol. 44

Günther Anton Johann Vogg

Epitaxial thin films of Si and Ge based Zintl phases and sheet polymers

169 Seiten

ISBN 3-932749-44-8

Vol. 45

Christian Strahberger

Vertikaler Transport und extreme Magnetfelder in Halbleitern

167 Seiten

ISBN 3-932749-45-6

Vol. 46

Jan Schalwig

Feldeffekt-Gassensoren und ihre Anwendung in Abgasnachbehandlungssystemen

125 Seiten

ISBN 3-932749-46-4

Vol. 47

Christopher Eisele

Novel absorber structures for Si-based thin film solar cells

126 Seiten

ISBN 3-932749-47-2

Vol. 48

Stefan Hackenbuchner

Elektronische Struktur von Halbleiter-Nanobaelementen im thermodynamischen Nichtgleichgewicht

213 Seiten

ISBN 3-932749-48-0

Vol. 49

Andreas Sticht

Herstellung und Charakterisierung von dünnen Silizium/Siliziumoxid-Schichtsystemen

166 Seiten

ISBN 3-932749-49-9

Vol. 50

Giuseppe Scarpa

Design and fabrication of Quantum Cascade Lasers

193 Seiten

ISBN 3-932749-50-2

- Vol. 51
Jörg Frankenberger
Optische Untersuchungen an zwei-dimensionalen Ladungsträgersystemen
158 Seiten
ISBN 3-932749-51-0
- Vol. 52
Doris Heinrich
Wavelength selective optically induced charge storage in self-assembled semiconductor quantum dots
144 Seiten
ISBN 3-932749-52-9
- Vol. 53
Nicolaus Ulbrich
Entwurf und Charakterisierung von Quanten-Kaskadenlasern und Quantenpunktkaskaden
133 Seiten
ISBN 3-932749-53-7
- Vol. 54
Lutz Carsten Görgens
Analyse stickstoffhaltiger III-V Halbleiter-Heterosysteme mit hochenergetischen schweren Ionen
116 Seiten
ISBN 3-932749-54-5
- Vol. 55
Andreas Janotta
Doping, light-induced modification and biocompatibility of amorphous silicon suboxides
180 Seiten
ISBN 3-932749-55-3
- Vol. 56
Sebastian Tobias Benedikt Gönnenwein
Two-dimensional electron gases and ferromagnetic semiconductors: materials for spintronics
198 Seiten
ISBN 3-932749-56-1
- Vol. 57
Evelin Beham
Photostromspektroskopie an einzelnen Quantenpunkten
186 Seiten
ISBN 3-932749-57-X
- Vol. 58
Po-Wen Chiu
Towards carbon nanotube-based molecular electronics
116 Seiten
ISBN 3-932749-58-8
- Vol. 59
Tobias Graf
Spin-spin interactions of localized electronic states in semiconductors
194 Seiten
ISBN 3-932749-59-6
- Vol. 60
Stefan Klein
Microcrystalline silicon prepared by hot wire CVD: preparation and characterization of material and solar cells
157 Seiten
ISBN 3-932749-60-X
- Vol. 61
Markus Krach
Frequenzverdreifacher mit Anti-Seriellen Schottky-Varaktor für den Terahertz-Bereich
156 Seiten
ISBN 3-932749-61-8
- Vol. 62
Ralph Thomas Neuberger
AlGaIn/GaN-Heterostrukturen als chemische Sensoren in korrosiven Medien
153 Seiten
ISBN 3-932749-62-6

Vol. 63

Sonia Perna

**Wasserstoff-Passivierung von tri-
kristallinem Silizium durch hydro-
genisiertes Siliziumnitrid**

136 Seiten

ISBN 3-932749-63-4

Vol. 64

Oliver Schumann

**Einfluss von Stickstoff auf das
Wachstum und die Eigenschaften
von InAs-Quantenpunkten**

148 Seiten

ISBN 3-932749-64-2

Vol. 65

Gerhard Rösel

**Entwicklung und Charakterisierung von
Typ-II-Heterostrukturen für die
Abstimmregion in abstimmbaren
Laserdioden**

101 Seiten

ISBN 3-932749-65-0

Vol. 66

Angela Link

**Zweidimensionale Elektronen- und
Löcher-Gase in GaN/AlGaN
Heterostrukturen**

156 Seiten

ISBN 3-932749-66-9

Vol. 67

Matthias Sabathil

**Opto-electronic and quantum transport
properties of semiconductor
nanostructures**

156 Seiten

ISBN 3-932749-67-7

Aluminum arsenide quantum wires: non-linear transport and non-Fermi liquid behavior

Joel Moser¹, Felix Erfurth, Matthew Grayson, Tobias Zibold, Max Bichler, Dieter Schuh, and Gerhard Abstreiter

Aluminum arsenide (AlAs) quantum wires are one-dimensional (1D) systems of heavy electrons where strong correlations translate into unusual transport properties. Previous work described the fabrication of those nanostructures and presented evidence for 1D conductance quantization as a function of electron density. Here we report recent studies of AlAs cleaved-edge overgrown wires and focus our research on the non-linear response of the conductance quantization, and on possible manifestations of electron-electron interactions.

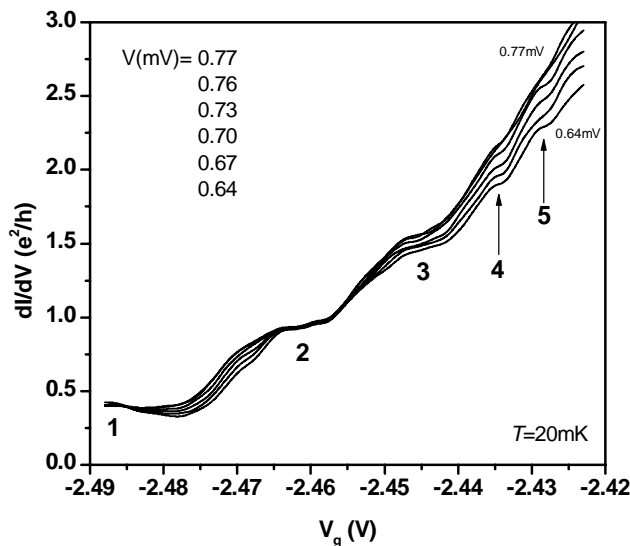


Fig. 1: Conductance vs DC bias V .

Regarding non-linear transport measurements of the conductance plateaus, along with the first and second 1D subbands steps corresponding to the population of the third, and possibly to the fourth and fifth subbands can be resolved by applying a finite dc bias V across the wire, as shown in Fig. 1. The appearance of higher 1D subbands can be interpreted as an averaging of the energy-dependent transmission coefficient over a potential window of width eV . The conductance quantum is found to be $G_0=0.44 e^2/h$, a substantially reduced value compared to the ballistic quantum $4e^2/h$ for a fourfold-degenerate spin and valley system. We have performed Hartree calculations to

investigate the influence of strain at the cleaved edge, where the wire resides, on the valley degeneracy g_v in the 1D system. We found that the band structure is locally modified compared to the band structure within the 2D electron gas (2DEG), yet in this non-interacting picture $g_v=2$ as in the 2DEG. Instead the reduction of G_0 originates from intra-wire back-scattering. In addition interaction-induced valley and/or spin degeneracy breaking is not excluded.

Turning to the role of interactions, we have observed non-Fermi liquid (non-FL) behaviors in tunneling resonances at low electron density. Such resonances occur as the chemical potential lies across disorder-induced potential barriers, thereby breaking up the wire into 0D islands of electrons. When a single 0D island, or quantum dot, is embedded within the wire, transport is mediated by resonant tunneling across the quantum dot. As temperature is varied the resonance area Γ is not conserved (see Fig. 2); instead $\Gamma(T)$ vanishes at low T as a power law, indicating a gap in the single-particle density of states at the Fermi level (see Fig. 3a.) Surprisingly two different power law exponents are measured above and below 250 mK, which signals the existence of two temperature regimes for the strength of the

¹phone: +49-89-289-12776, fax: +49-89-3206620, email: moser@wsi.tum.de

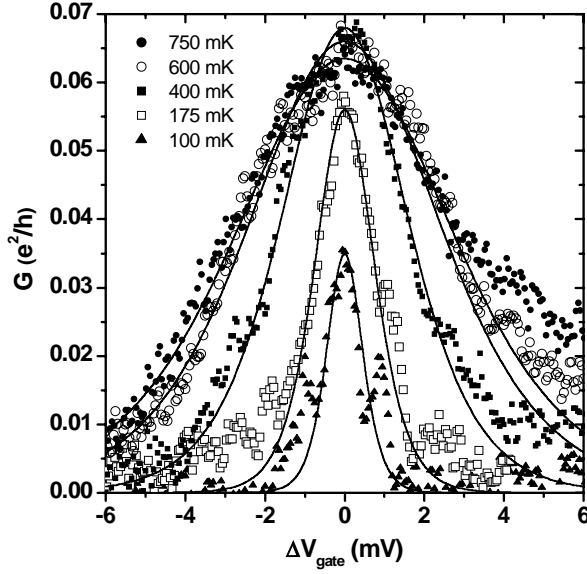


Fig. 2: Resonance A at various temperatures T .

in AlAs. We have already obtained promising results for the filtering of edge channels and are now developing new gating designs to explore possibilities in valley filtering.

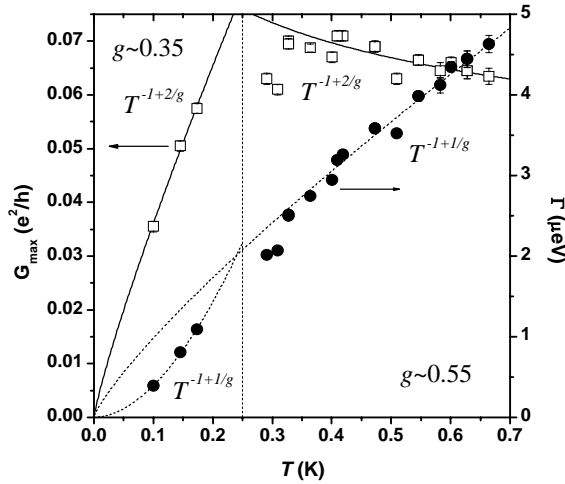


Fig. 3a: T -dependence of the area Γ and the peak G_{max} of resonance A. Different power law exponents are found below and above 250mK.

interactions. Further evidence for a non-FL is obtained by studying the dependence of G on dc bias V at base T : $\Gamma(V)$ increases with V as a power law, unlike what would be expected for Coulomb blockade resonances fed by FL leads (see Fig. 3b).

In the wake of this research, we are now exploring an alternative approach to 1D AlAs systems. We have fabricated quantum point contacts (QPC) on AlAs 2DEG and are currently looking for evidence of conductance quantization in those nanostructures. In the long run we are interested in tuning the valley degeneracy by locally depleting the 2DEG along specific crystallographic orientations to exploit the anisotropy of the electron effective mass

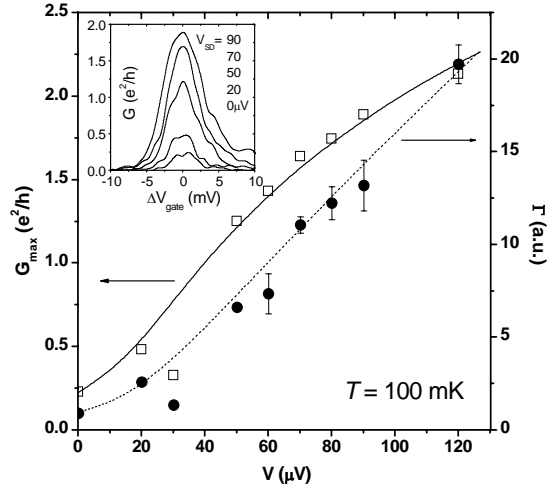


Fig. 3b: V -dependence of the area Γ and the peak G_{max} of resonance B.

Important addresses

Walter Schottky Institut
Technische Universität München
Am Coulombwall 3
85748 Garching
Germany
www-address: <http://www.wsi.tum.de>

Secretaries:

Veronika Enter
Tel.: ++49-89-28912761, Fax: ++49-89-28912737, e-mail: veronika@wsi.tum.de

Regina Huber
Tel.: ++49-89-28912781, Fax: ++49-89-3206620, e-mail: regina.huber@wsi.tum.de

Irmgard Neuner
Tel.: ++49-89-28912771, Fax: ++49-89-3206620, e-mail: irmgard@wsi.tum.de

Liane Lindner (SFB 631)
Tel.: ++49-89-28912751, Fax: ++49-89-28912737, e-mail: liane@wsi.tum.de

Faculty Members and Scientific Staff

Gerhard Abstreiter
Tel.: ++49-89-28912770, Fax: ++49-89-3206620, e-mail: abstreiter@wsi.tum.de

Markus-Christian Amann
Tel.: ++49-89-28912780, Fax: ++49-89-3206620, e-mail: mcamann@wsi.tum.de

Martin Stutzmann
Tel.: ++49-89-28912760, Fax: ++49-89-28912737, e-mail: stutz@wsi.tum.de

Peter Vogl
Tel.: ++49-89-28912750, Fax: ++49-89-28912737, e-mail: vogl@wsi.tum.de

Gerhard Böhm
Tel.: ++49-89-28912791, Fax: ++49-89-3206620, e-mail: boehm@wsi.tum.de

Martin Brandt
Tel.: ++49-89-28912758, Fax: ++49-89-28912737, e-mail: brandt@wsi.tum.de

Martin Eickhoff
Tel.: ++49-89-28912889, Fax: ++49-89-28912737, e-mail: eickhoff@wsi.tum.de

Jonathan Finley

Tel.: ++49-89-28912778, Fax: ++49-89-3206620, e-mail: finley@wsi.tum.de

Jürgen Freyer

Tel.: ++49-89-28912789, Fax: ++49-89-3206620, e-mail: freyer@wsi.tum.de

José Antonio Garrido Ariza

Tel.: ++49-89-28912766, Fax: ++49-89-28912737, e-mail: garrido@wsi.tum.de

Jacek Majewski

Tel.: ++49-89-28912741, Fax: ++49-89-28912737, e-mail: majewski@wsi.tum.de

Ralf Meyer

Tel.: ++49-89-28912790, Fax: ++49-89-3206620, e-mail: meyer@wsi.tum.de

Dieter Schuh

Tel.: ++49-89-28912779, Fax: ++49-89-3206620, e-mail: schuh@wsi.tum.de

Marc Tornow

Tel.: ++49-89-28912772, Fax: ++49-89-3206620, e-mail: tornow@wsi.tum.de

Alexandros Trellakis

Tel. : ++49-89-28912752, Fax: ++49-89-28912737, e-mail: trellakis@wsi.tum.de

Fine structure in the dI/dV characteristics of quantum Hall edge tunneling

Lucia Steinke¹, Matthew Grayson, Michael Huber, Dieter Schuh, Max Bichler, and Gerhard Abstreiter

Quantum Hall edge tunneling has been previously investigated by the authors at temperatures of 300 mK and above in perpendicular quantum wells separated by a tunnel junction. In that work it was shown that momentum conservation parallel to the barrier produced sharp features in the tunnel conductance which could be directly associated with the Landau level structure at the edge. In this work such devices were investigated for the first time at dilution-refrigerator temperatures of 30 mK, and a new fine-structure in the tunneling conductance is reported.

The device is a gated tunnel junction between a quantum Hall (QH) system and a perpendicular quantum well, such that the gate tunes the density of the QH system (inset, Fig. 1). Fig. 1 shows a plot of the differential tunnel conductance G vs. magnetic field B , where the gate bias V_g was fixed to zero. The trace was repeated for several dc bias values V_{bias} as shown. Primary peaks are indexed by the integer n and correspond to the peaks reported previously at higher temperatures, associated with the same Landau index, n . For this discussion we wish to focus on the fine structure in the peaks, observable as small wiggles surrounding each of these principle peaks only at these low temperatures (30 mK). One observes a continuous evolution of the fine structure peaks with V_{bias} , which is more clearly seen by taking the derivative dG/dB and making a color plot, shown in Fig. 2. Two prominent types of fine-structure evolution are observed: peaks which shift with positive dV/dB (Fig. 2, right) and those with negative dV/dB (Fig. 2, left).

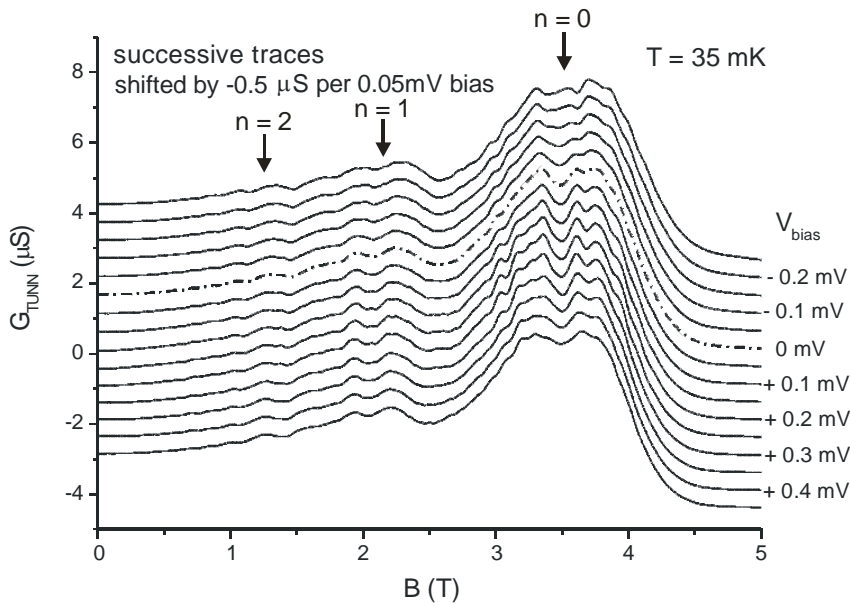
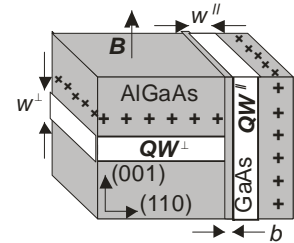


Fig. 1: Waterfall plot of a high resolution set of B -field sweeps around zero-bias, mapping the evolution of the fine structure in the tunnel conductance spectrum.



These two behaviors can be explained if one considers the resonance condition in k -space. A differential tunnel conductance resonance arises when either of the two Fermi

¹phone: +49-89-289-12756, fax: +49-89-3206620, email: steinke@wsi.tum.de

points in the sample intersect a large density of states in the other lead. In a k -space momentum-conserving picture, these intersections shift with dV/dB positive for the Fermi point of the quantum Hall system FP^\perp , and negative for the probe system FP^\parallel so we propose this as the first evidence showing both Fermi points in an edge tunneling experiment.

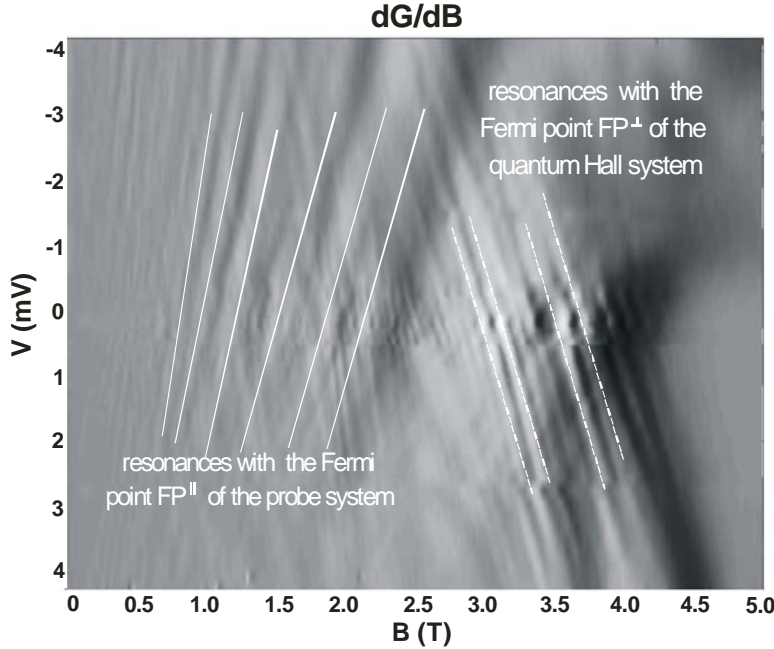


Fig. 2:

Gray scale map of the first derivative dG/dB of the tunnel conductance plotted with respect to magnetic field and bias voltage V . Bright areas correspond to peaks in dG/dB , and dark areas to valleys. Two different slopes in V vs. B in the resonance structure are observed, which could be attributed to the two possible Fermi points, at the quantum Hall edge FP^\perp and in the probe system, FP^\parallel .

The sample was also measured at zero B and the gate voltage V_g was swept. In Fig. 3 the result shows that at low temperatures (40 mK) the conductance G oscillates periodically with V_g . This periodic structure is not observable at higher temperatures due to the large thermal broadening, and is presumably due to Coulomb blockade to some local island of charge weakly coupled to the two respective leads. One candidate for this charge island is a 1D wire which may reside directly next to the barrier.

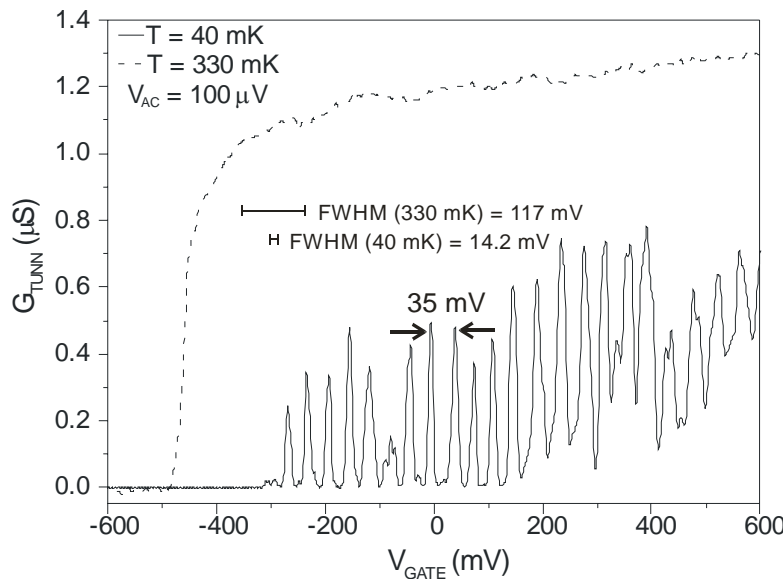


Fig. 3:

Gate voltage dependence of the tunnel conductance at 30 mK compared to a later measurement at 400 mK. At 30 mK the tunnel conductance shows oscillations as a function of gate bias with an average period of 35 mV. The periodic dependence on gate bias suggests Coulomb blockade as the likeliest explanation.

Compact expression for the angular dependence of tight-binding Hamiltonian matrix elements

Peter Vogl¹ and Aleksey V. Podolskiy

Empirical tight-binding theory gives a physically transparent, semiquantitative picture of electronic and structural properties of molecules and solids and has been applied to many systems. In the tight-binding scheme, the electronic Hamiltonian is represented in a Wannier-type or Löwdin basis set that specifies the atomic centers and the angular symmetry with respect to the given center. In the two-center approximation that is adequate for most s-p-bonded systems, the Hamiltonian matrix elements depend only on the relative position of two centers that are coupled with one another and can be written as sums of products of angular and radial integrals. The latter depend solely on the distance between the two centers but not on the orientation whereas the angular parts reflect the orientation of the orbitals localized at the two centers in space. While the radial portions of the Hamiltonian matrix are determined empirically by comparison with experiment, the angular parts can be calculated generally and depend only on the relative orientation of the 2 centers in space. These calculations were carried out by Slater and Koster a long time ago. They published extensive tables for the two-center Hamiltonian matrix elements, generally referred to as Slater-Koster energy integrals.

For s- and p-orbitals, the determination of the angular dependence of the two-center integrals can easily be calculated once for all. However, as soon as d- or higher angular momentum orbitals are included in the Hamiltonian, the expressions for the matrix elements get very cumbersome. Since the original work of Koster and Slater, a few authors have augmented the two-center matrix elements for f and g integrals and derived general expressions for any angular momentum involving lengthy 3-j and 6-j symbols. However, typing in those expressions is not only computationally inconvenient and error-prone, there is no easy way to check the validity of these expressions. In fact, errors in the original expressions of Koster and Slater have been reported repeatedly over time and there is a long list of hard-to-find errata in the literature. Not surprisingly, in the process of writing the current paper, we found some additional errors in published expressions for f and g integrals that have escaped notice so far. It is obviously desirable to have compact expressions the two-center Hamiltonian matrix elements.

In all these years, it has gone unnoticed that the two-center integrals can be written, for all angular momenta, in a fairly simple and closed analytical form that is well suited for numerical calculations and thus much less error-prone. We have derived analytical expressions for the two-center matrix elements for arbitrary angular momentum that only involve elementary functions and short summations. A code in the form of Mathematica and Maple expressions are available on the internet (www.wsi.tum.de/t33/research/codes/codes.htm).

Koster and Slater only considered nonrelativistic Hamiltonians. In semiconductors, however, the spin-orbit interaction plays an important role and is routinely included in semi-realistic tight binding calculations. Since the spin-orbit interaction is predominantly an intra-atomic effect, a localized orbital representation such as a tight binding scheme is well suited to represent the spin-orbit interaction as has been found by Chadi many years

¹phone: +49-89-289-12750, fax: +49-89-289-12737, email: vogl@wsi.tum.de

ago. Unfortunately, the angular dependence of these matrix elements is as cumbersome as in their nonrelativistic counterparts, and has only been worked out in the literature for p-orbitals. We have derived general analytic expressions for the intra-atomic spin-orbit Hamiltonian matrix elements of any orbital momentum and again provide a code that facilitates their implementation.



Controlling size and position of InAs quantum dots

Jochen Bauer¹, Robert Schulz, Emanuele Uccelli, Dieter Schuh, and Gerhard Abstreiter

The control of the spatial position of quantum dots is an important demand for the use of quantum dots in future devices and can e.g. be achieved by lithographic methods. Another approach is to self-align InAs quantum dots on well defined positions on a (1-10) GaAs surface as recently demonstrated [1]. Here the template to determine the position of the quantum dots is fabricated using the cleaved edge overgrowth technique (CEO): In a 1st growth step, a series of AlAs layers is grown with molecular beam epitaxy (MBE) on (001) GaAs. By in situ cleaving this substrate, a smooth (1-10) GaAs surface with alternating GaAs and AlAs stripes is obtained. The subsequent deposition of InAs on this surface leads to the formation of InAs quantum dots on top of the AlAs stripes. An example for such a sample is given in Fig. 1. This sample consists of 5 AlAs-/GaAs-superlattices where the AlAs width is varied from 20 nm to 40 nm and the GaAs width is kept constant at 70 nm. Structural data of the quantum dots are collected in table 1.

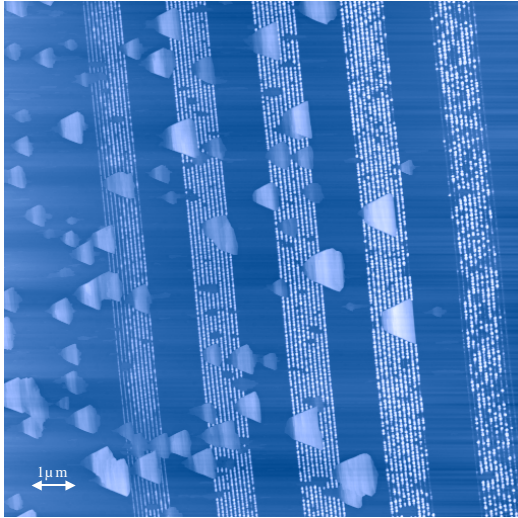


Fig. 1: AFM picture of the (1-10) cleaved edge surface overgrown with 3ML InAs on different AlAs-/GaAs-superlattices: the thickness of the AlAs layers was varied from 20 nm to 40 nm and the GaAs width is kept constant at 70 nm.

On the sample, quantum-dot like structures can clearly be identified on the AlAs stripes. Their sizes depend on the thickness of the AlAs layers as can be seen in the table below.

Table 1:

	SL1 (20nm AlAs)	SL2 (25nm AlAs)	SL3 (30nm AlAs)	SL4 (35nm AlAs)	SL5 (40nm AlAs)
Lat. size [nm]	27 - 35	30 - 40	35 - 45	35 - 45	40 - 50
Mean height [nm]	13.0 ± 1.7	15.9 ± 2.6	18.8 ± 3.3	20.9 ± 5.0	20.1 ± 3.9
Lat. size / height	2.1 - 2.7	1.9 - 2.5	1.9 - 2.4	1.7 - 2.2	2.0 - 2.5
density [$1/\mu\text{m}$]	13.6	12.6	14.1	11.8	13.2

Due to the high precision of MBE, an atomically precise positioning of these quantum dot chains is possible. Furthermore the measured size of the quantum dots is correlated with the thickness of the AlAs-strips (see table 1), and, hence, can be adjusted in the first MBE growth step. This correlation can also be seen in Fig. 2 where the quantum dot volume and the quantum dot height are plotted versus the width of the AlAs stripes. A linear correla-

¹phone: +49-89-289-12756, fax: +49-89-3206620, email: bauer@wsi.tum.de

tion of the dot height with the AlAs-width can be seen which seems to saturate for 40 nm AlAs width.

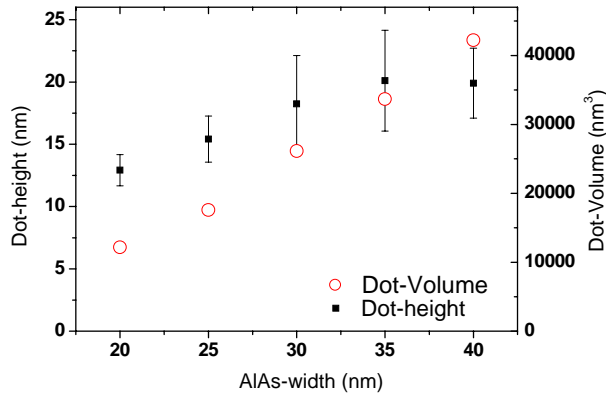


Fig. 2: Quantum dot height and quantum dot- volume are plotted versus the width of the AlAs stripes. The error bars in this figure represent the FWHM of the height distribution.

In order to investigate the optical properties of the quantum dot nanostructures we performed scanning μ -photoluminescence (μ -PL) spectroscopy on a subsequently grown sample with a GaAs capping layer. Figure 3 shows a series of μ -PL spectra which differ in the excitation power.

At low excitation power, just a single emission line at 1.308 eV is observed. The linear power dependence of this feature identifies it as arising from a single exciton (X^0). In addition, this line is an emission doublet, possibly due to elongation of the quantum dots along the AlAs layer and the resulting electron-hole exchange interaction.

Upon increasing the excitation power density, several sharp lines at lower (1.3044 eV) and higher (1.3135 eV, 1.3148 eV, 1.3166 eV and 1.3182 eV) energies emerge.

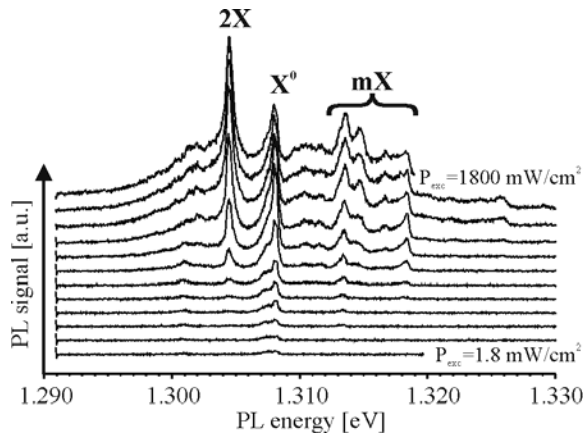


Fig. 3: μ -PL spectra of a single InAs quantum dot on the (1-10) cleaved surface as a function of excitation power. For clarity, subsequent spectra are offset vertically.

In particular, the intensity of the emission line at 1.3044 eV increases quadratically with excitation power density and dominates the spectra for the highest excitation densities investigated. This characteristic behavior identifies this peak as arising from bi-exciton (2X) recombination in the dot, an observation which is further supported by the lineshape which, in contrast with the single exciton, exhibits no exchange splitting as expected from the spin-singlet nature of the bi-exciton ground state. The other lines probably arise from multi exciton complexes (mX) and charged excitons.

In conclusion the fabricated quantum dots show excellent optical properties and have a high potential for the realisation of well defined arrays of quantum dots.

[1] J. Bauer, D. Schuh, E. Uccelli, R. Schulz, A. Kress, F. Hofbauer, J. J. Finley, and G. Abstreiter, Appl. Phys. Lett. 85, 4750(2004)

Electron paramagnetic resonance of Mn^{2+} in Mn-As-H complexes

Christoph Bihler¹, Hans Hübl, Martin S. Brandt, and Martin Stutzmann
in cooperation with Peter Klar and Wolfgang Stolz, Philipps-Universität Marburg

Ferromagnetic semiconductors such as $\text{Ga}_{1-x}\text{Mn}_x\text{As}$ are of topical interest for applications in spintronics, in particular for the realization of contacts for the injection of spin-polarized charge carriers. In GaAs, both the localized magnetic moments as well as the itinerant holes mediating the ferromagnetic coupling between them can be introduced by manganese acceptors. Thus, thin $\text{Ga}_{1-x}\text{Mn}_x\text{As}$ films with $0.01 < x < 0.06$ show metallic conductivity and ferromagnetism in their as-grown state.

Different ways of switching or influencing the magnetism in this material are currently being investigated. One possibility is post-growth hydrogenation. The incorporated hydrogen forms Mn-As-H complexes and thus passivates the Mn acceptors. If the H concentration reaches the Mn concentration, the samples become semiconducting and paramagnetic.

According to this model, the Mn atoms in the Mn-As-H complexes should be in the $\text{Mn}^{2+}(3d^5)$ oxidation state with g-factor $g=2$ and spin $S=5/2$. In order to investigate the influence of the crystal field on the symmetry of the 3d-electron wave function, angle-dependent electron paramagnetic resonance (EPR) spectra of hydrogenated metal-organic vapour-phase epitaxy (MOVPE) grown samples with $x \leq 0.005$ have been measured (Fig.1). A resolved hyperfine structure consisting of six resonances can only be observed under certain orientations of the sample with respect to the magnetic field (30° and 90°). This behavior can be understood by means of the Breit-Rabi diagram in Fig.2. The Zeeman interaction described by g causes a splitting into six equally spaced energy levels. These levels are shifted in their energies by the influence of the crystal field, resulting in a fine structure splitting. Furthermore, each Zeeman level is split sixfold by hyperfine interaction with the nuclear spin $I=5/2$ of the ^{55}Mn nuclei. Consequently, between neighboring Zeeman levels ($\Delta m_s = \pm 1$) there are six allowed magnetic dipole transitions with $\Delta m_l = 0$, giving rise to a total of 30 transitions. If - as in the sample investigated - the fine structure splitting is smaller than the hyperfine splitting, the five fine-structure line groups will overlap and thus diminish the resolution of the hyperfine resonances. Only for vanishing fine structure

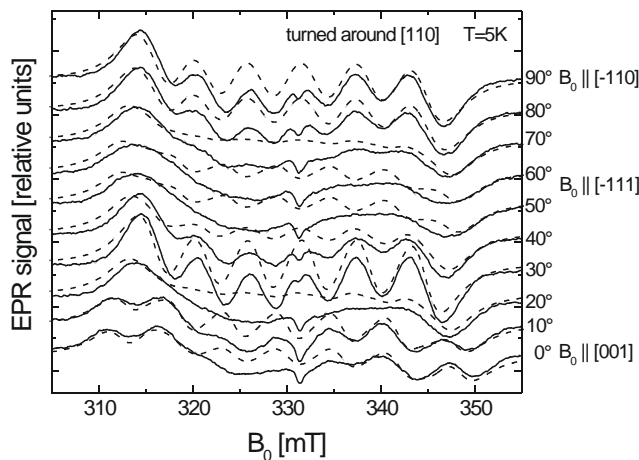


Fig. 1:

Angle-dependent EPR spectra of a hydrogenated MOVPE-grown sample with $x \approx 0.005$ (full lines). The spectrum has been simulated (dashed line) using $g = 2$, $A = -0.67 \mu\text{eV}$, $D_{[001]} = -0.012 \mu\text{eV}$, $D_{\langle 111 \rangle} = 0.012 \mu\text{eV}$ and $a = -0.18 \mu\text{eV}$.

¹phone: +49-89-289-12755, fax: +49-89-289-12737, email: bihler@wsi.tum.de

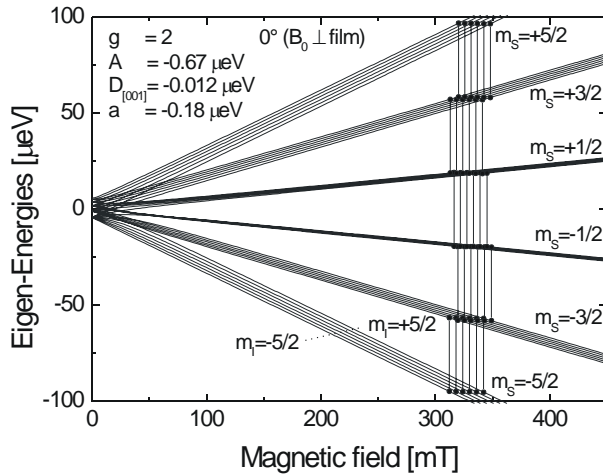


Fig. 2: Breit-Rabi diagram for GaAs:Mn²⁺ with the magnetic field oriented perpendicular with respect to the GaMnAs layer. The vertical lines indicate the allowed magnetic dipole transitions with $\Delta m_s = \pm 1$ and $\Delta m_l = 0$.

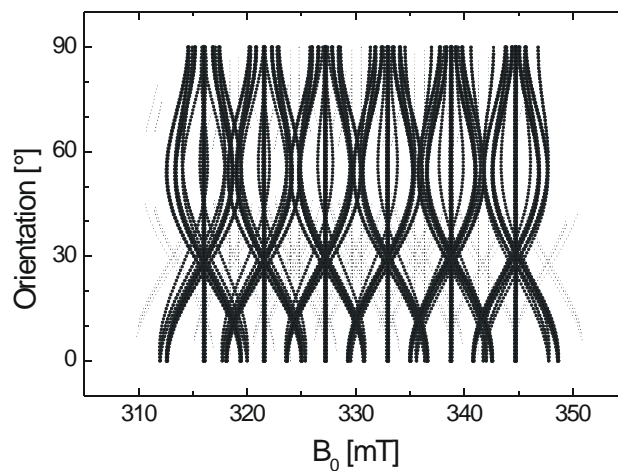
splitting, the six hyperfine resonances will be resolved – which in our sample is the case at 30° and 90° orientation between external magnetic field and [001] direction.

For the simulation of the measured EPR spectra in Fig.1, in addition to the cubic anisotropy of the GaAs host lattice, an uniaxial anisotropy in the [001] growth direction and an uniaxial anisotropy in the $\langle 111 \rangle$ directions, where H is expected to be incorporated, have to be considered. As the simulation shows (Fig.1 and 3), the observed anisotropy can be well described by the hyperfine splitting A and the cubic anisotropy a . The uniaxial anisotropy contributions $D_{[001]}$ and $D_{\langle 111 \rangle}$ mainly decrease the resolution of the fine structure and thus the given values must be considered as upper limits.

From the small value of $D_{\langle 111 \rangle}$, one can deduce that the influence of the incorporated H on the Mn 3d-electron wave function is rather small. This might be explained by H occupying a back-bonded position in the Mn-As-H complex. Furthermore, the small value of $D_{[001]}$ indicates that the Ga_{1-x}Mn_xAs layer is only weakly strained in growth direction, corresponding to a high crystalline quality of the MOVPE sample investigated. A second sample with a higher Mn concentration showed less resolved EPR spectra. This strain induced broadening is an indication why the Mn²⁺(3d⁵) state so far could not be observed in EPR for hydrogenated low-temperature molecular beam epitaxy (LT-MBE) grown samples in the concentration range of $0.01 < x < 0.06$.

Fig. 3:

Anisotropy of the EPR resonance fields B_0 simulated with the same parameters as in Fig.1. The size of the dots corresponds to the expected intensity of the resonance line.



Carrier localization in diamond surface conductive channels

Jose Antonio Garrido¹, Tobias Heimbeck, and Martin Stutzmann

The p-type surface conductive channel induced in hydrogen terminated diamond surfaces is a very interesting system to study the effect of disorder-induced localization. The combination of surface hydrogen termination and the presence of surface adsorbates produces an accumulation of holes in a surface channel, where carrier concentrations up to $5 \times 10^{13} \text{ cm}^{-2}$ have been reported. The holes are expected to form a two dimensional channel directly at the diamond surface. Thus, the presence of charged surface adsorbates and

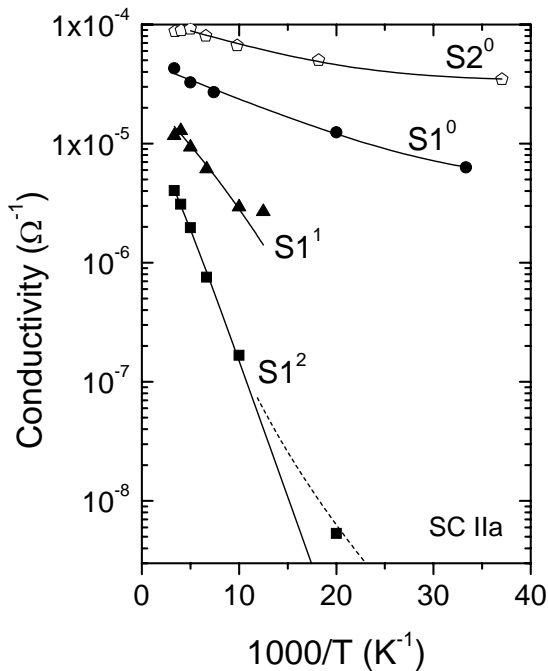


Fig. 1: Surface conductivity versus $1/T$ for samples with different conductivities.

structural defects is expected to play an important role for the transport and the scattering of holes in this surface channel. In addition, an inhomogeneous hydrogen termination of the diamond surface should have a similar effect. Therefore, noticeable surface potential fluctuations are expected, analogous to silicon inversion layers with interface oxide charges. We have studied the transport properties of holes in 2D conductive channels at the surface of hydrogen-terminated diamond samples. A specific annealing step was used to vary the concentration of carriers in the conductive channel of the same sample, and to investigate its influence on the conductivity. Hall experiments have been performed to evaluate the impact of the expected surface disorder on the transport properties. In the studied temperature range (30K-300K), we did not observe freeze out of carriers, as expected for the Anderson mobility edge model. Fig. 1 shows the typical temperature dependent conductivity for single crystalline surface conductive diamond samples. The symbols represent the experimental results, whereas the solid lines represent the conductivity calculated using a model described below. In vacuum, and without any annealing process (corresponding to symbols in curves S1⁰ and S2⁰), the measured 2-D conductivities at room temperature are in the range $5 \times 10^{-5} - 10^{-4} \text{ } \Omega^{-1}$, and decrease with decreasing temperature. However, the dependence of the conductivity on temperature is very weak for samples S1⁰, and S2⁰. According to Fig. 2, the carrier concentration (extracted from Hall effect experiments) is almost independent of temperature. Annealing the samples in vacuum reduces the number of holes accumulated in the inversion layer, as shown in Fig. 2 for samples S1 and S3. For instance, in the case of sample S1 the carrier concentration (measured at room temperature) can be varied between $9 \times 10^{12} \text{ cm}^{-2}$ for the non-annealed state (S1⁰), $2.4 \times 10^{12} \text{ cm}^{-2}$ after one annealing step (S1¹), and $9 \times 10^{11} \text{ cm}^{-2}$ after two annealing steps (S1²). In contrast, a strong influence of this annealing process on the

¹phone: +49-89-289-12766, fax: +49-89-289-12737, email: garrido@wsi.tum.de

temperature dependence of the conductivity can be observed in Fig. 1. In the high temperature regime, the temperature dependence of the conductivity resembles an exponentially activated behaviour, with the activation energy increasing as the carrier concentration decreases.

At lower temperatures the conductivity does not follow the pure exponential dependence on temperature anymore. Interestingly, the activated behaviour of the conductivity is not the result of an activated carrier concentration, as clearly seen in Fig. 2. Instead, the Hall mobility is temperature activated in a very similar way as the conductivity (Fig. 3). At room temperature and without any annealing, the Hall mobility is in the range 30-100 cm^2/Vs . Mirroring the behaviour of the conductivity, at high temperature the mobility shows an exponentially activated behaviour, while at lower temperatures saturation is observed. Our experiments show a complex behaviour of the mobility which cannot only be explained by the reduction of the mobility at lower temperatures as a result of the impurity scattering mechanism.

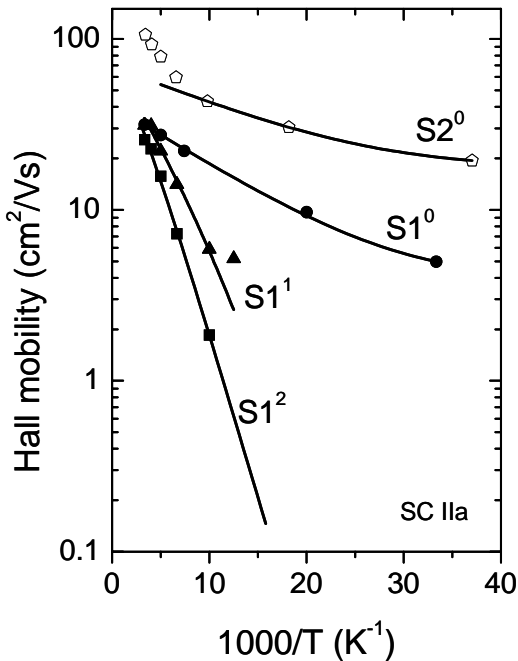


Fig. 3: Temperature dependence of the Hall mobility.

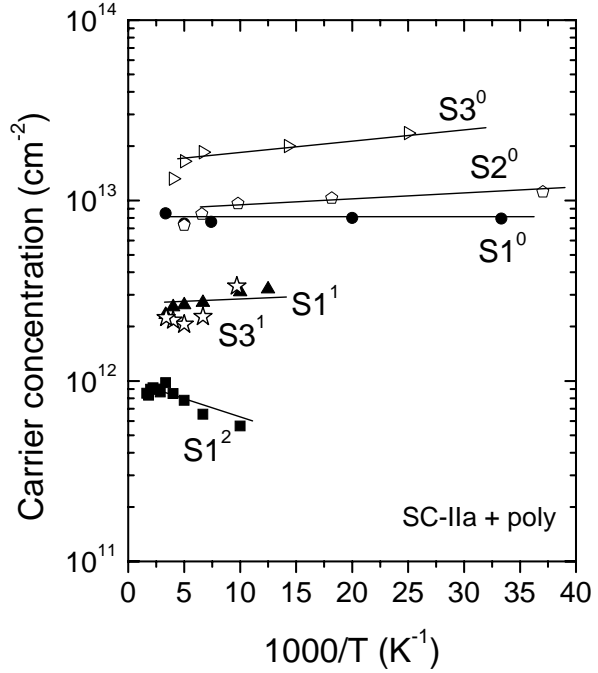


Fig. 2: Temperature dependence of the carrier concentration of different samples.

Mirroring the behaviour of the conductivity, at high temperature the mobility shows an exponentially activated behaviour, while at lower temperatures saturation is observed. Our experiments show a complex behaviour of the mobility which cannot only be explained by the reduction of the mobility at lower temperatures as a result of the impurity scattering mechanism.

We have adopted an early model by Arnold who, using percolation theory, attributed the activation of the conductivity and the Hall mobility to the presence of long-range inhomogeneities in the samples, suggesting that metallic and thermally activated conductivity coexist over an appreciable range of carrier concentration.^[1] Our results have been fitted using the model proposed by Arnold (solid lines in Figures 1 and 3) with a very good agreement.

[1] E. Arnold, Surf. Sci. **58**, 60 (1976)

Effects of strain and confinement on the emission wavelength of InGaAs quantum dots due to a GaAsN capping layer

Stefan Birner¹, Oliver Schumann², Lutz Geelhaar², and Henning Riechert²

For optical fiber applications quantum dot (QD) lasers emitting at 1.3 and 1.55 μm are of great interest because of predictions for improved laser properties like lower threshold current density and reduced temperature sensitivity compared to quantum wells. A lot of investigations have been made to expand the emission wavelength of QDs towards 1.3 μm . This is done mainly by lowering the growth rate, embedding the QDs into an InGaAs quantum well or stacking of QDs. Another successful approach to reach 1.3 μm on GaAs substrates is the incorporation of nitrogen into the material surrounding the QDs where nitrogen reduces the lattice constant and, thus, also reduces the overall compressive strain in the sample formed due to the larger lattice constant of the QD material. These prospects have recently encouraged some investigations to examine the influence of nitrogen incorporation into the surrounding matrix material. The use of GaAsN as a capping layer for the QDs allows a wavelength extension of more than 100 nm. This wavelength extension is often attributed to the relief of the strain inside the QDs which is ascribed to strain compensation. However, we showed through our simulations that the opposite is the case. Although the GaAsN matrix leads to a reduction in the hydrostatic strain in the material surrounding the QDs, the hydrostatic strain inside the QDs increases. This strain inside the QDs can strongly change their emission wavelength. Therefore, exchanging the GaAs capping layer with a material of different lattice constant is expected to allow a tailoring of the emission wavelength of the QDs.

In addition, the electronic confinement of the QD, *i.e.* the height of the potential barrier formed by the conduction and valence band offsets of the QD and of the matrix material due to the different band gaps has an important influence on the emission wavelength as well. Increasing or decreasing the confinement results in a blueshift or redshift of the emission wavelength, respectively. Fig. 1 shows the conduction and valence band profile for two different matrix materials together with a sketch of the QD structure.

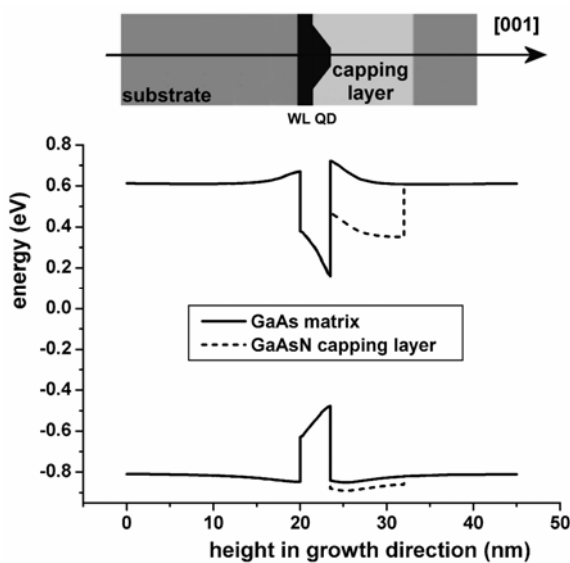


Fig. 1:

Conduction and valence bands as obtained from the simulations with a nitrogen content of 1.2% in the 10 nm thick GaAsN layer above the InGaAs quantum dot (QD) and the reference structure without nitrogen. The band structure is taken along a line in growth direction through the center of the QD. One can clearly see that the confinement of the electrons is reduced significantly due to the incorporation of nitrogen around the QD. The wetting layer (WL) consists of $\text{In}_{0.25}\text{Ga}_{0.75}\text{As}$ whereas the In content in the QD varies linearly from 25% to 100% at the top.

¹phone: +49-89-289-12752, fax: +49-89-289-12737, email: stefan.birner@nextnano.de

²Infineon Technologies AG

Our experiments and simulations showed that a GaAsN capping layer grown on InGaAs QDs induces a strong redshift of the emission wavelength and extends it beyond 1.3 μm (Fig. 2). In order to understand this behavior, we investigated this effect systematically by changing the nitrogen content in the GaAsN layer, varying the thickness of this layer and by embedding a GaAs spacer layer between the GaAsN layer and the QDs. We simulated the band structure and the electron and hole energy levels based on 6×6 $\mathbf{k}\cdot\mathbf{p}$ calculations including strain, deformation potentials and piezoelectric effects using the 3D device simulator *nextnano*³ [1]. The QDs in our simulations have the shape of a symmetric truncated pyramid and the geometrical and alloy profile parameters for modeling the QDs were taken from XSTM measurements of our grown samples. The wetting layer underneath the QD is 2 nm thick and has an In content of 25% whereas the In content inside the QD varies linearly from 25% at the bottom to 100% at the top of the QD.

By means of our simulations we have shown that the strain inside the QDs is almost unaffected by the incorporation of moderate amounts of nitrogen (~ 1 –2%) into the GaAs capping layer and cannot explain the observed increase of the emission wavelength. Instead, we conclude from comparisons between experimental data and simulations that the extension of the wavelength is caused by the strong reduction of the conduction band energy in the GaAsN layer (with respect to GaAs) and the hence resulting reduction of the confinement of the electron wavefunction in the QDs. The origin of the reduction of the conduction band energy is a special feature of the so-called *diluted nitride* semiconductor material GaAsN where the incorporation of small amounts of nitrogen leads to the formation of a narrow impurity band that lies energetically above the conduction band. The coupling of this impurity band to the conduction band leads to a reduction of the conduction band energy and thus to a decrease in the band gap energy. We modeled this band gap reduction by appropriate bowing parameters that were extracted from the widely accepted band-anticrossing model for diluted nitrides.

Furthermore, we showed both experimentally and by means of simulations that the insertion of a GaAsN layer below the QDs yields only a very small change in wavelength in contrast to the GaAsN capping layer.

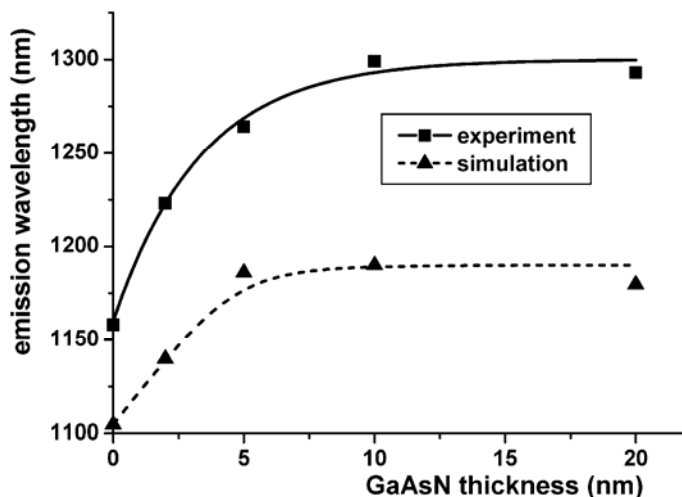


Fig. 2: Emission wavelength of the QDs at 300 K as a function of the thickness of the GaAsN_{1.2%} capping layer. The squares correspond to the experimental and the triangles to the simulated data. We varied the thickness of the GaAsN layer from 0 to 20 nm. A strong redshift of the emission wavelength is observed for increasing thickness of the GaAsN capping layer. At a thickness of about 10 nm, this redshift

[1] The *nextnano*³ software package can be downloaded from www.wsi.tum.de/nextnano3. Support is available through www.nextnano.de.

Modeling of purely strain-induced GaAs/InAlAs quantum wires

Stefan Birner¹, Robert Schuster², and Werner Wegscheider²

Cleaved edge overgrowth (CEO) quantum wires (QWRs) at the intersection of two perpendicular quantum wells (QWs) where the (100) QW and the (011) QW are of type I, thus allowing for electron and hole confinement, have shown to provide enhanced exciton binding energies and a concentration of the oscillator strength. At the T-shaped intersection a one-dimensional QWR running along the direction perpendicular to the (0-11) plane is formed because electron and hole wave functions can expand into a larger volume. For clear one-dimensional characteristics at room temperature, a large energy separation between the constituting two-dimensional QWs and the QWR is needed. The optimization of this confinement energy was sought by a variety of groups using unstrained and strained structures. Here, we theoretically studied strained QWR structures that were grown using the CEO technique and consist of a single QW only. Strong carrier confinement is achieved purely by lateral strain variation within the QW which is promising for the development of room temperature devices. In the first growth direction an InAlAs layer serves as the stressor material. Growing a GaAs QW directly on the cleaved (011) plane in a second growth step results in a strongly strain modulated T-shaped structure.

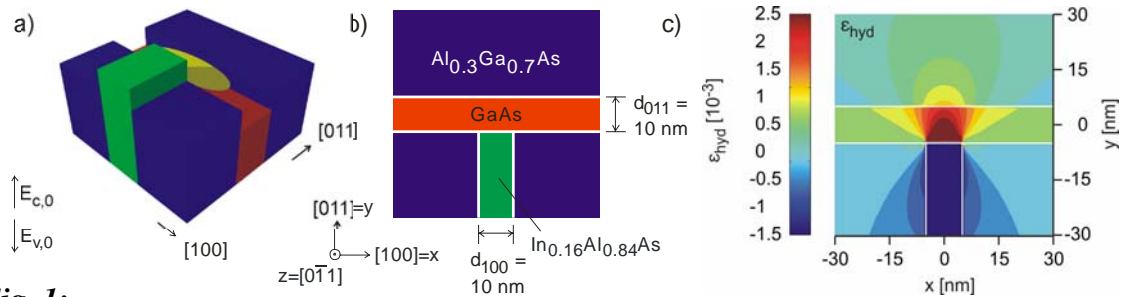


Fig. 1:

a) Conduction $E_{c,0}$ (or valence $E_{v,0}$) band edge without considering strain effects. The position of the wave function is indicated. b) Schematic of the strained T-shaped QWR structure. The 10 nm GaAs QW is grown on the cleaved edge of a strained $\text{In}_{0.16}\text{Al}_{0.84}\text{As}$ barrier. c) The hydrostatic strain (trace of the strain tensor, i.e. relative change in volume) has its maximum at the intersection, where it leads to a reduced band gap which is the requirement for confining the charge carriers. Thus, the QWR is formed in the GaAs QW due to the tensile strain field induced by the $\text{In}_{0.16}\text{Al}_{0.84}\text{As}$ layer.

In the sample sketched in Fig. 1b), the $\text{In}_{0.16}\text{Al}_{0.84}\text{As}$ barrier layer (width 10 nm) has a larger lattice constant than $\text{Al}_{0.3}\text{Ga}_{0.7}\text{As}$ and thus is subject to tensile strain in the [100] direction, which is transmitted to the overgrown GaAs QW (width 10 nm) where a QWR is formed at the lateral positions of the stressor layers. Since this direct growth on the cleaved edge leads to strong strain modulations, large confinement energies were predicted for such structures. Here, we present results of computations with the nano device simulator **nextnano³**, which was used for the optimization of the sample layout. The strain tensor was calculated by minimizing the elastic energy within continuum elasticity theory, where the units cells were allowed to deform in the (x,y) plane only. Along the translationally invariant z direction the lattice commensurability constraint forced the InAlAs layer to

¹phone: +49-89-289-12752, fax: +49-89-289-12737, email: stefan.birner@nextnano.de

²University of Regensburg

adopt the lattice constant of $\text{Al}_{0.3}\text{Ga}_{0.7}\text{As}$. The new conduction and valence band edges were determined by taking into account the shifts and splittings due to the relevant deformation potentials. The strain-induced piezoelectric fields were obtained by solving Poisson's equation. Finally, the 2D single-band Schrödinger equation had to be solved for the electron and heavy hole eigenenergies and wave functions within effective-mass theory using the envelope function approximation in a self-consistent Schrödinger-Poisson cycle. For the electrons we assumed an isotropic effective mass tensor, whereas for the heavy holes an anisotropic effective mass tensor (GaAs: $m_{100} = 0.350 m_0$, $m_{011} = 0.643 m_0$) was derived from the Luttinger parameters. At the interfaces all material parameters varied step-like. Fig. 2 depicts the electron and hole probability densities in a strained GaAs/ $\text{In}_{0.16}\text{Al}_{0.84}\text{As}$ QWR. The separation of the electron and hole wave functions, which unfortunately reduces the overlap integral that is important for optical transitions, is an effect of piezoelectricity. Neglecting the piezo effect results in symmetric probability densities as shown in Fig. 2a). It is important to realize that the confinement is purely due to strain. If the strain is neglected it is not possible to confine charge carriers at the T-shaped intersection. In Fig. 3 the calculated confinement energy, which is the difference between the electron-hole ground state transition energies of the QW and the QWR, is plotted and compared to experimental results of spatially resolved micro-photoluminescence measurements. While the rising of the confinement energy with increasing stressor layer thickness and increasing width of the overgrown QW is very well reproduced with our single-band approach, the calculated absolute values do not match the experimental data perfectly well. Confinement energies in the range of 50 meV with respect to the corresponding energy for the QW are obtained, which is approximately twice the value of $k_B T$ at room temperature. To enhance the overlap of the electron and hole wave functions the $\text{In}_{0.16}\text{Al}_{0.84}\text{As}$ layer can be replaced by quaternary $\text{In}_{0.16}\text{Al}_{0.84-x}\text{Ga}_x\text{As}$. With increasing x the band gap of the stressor layer gets smaller without relevantly changing the strain configuration. The simulations show that for $x=0.7$ the electron wave function is located closer to the center of the hole wave function than shown in Fig. 2.

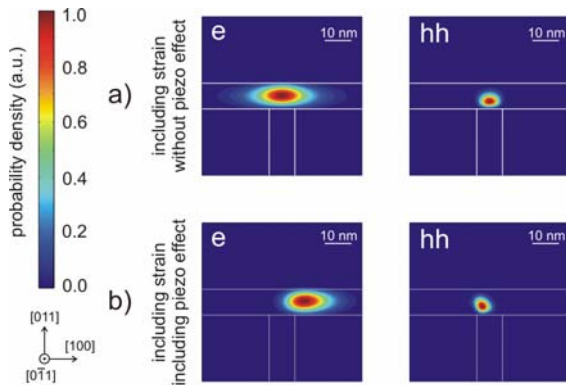


Fig. 2:

Contour plots of the calculated probability densities of the electron (e) and heavy hole (hh) wave functions. The units are scaled so that the maximum value equals 1.

a) without piezoelectric fields

b) including piezoelectric fields

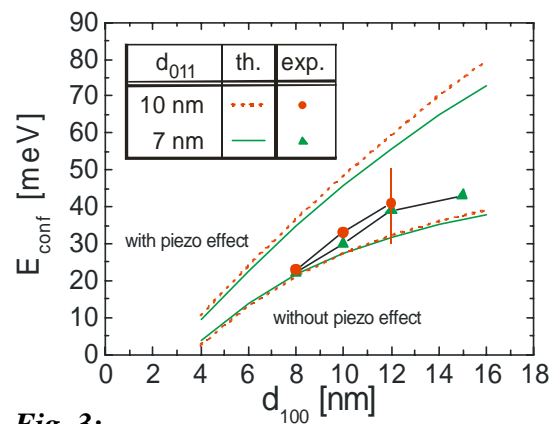


Fig. 3:

Theoretical (*th.*) and experimental (*exp.*) values of the confinement energies E_{conf} of strained GaAs/ $\text{In}_{0.16}\text{Al}_{0.84}\text{As}$ QWRs where the thickness of the stressor layer and the QW were varied. The piezo effect clearly enhances the confinement energy.

[1] The nextnano³ software package can be downloaded from www.wsi.tum.de/nextnano3. Support is available through www.nextnano.de.

Ferromagnetic properties of manganese doped germanium

Dominique Bougeard¹, Stefan Ahlers², Hubert Riedl, and Gerhard Abstreiter

Magnetic semiconductors represent a promising candidate for the implementation of spintronics devices. An additional degree of freedom is introduced in such devices by making use of both carrier charge and spin. While considerable progress concerning the elaboration and possible technological applications of magnetic semiconductors has been made on III-V-based systems like (Ga,Mn)As, research on group IV-based DMS still resides in the beginnings. However, theoretically predicted high magnetic transition temperatures and the possibility of an integration into the mature Si/Ge-semiconductor technology suggest a high potential of IV-based magnetic semiconductors. In this work we present first investigations of the structural and ferromagnetic properties of epitaxially grown, manganese doped germanium.

In thermodynamic equilibrium the solubility limit of Mn in Ge is $4.4 \cdot 10^{15} \text{ cm}^{-3}$, resulting in a maximum equilibrium Mn concentration of $10^{-5} \%$. However, much higher dopant concentrations (usually in the order of several percent) are believed to be required to provide both good electrical conductivity and observable ferromagnetic effects. Low substrate temperature molecular beam epitaxy (MBE) enables crystallographic growth far from thermodynamic equilibrium. We choose low substrate temperatures (LT-MBE) to further reduce the solubility limit and prevent the formation of large, incoherent intermetallic clusters. Figure 1 shows the TEM image of a typical 200 nm thick Ge:Mn layer grown by LT-MBE at a substrate temperature of $70 \text{ }^\circ\text{C}$, a Ge flux rate of 0.08 \AA/s , introducing a mean Mn concentration of 3.4 %. The crystal quality of the deposited material is good and matches the matrix of the substrate up to Mn contents of 3.4%. No dislocations can be observed. The layer shows the formation of Mn rich clusters under these growth conditions. The clusters are homogeneously distributed in the layer. They are slightly elongated along the growth direction, have a typical width of several nm and a typical length of several ten nm for mean Mn contents up to 3.4%. Clusters are coherently incorporated into the host matrix (see inset in figure 1). The cluster size and density increase with the Mn concentration. For Mn contents around 40% the LT-MBE layer is polycrystalline.

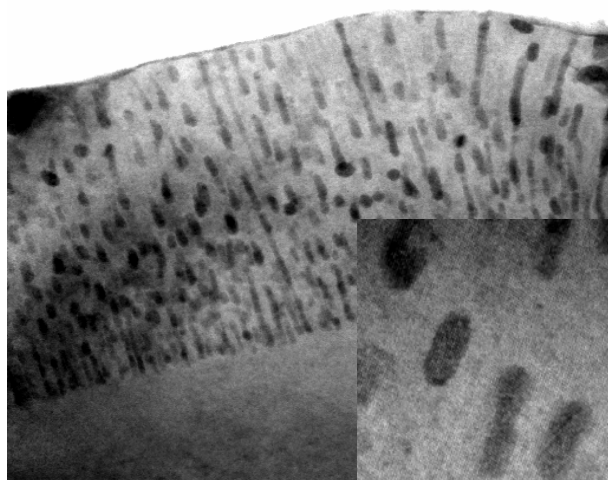


Fig. 1:

TEM image of a 200 nm Ge:Mn layer with Mn concentration of 3.4 % and substrate temperature of $70 \text{ }^\circ\text{C}$ showing the existence of elongated Mn clusters. The inset (high res TEM) shows the coherence of Mn clusters. TEM in cooperation with Dr. Achim Trampert, Paul-Drude-Institut, Berlin

¹ phone: +49-89-289-12777, fax:+49-89-3206620, email: bougeard@wsi.tum.de

² phone: +49-89-289-12777, fax:+49-89-3206620, email: ahlers@wsi.tum.de

While further TEM analysis to obtain structural and chemical information about the clusters currently is in progress, SQUID magnetisation measurements show clear ferromagnetism for samples doped with Mn concentrations of 2.5, 3.4 and 40.3%. The curves indicate the presence of intermetallic Mn_5Ge_3 precipitates. Figure 2 shows the dependence of magnetisation on temperature, which is both in shape and in Curie temperature (approximately 300 K) similar to results known for pure Mn_5Ge_3 . Hysteretic behaviour can be observed in hysteresis measurements done at variable temperatures between 4.2 K and room temperature. Yet the absence of a square hysteresis (known e. g. from (Ga,Mn)As) is a sign of weak ferromagnetic ordering. This is confirmed by the calculation of magnetic moments from the nominal Mn concentration and the measured magnetisation. Values range from 0.4 to 1.1 μ_B , significantly below the expected value of Mn_5Ge_3 (2.5 μ_B).

Hall voltage measurements show a clear p-type behavior of LT-MBE Ge:Mn structures grown on intrinsic substrates. No distinct feature of an anomalous Hall effect induced by the presence of magnetic moments in the layer can be observed. Furthermore no significant dependence of the Hall voltage on Mn content can be observed. The carrier concentrations in the order of 10^{17} cm^{-3} deduced from these measurements tend to show that only a small fraction of the introduced Mn is electrically active. The influence of ferromagnetic Mn rich clusters on the transport properties of the Ge:Mn layers has to be further investigated.

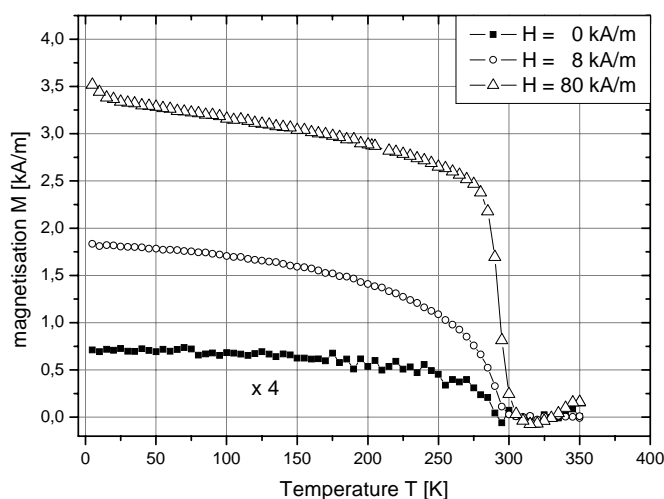


Fig. 2:
SQUID: magnetization vs. temperature. The shape of the graphs and a Curie-temperature of ~ 300 K indicate the presence of the intermetallic phase Mn_5Ge_3 . SQUID in cooperation with Wolfgang Kipferl, University of Regensburg

Effects of thermal annealing on the bandgap of GaInAsSb

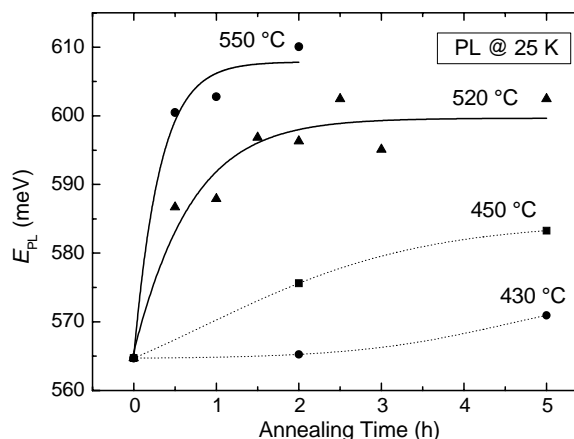
Oliver Dier¹, Susanne Dachs, Christian Lauer, Markus Grau, Chu Lin, and Markus-Christian Amann

GaInAsSb alloys have received growing interest as active materials in optoelectronic devices in recent years. These materials are widely used in lasers, light emitting diodes, and photodiodes, operating in the 1.8 μm to 3 μm wavelength range. The main application for uncooled, cheap light sources and detectors in this wavelength range is gas sensing, using the tunable laser diode absorption spectroscopy (TDLAS) principle. Single mode light sources like DFB-lasers or VCSELs as used for TDLAS require the exact knowledge of the gain spectrum and therefore of the bandgap of the active material. We have investigated the blue shift of GaInAsSb lattice-matched to GaSb to provide the tuning wavelength data needed for a VCSEL or DFB device process. Quantum-Well samples as well as bulk material were annealed at typical growth and processing temperatures between 430°C and 600°C. The samples were characterized using photoluminescence (PL) at 25 K and high resolution X-ray diffraction (HRXRD). The QW samples contained five 10 nm thick GaInAsSb quantum wells with 15 nm AlGaAsSb barriers. Bulk samples consisted of 500 nm GaInAsSb. To investigate the origin of the blue shift, the indium concentration was varied between 20% and 40% for different samples, and the growth temperature ranged from 430°C to 520°C. Also different compressive strain of 0.5%, 1.0% and 1.5% was applied. To quantify the blue shift, a sample with 30% indium and 0.75% compressive strain was grown on a full wafer at 490°C. After growth, pieces of the samples were annealed in the MBE system under Sb stabilization. The annealing time varied from 0.5 to 5 hours, while the annealing temperature was diversified from 430°C to 600°C. To measure the photoluminescence an FTIR setup (using CaF₂ optics and beam-splitter) was used. The samples were mounted on a cryostat and pumped with a 488 nm argon laser. For bulk samples with less light emission a diode laser at 805 nm with 1 W maximum optical power was used for pumping. For GaInAsSb bulk-material a maximum blue shift of 83 meV was found after annealing for 2 hours at 520°C. Also an increase of the PL-intensity for the annealed sample was observed at the same pumping power, but no measurable changes in the full width at half maximum (FWHM) occurred. Using HRXRD, a small increase of compressive strain was observable, indicating a change in the material composition. Due to more degrees of freedom in material composition and strain, MQW samples were fabricated to investigate the influence of compositional (strain, indium content) and growth (growth temperature, V/III-ratio) parameters on the energy shift. Neither a growth regime nor composition of the quaternary alloy was found, in which the alloy was thermally stable. To quantify the blue shift, an MQW-structure with Ga_{0.7}In_{0.3}As_{0.07}Sb_{0.93} as active material was deposited on a full wafer and afterwards pieces of the sample were annealed at different times and temperatures, as shown in Fig. 1. Here, although the sample was grown at 490°C, a blue shift of around 20 meV occurred, for annealing at 40°C below growth temperature. For higher temperatures, a saturation of the blue shift is observed. Fig. 2 shows the photoluminescence energy plotted versus the annealing temperature of an MQW-structure. It shows a linear behavior in the investigated range, no saturation like in Fig. 1 occurred.

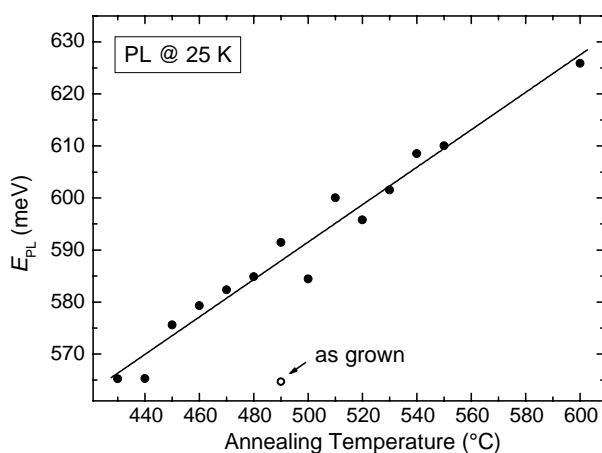
¹phone: +49-89-289-12788, fax: +49-89-3206620, email: dier@wsi.tum.de

Fig. 1:

Blue shift of annealed GaInAsSb as measured by photoluminescence at 25 K. The samples were annealed for up to 5 hours with different temperatures. For higher temperatures a saturation is observable.



The energy for the unannealed sample is shown as an open circle. Samples annealed at temperatures above 430°C showed a blue shift, although annealing temperature was below the growth temperature of 490°C. Similar to Fig. 1, the blue shift was already visible below growth temperature. The maximum blue shift was found to be 61.2 meV, if annealed at 600°C for two hours. The reasons for the blue shift are not yet clear. GaInAsSb is known to have a large miscibility gap, so some kind of decomposition is a possible explanation.

**Fig. 2:**

Photoluminescence energy at 25 K vs. annealing temperature for a GaInAsSb quantum-well sample. The sample showed a strong blue shift if annealed below growth temperature.

Antisites and reordering processes in GaInAsSb could be another possible reason, since for GaSb an intrinsic p -type doping is related to Ga_{Sb} antisites, and we found an intrinsic p -type doping of 10^{17} cm^{-3} in GaInAsSb (as measured by van der Pauw experiments). Furthermore, scanning transmission electron microscopy (STEM) images of MOVPE-grown GaInAsSb showed a variety of dislocations, which can affect the bandgap and could also be changed by annealing. For further investigations a high resolution investigation method is required. For low annealing temperatures, as used in this work, quantum-well intermixing is the only mechanism which can be excluded, because the same blue shift was also found in bulk material.

Modulating the growth conditions: Si as an acceptor in (110) GaAs for high mobility p-type heterostructures*

Frank Fischer, Matthew Grayson¹, Dieter Schuh, Max Bichler, Karl Neumaier², and Gerhard Abstreiter

High mobility two-dimensional holes in GaAs are of research interest both for their strong spin-orbit coupling and for their heavy mass. Studies of spin effects may have implications for the field of spintronics, since a large Rashba term splits the spin subbands even at zero external magnetic field, B . The large mass has led to studies of a new kind of metal insulator transition and evidence of a Wigner crystal.

We begin with studies of the metal insulator transition (MIT) in *bulk p-type* doped samples. We investigated a high density sample p^+ exhibiting metallic behavior for $T \rightarrow 0$ and a low density sample p^- which is insulating for $T \rightarrow 0$ and not measurable below $T < 10$ K. Both samples are heavily auto-compensated. The Hall coefficient R_H in the p^- sample has a non-monotonic temperature dependence (Fig. 1). In addition, the longitudinal resistance can be divided into two regimes with different activation energies. This type of transport is well-described by hopping conduction in a parallel impurity band.

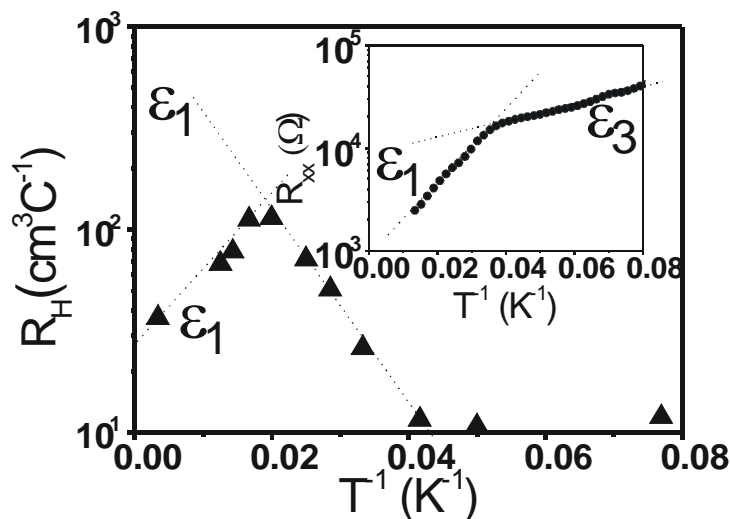


Fig. 1: Arrhenius plot of the Hall coefficient showing a non-monotonic temperature dependence. The dotted lines indicate the associated activation energies. Inset: longitudinal resistance exhibits activated behavior.

It is typical for lightly bulk-doped semiconductors with conduction in the valence band and in an impurity band. The activated behavior $\epsilon_3 = 2.1$ meV characterizes the nearest neighbor hopping gap. The deduced acceptor activation energy $\epsilon_1 = 7.8$ meV is about a factor of x5 smaller than the activation energy $\Delta E = 35$ meV of isolated Si-acceptors in GaAs obtained by Hall-effect measurements. However for increasing N_A the activation energy in doped semiconductors decreases according to $\epsilon_1 = \Delta E [1 - (N_A/N_{crit})^{1/3}] = 14$ meV with N_{crit} the critical density of the MIT. The fact that the measured ϵ_3 is still lower than the expected one and may be due to an impurity band strongly broadened towards the valence band. Now we can compare the experimental results with the theoretical expectations for the MIT. The metal-insulator transition is defined by the Mott criterion $a_B^* N_{crit}^{1/3} \approx 0.25$, with $a_B^* = 15$ Å

¹phone: +49-89-289-12778, fax: +49-89-3206620, email: matthew.grayson@wsi.tum.de

²Walther-Meißner-Institut für Tieftemperaturforschung

the effective Bohr radius. The critical transition density can be estimated to $N_{crit} = 5 \times 10^{18} \text{ cm}^{-3}$ for acceptors in p-type GaAs. The acceptor concentration $N_A^- = 1.1 \times 10^{18} \text{ cm}^{-3} < N_{crit}$ of sample p⁻ showing insulating behavior is well below the critical density of the MIT. In agreement with the Mott criterion the density $N_A^+ = 7.1 \times 10^{18} \text{ cm}^{-3} > N_{crit}$ of the p⁺ sample showing metallic behavior is above the critical density of the MIT.

We now turn our attention to two-dimensional hole gases (2DHG) in p-type heterostructures. To overcome the problem of the rough surface morphology of the p-type layers, we invented a new growth modulation technique for heterostructures. We studied the sample quality with measurements of the longitudinal and transverse resistance with a special focus on the low B-field Shubnikov-de Haas oscillations (SdH). The highest observed hole mobility is $\mu = 175000 \text{ cm}^2/\text{Vs}$ at a density of $p_{2D} = 2.4 \times 10^{11} \text{ cm}^{-2}$ indicating the excellent quality of the samples despite the doping layer with the poor morphology. An ungated sample shows very well developed quantum Hall plateaus and minima of the longitudinal resistance at 30 mK. In the low B-Field regime one can observe a beating of the SdH which is known from literature for 2DHGs to arise from zero-field spin splitting because of inversion asymmetry. By plotting R_{xx} against B^{-1} and Fourier transforming it in the low B-Field region one can directly deduce the density of $p_{2D}^L = 1.4 \times 10^{11} \text{ cm}^{-2}$ of the lower spin subband and the density $p_{2D}^U = 1.0 \times 10^{11} \text{ cm}^{-2}$ of the upper subband which add up to the total density evident at high B-fields $p_{2D} = 2.4 \times 10^{11} \text{ cm}^{-2}$. In addition we studied persistent photoconductivity (PPC) which is a common technique to increase the carrier density in two-dimensional electron systems (2DES) though it is uncommon in 2DHGs. We find a pronounced PPC effect in our samples. The unilluminated, dark density of the 2DHG at 4.2 K is $p_{2D} = 1.17 \times 10^{11} \text{ cm}^{-2}$ with a mobility of $\mu = 28000 \text{ cm}^2/\text{Vs}$. By illuminating a Hall-bar sample with a LED we were able to tune the density up to the maximum density of $p_{2D} = 2.3 \times 10^{11} \text{ cm}^{-2}$ with a mobility $\mu = 140000 \text{ cm}^2/\text{Vs}$ at 4.2 K. By using an L-shaped Hall-bar we investigate the mobility anisotropy of the two principal in-plane directions [1-10] and [001]. Up to a factor of 3-4 anisotropy has been observed in previous publications on the (110) and (311)A facet. In contrast, in our samples we observed only a very weak anisotropy mostly pronounced at low temperatures where it is within a factor of 1.1 to 1.3. From anisotropies in the bulk mass alone, one would expect a mobility anisotropy of a factor of 0.5, leaving open the possibility that anisotropic roughness may be counteracting the mass anisotropy.

In summary we characterized heavily auto-compensated Si-doped bulk (110) GaAs, and observed an insulating impurity band for a non-degenerate bulk p-type sample below the MIT, and metallic conduction for a degenerately doped sample. We were able to grow the first high mobility 2DHG on (110) oriented GaAs using Si as a dopant. We observed an unusual PPC and a weak anisotropy. High mobility MBE systems, equipped with Si as the *only* dopant source can take advantage of this new technique to grow 2DHGs on (110) oriented GaAs.

*Ref: F. Fischer, D. Schuh, M. Bichler, K. Neumaier, G. Abstreiter, and M. Grayson, accepted to Appl. Phys. Lett.

Highly Si-doped AlN grown by plasma assisted MBE

Martin Hermann¹, Florian Furtmayr, Martin Stutzmann, and Martin Eickhoff

Within the group III-nitride alloy system, AlN has the widest direct band gap of 6.2 eV , which makes it a useful material for optoelectronic applications in the UV spectral regime. For applications such as field emitters or UV-LEDs the achievement of controllable n-type conductivity is crucial. Silicon, known as a shallow donor in Ga-rich AlGaN alloys, is also considered as the preferable donor in AlN. However, because of the high ionization energy of Si in AlN, it is difficult to accomplish a significant conductivity. One possible approach is to increase the Si-concentration above the threshold for impurity band formation, estimated to occur at approximately 1 at. \% Si .

A study of the influence of the growth conditions on the Si incorporation in AlN layers grown by plasma assisted molecular beam epitaxy revealed a strong suppression of Si incorporation for metal-rich growth conditions. In this case the incoming Si is dissolved in a metallic Al film on top of the growing sample and therefore cannot be incorporated into the AlN layer. In contrast, N-rich growth conditions result in homo-geneous Si incorporation of up to $5.2 \times 10^{21}\text{ cm}^{-3}$ as measured by ERD analysis (c.f. Fig. 1). The apparent surface accumulation of Si for high doping concentrations can be attributed to the increased surface roughness of those layers. Moreover, the Si concentration increases in the same manner as the Si flux, indicating that no saturation occurs. The solubility limit of Si in AlN can be estimated to be larger than 5 at. \% .

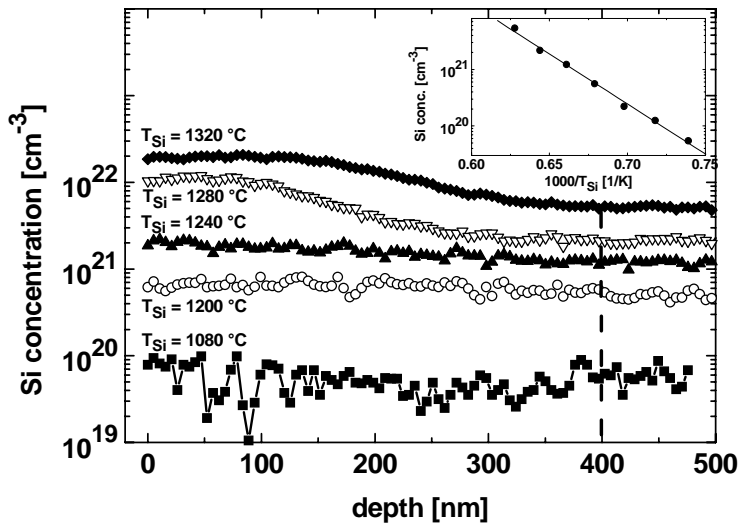


Fig. 1: Depth profiles of the Si concentration in AlN layers for different Si-cell temperatures T_{Si} . The inset shows an Arrhenius-plot of the Si-concentration at a depth of 400 nm . The slope of the linear fit shows the same behaviour as the flux of the Si-cell, indicating that no saturation occurs.

The influence of the Si concentration on the electronic properties of AlN:Si films grown under N-rich conditions was analyzed by temperature dependent Hall effect and conductivity measurements. Fig. 2 shows the room temperature conductivity for samples with different Si concentrations. Moderate Si-doping up to concentrations of $5 \times 10^{19}\text{ cm}^{-3}$ results in an increase of the room temperature conductivity, which is more than four orders of magnitude higher than in undoped samples ($< 10^{-9}\text{ }(\Omega\text{cm})^{-1}$). For higher Si-concentrations, the conductivity decreases again. However, an increase of $[Si]$ from $1 \times 10^{21}\text{ cm}^{-3}$ to $2.5 \times 10^{21}\text{ cm}^{-3}$ causes a further conductivity increase by four orders of magnitude.

¹phone: +49-89-289-12755, fax: +49-89-289-12737, email: hermann@wsi.tum.de

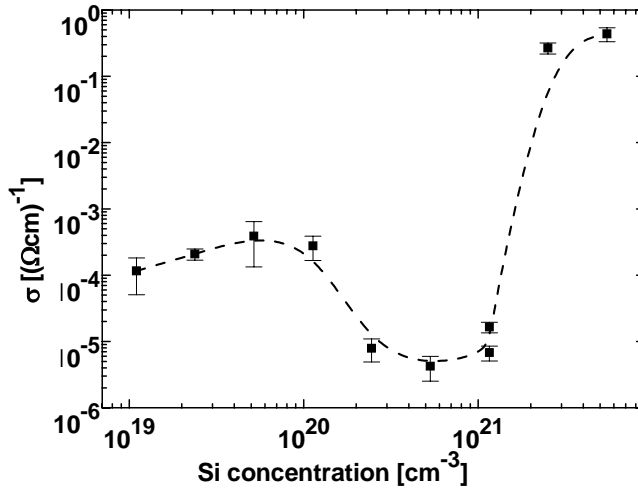


Fig. 2:
Room temperature conductivity for Si-doped AlN layers grown under N-rich conditions as a function of the Si concentration.

Fig. 3 displays the activation energy extracted from the temperature dependent conductivity and of the carrier density, measured between room temperature and 500°C. For moderate doping levels we found an increase of the activation energy from approximately 250 meV for $[Si] = 1.1 \times 10^{19} \text{ cm}^{-3}$ up to more than 500 meV for $[Si] = 1.2 \times 10^{21} \text{ cm}^{-3}$. Due to their high resistivity Hall analysis of the layers with $[Si] = 2.5 \times 10^{20} \text{ cm}^{-3}$ and $2.3 \times 10^{20} \text{ cm}^{-3}$ was not possible. It should be noted that in some samples we have observed slightly different activation energies for temperatures above 500°C. We attribute this behavior to the simultaneous influence of residual oxygen with a concentration comparable to $[Si]$. For $[Si] > 1.2 \times 10^{21} \text{ cm}^{-3}$ we observed a drastic reduction in the activation energy, which correlates with the increase in conductivity described in Fig. 2.

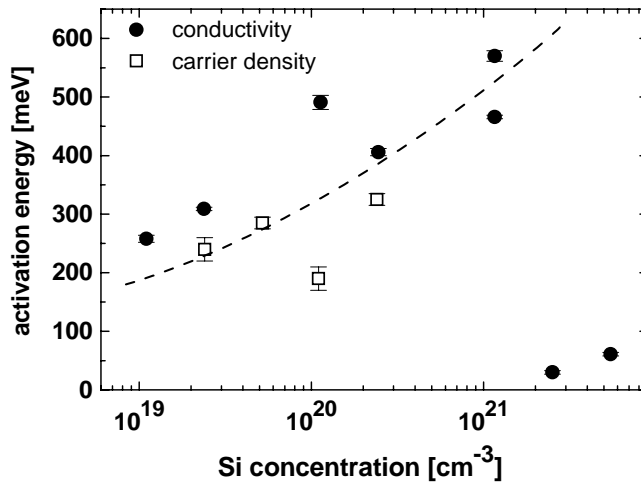


Fig. 3:
Activation energy of the conductivity and the free carrier density in Si-doped AlN grown in the N-rich regime as a function of $[Si]$.

An increase of the activation energy and a decrease in conductivity for intermediate Si-concentrations as shown in Fig. 2 can be attributed to self compensation due to the formation of deep centers. The sudden decrease of the activation energy for the highest Si-concentrations, which is accompanied by an increase in conductivity by four orders of magnitude, can be explained by the formation of an impurity band.

Low-resistive ohmic contacts to *n*-type GaSb using a highly doped n^+ -InAsSb contact layer

Christian Lauer¹, Oliver Dier, and Markus-Christian Amann

GaSb-based semiconductor diode lasers with emission wavelengths above $2\mu\text{m}$ are interesting light sources for tunable diode lasers absorption spectroscopy applications (TDLAS) and a lot of effort was put into the development of these devices. A limiting constraint in device design is still posed by the lack of low-resistive metal-to-*n*-GaSb contacts. Whereas *p*-type contacts to GaSb exhibit extremely low contact resistivities well below $10^{-6}\Omega\text{cm}^2$ (partly due to the high possible Be-doping concentration of $> 10^{20}\text{cm}^{-3}$), the Te-doping concentration in *n*-type GaSb is limited to $2 \times 10^{18}\text{cm}^{-3}$. In addition, the contacts suffer from a Fermi level pinning near the valence band edge, causing a high Schottky barrier. Ohmic tunneling contacts are usually fabricated by diffusing dopant atoms (e.g. Ge) from the metallization into the superficial semiconductor layer to induce high doping and a thin depletion region. The resulting contact resistivities are very sensitive to the employed metallization sequence and process control during diffusion. In addition, the surface of GaSb-based materials rapidly oxidizes in atmospheric oxygen and deionized water. Therefore the common procedure of applying an acidic dip to remove the native oxide layer prior to deposition of the metallization turns out to have almost no effect on the final contact resistivity. The best result so far ($1.4 \times 10^{-6}\Omega\text{cm}^2$) was achieved by another group with a metallization sequence containing Pd to reduce the native oxide, Ge as dopant, and In to produce InGaSb close to the surface during annealing, providing a lower barrier for the electron transport. Unfortunately, none of the contacts presented so far shows ohmic behavior without the annealing step necessary for dopant diffusion. This annealing step might not be tolerable for all device designs due to deep in-diffusion of dopants, out-diffusion of Sb, and deep reaching material damage.

To avoid a hard annealing step, our group suggests a contact to *n*-GaSb using an intermediate epitaxial InAsSb layer which can be Te-doped above $1 \times 10^{20}\text{cm}^{-3}$. The contacted GaSb layer below is Te-doped with a concentration of $5 \times 10^{17}\text{cm}^{-3}$. The native oxide on the sample is removed by sputter etching with an Ar plasma and deposition of the metallization takes place in the same chamber by sputtering. Thus we prevent exposure of the sample surface to oxygen and avoid reoxidation. Pt serves as the contact metal. Unfortunately, tests of Pt and Pd based contacts revealed unsatisfying adhesion to dielectrics like SiO_2 , making device application difficult. To improve adhesion we first deposit a very thin Ti layer with a thickness below 1nm and then 35nm of Pt as contact metal and diffusion barrier for the following 250nm of Au. Finally the contacts can be slightly annealed to further improve adhesion, but the concept does not rely on diffusion processes, thus minimizing structural damage inside the device. Significant damage only occurs if the annealing temperature becomes too high ($>400^\circ\text{C}$) to prevent diffusion of Au through the Pt barrier into the semiconductor or of the Te dopant from the epitaxial contact layer.

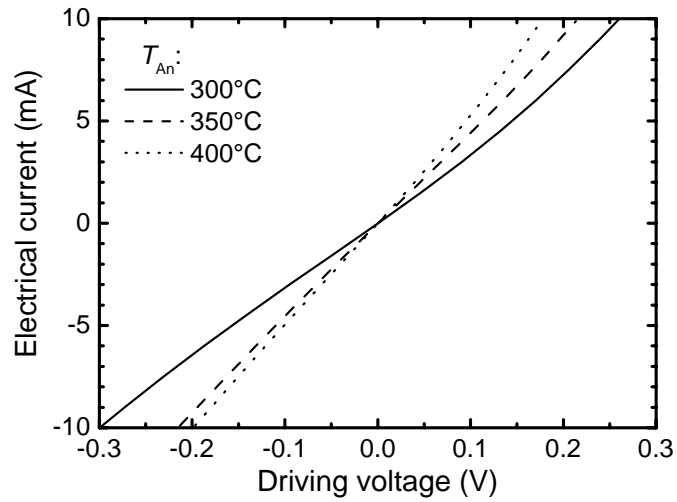
If the native oxide layer is not removed from the sample surface the contacts do only show ohmic behavior after an annealing step. The resulting current-voltage (*IV*-) characteristics of test structures are shown in Fig. 1. They have a circular contact area of $5\mu\text{m}$ in diameter and were annealed at 300°C , 350°C , and 400°C for 90s under gas flows of 4slm of N_2 and 1slm of H_2 . Taking into account the contribution of the underlying substrate on

¹phone: +49-89-289-12788, fax: +49-89-3206620, email: lauer@wsi.tum.de

the measurement, contact resistivities of $6.6 \times 10^{-6} \Omega\text{cm}^2$ (300°C), $1.8 \times 10^{-6} \Omega\text{cm}^2$ (350°C), and a record-low $9.6 \times 10^{-7} \Omega\text{cm}^2$ (400°C) can be extracted from the *IV*-curves.

Fig. 1:

Current vs. voltage for circular contact test structures with a diameter of $5 \mu\text{m}$ after annealing for 90s at temperatures of 300°C, 350°C, and 400°C, respectively. The native oxide layer was not removed from the sample surface before deposition of the metallization.



If the native oxide is removed by sputter etching to a depth of 4nm or 8nm the contacts show ohmic behavior even without an annealing step. The extracted contact resistivities amount to $4.3 \times 10^{-6} \Omega\text{cm}^2$ (4nm) and $5.1 \times 10^{-6} \Omega\text{cm}^2$ (8nm), respectively. To our knowledge these are the first metal to *n*-GaSb contacts to exhibit ohmic behavior without an annealing step. The sputter etching process seems to induce crystal damages to the semiconductor, thus deteriorating the resistivity for deeper etching. The native oxide is normally thinner than 2nm and a reduction of the etch depth and the resulting crystal damage should further improve the results. If the contacts are slightly annealed for 90s at 350°C the values improve to $2.8 \times 10^{-6} \Omega\text{cm}^2$ (4nm) and $3.4 \times 10^{-6} \Omega\text{cm}^2$ (8nm), respectively (see Fig. 2).

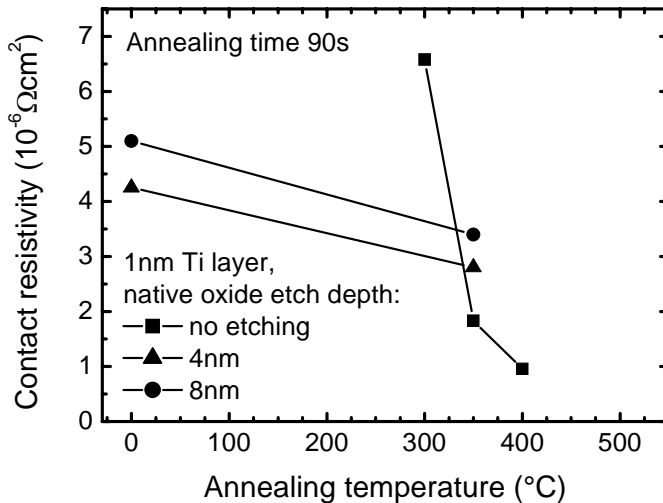


Fig. 2:

*Contact resistivity of Ti/Pt/Au contacts to n^+ -InAsSb/*n*-GaSb after annealing for 90s at different temperatures. The native superficial oxide on the three samples was left untreated (squares) or removed by sputter etching to a depth of 4nm (triangles) and 8nm (circles), respectively. At temperatures above $\sim 420^\circ\text{C}$ the contacts are destroyed by metal diffusion.*

A simulation of the band bending shows a significant peak in the conduction band at the interface between the InAsSb contact layer and the underlying GaSb layer. This peak extends to 0.7eV above the Fermi level and explains the slight nonlinearity in the *IV*-characteristics displayed in Fig. 1. Further improvement of the contacts is expected if this peak can be reduced using a grading between the two materials.

Nanometer spaced electrodes on a cleaved AlGaAs surface

Sebastian M. Luber,¹ Sebastian Strobel, Hans-Peter Tranitz², Werner Wegscheider², Dieter Schuh, and Marc Tornow

Novel hybrid structures combining inorganic substrates and functionally designed molecular units are of high prospect for future molecular nanoelectronics. One of the major challenges is the preparation of well defined contacts, often termed nanogap electrodes, that allow to reliably contact and electrically investigate molecules of a given size. A variety of methods have already been demonstrated to be very well suited for contacting nano-scale objects. However, applications which require at the same time macroscopically flat surfaces with a pre-designed gap separation between symmetric, coplanar electrodes can hardly be addressed. Such properties are particularly important for the manipulation, positioning and electrical investigation of molecules on or between electrodes by, e.g., scanning probe techniques. We present a novel fabrication method that combines the benefits of using only conventional process technology for lateral patterning with the precision, cleanness and smoothness of a cleaved AlGaAs/GaAs heterostructure grown by molecular beam epitaxy (MBE). As the crystallographic cleavage is done after finishing the micro-patterning of the device, the sensitive nanogap region is protected from any organic contamination during all lithographic process steps.

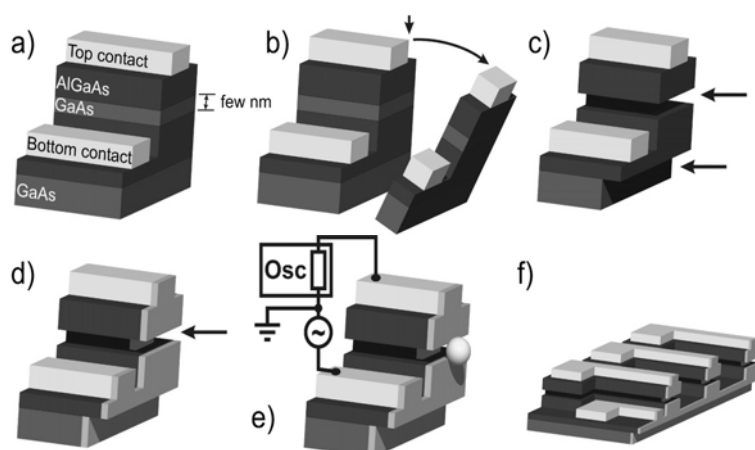


Fig. 1: Schematic showing the fabrication process. (a) AlGaAs-GaAs heterostructure after mesa etching and deposition of contact pads. (b) Cleavage of the sandwich structure. (c) Selective etching of the GaAs layer. (d) Deposition of a thin film metal layer. (e) Experimental setup to trap single polarizable nanoparticles between the electrodes. (f) Linear array of parallel processed electrode structures

Starting material for the AlGaAs-GaAs heterostructure are epi-ready (001) GaAs wafers. For the lower electrode a 1000nm thick $\text{Al}_{0.3}\text{Ga}_{0.7}\text{As}$ layer is MBE grown on the semi-insulating GaAs substrate followed by a thin GaAs layer which later defines the electrode distance. Then a 500nm AlGaAs layer is deposited which is later used as support for the top electrode. After that, the lateral patterning of the heterostructure is carried out by conventional optical lithography only. For the integration of a larger number of nanogap devices on one chip finger-like structures were patterned using standard optical lithography and wet etching. Then, electrical Ti/Au contact pads were deposited (cf. fig. 1(a)). By cleaving the substrate, an atomically flat and perfectly clean (110) surface of the AlGaAs-

¹ phone : +49-89-289-12776, fax : +49-89-3206620, email : luber@wsi.tum.de

² Institut für Angewandte und Experimentelle Physik, Universität Regensburg, 93040 Regensburg, Germany

GaAs sandwich structure is exposed (fig. 1(b)). After that, the embedded GaAs layer is etched selectively versus the outer AlGaAs layers using citric acid and H_2O_2 (5:1) (fig. 1(c)). After that, the electrode forming thin film metal layer (5nm Ti / 8nm Au) is evaporated perpendicularly to the cleaved surface (fig. 1(d)). The electrical contact between the top and the bottom electrode is interrupted at the AlGaAs-GaAs interface edge thereby separating the two nanogap electrodes. The final gap size between the electrodes is only determined by the layer sequence set during MBE growth, the minor roughening and widening of the AlGaAs-GaAs interface due to non-perfect selective etching and the lateral roughness of the thin film metal layer. We tested the electrical functionality of the device by trapping single gold nanoparticles using the electrical setup depicted in figure 1(e) as will be described later. Figure 1(f) shows a completely processed multi-finger structure with nanometer separated electrodes at every end of a finger where each top electrode can be addressed individually.

To prove the smoothness of the electrode surface we characterized completely processed devices with an atomic force microscope (AFM). Typical values for the maximum surface corrugation of the metal layer are below 1.2nm at both sides of the gap. We also analyzed the electrode distance as it is slightly oscillating due to the non perfect selective etching of the GaAs vs. the AlGaAs layer and the metal roughness, and measured a maximum deviation of typically less than 2.1nm from the mean value of 22.5nm for a device with 20nm GaAs layer. To illustrate the application of our device to contact nanoscale objects we recorded current-voltage (IV) characteristics before and after positioning a single metal colloid particle on the gap. Prior to any modification the electrodes showed a very good insulating behavior at liquid helium temperature (4.2K) with resistances exceeding $10\text{G}\Omega$. We subsequently positioned gold nanoparticles between the electrodes using an electrical trapping method. Here, the sample is immersed in a diluted colloidal solution of polarizable particles, and an oscillating voltage is applied to the electrodes with a series resistor included in the circuit (cf. fig. 1(e)). The non-uniform alternating electric field between the electrodes attracts the particles due to a dielectrophoretic force, a process which self-terminates after the successful trapping. Typical electrical characterization data of a sample with a 20 nm GaAs layer before and after trapping are displayed in figure 2. Clearly, the I-V characteristics change from very good electrode isolation ($\sim 11\text{G}\Omega$) to a clean short-circuit, as indicated by a decrease of the resistance over more than six orders of magnitude (at $T=4.2\text{K}$). The trapping of only a single gold cluster was verified by scanning electron microscopy (SEM).

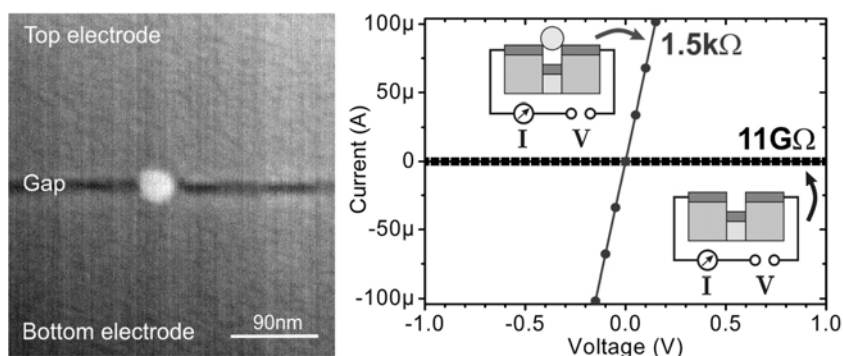


Fig. 2: *Left:* Typical SEM picture of a single 30nm gold particle trapped between the electrodes of a device with a 20nm GaAs layer. *Right:* I-V characteristics before (■) and after (●) trapping a single Au nanoparticle

Growth and characterization of Mn-doped Ge

Thomas Vallaitis¹, Mario Gjukic, Martin S. Brandt, and Martin Stutzmann

Most of the proposed applications of spintronic devices require the injection of a highly spin-polarized current into semiconductor structures. Ferromagnetic metals on semiconductors fail to achieve high degrees of polarization because of a large mismatch in specific resistivities and scattering processes at the metal-semiconductor interface. Additionally, the heteroepitaxial growth of metal-semiconductor-metal structures has proven to be very difficult. A promising approach to overcome these intrinsic problems is the use of diluted magnetic semiconductors (DMS), which are a combination of well-known semiconductors and the magnetic properties of transition-metal ions. While a lot of progress has been achieved for II-VI and III-V based DMS, compatibility with existing group IV semiconductor technology is desired for many applications, eg. for quantum logic gates. Inspired by first publications on $\text{Ge}_{1-x}\text{Mn}_x$, where a Curie temperature of 116 K has been reported for a manganese concentration of 3.5 at.%, we have investigated this material system.

Using low-temperature molecular beam epitaxy (LT-MBE), numerous $\text{Ge}_{1-x}\text{Mn}_x$ samples were grown on Ge(100) and quartz substrates, where the manganese concentration, the substrate temperature, and the germanium flux were varied systematically and independently. The manganese content has been determined by energy-dispersive X-ray spectroscopy (EDX) and elastic recoil detection (ERD). Structural, electronic and magnetic properties of the samples have been investigated using atomic-force microscopy (AFM), Raman scattering, UV/Vis reflection spectroscopy, conductivity measurements, and superconducting quantum-interference device (SQUID) magnetization measurements.

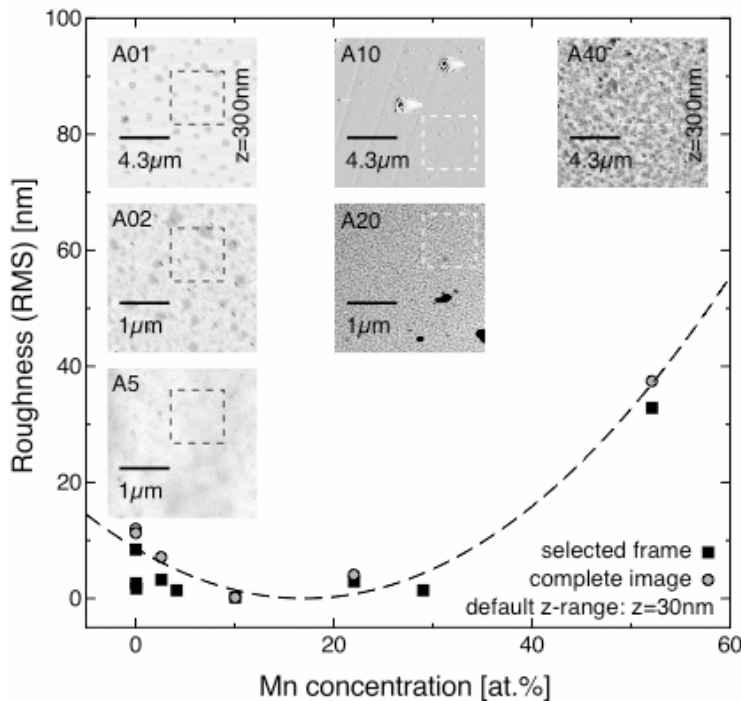


Fig. 1: RMS surface roughness for samples grown at 225°C with a Ge growth rate of 1 Å/s as determined by atomic force microscopy (inset). A minimal roughness of 1 nm is observed for a manganese concentration around 10 at.%.

¹phone: +49-89-289-12739, fax: +49-89-12737, email: thomas.vallaitis@wsi.tum.de

Fig. 1 shows the RMS surface roughness as a function of the manganese concentration for samples grown at 225°C with a germanium growth rate of 1 Å/s. The small AFM images illustrate the gradual transition of the crystal growth regime from distinct island growth to an island-layer growth and back to island growth for high manganese concentrations. The minimum of the roughness indicates a good crystalline quality for manganese concentrations up to 20 at.%, which has been confirmed by Raman and UV/Vis spectroscopy.

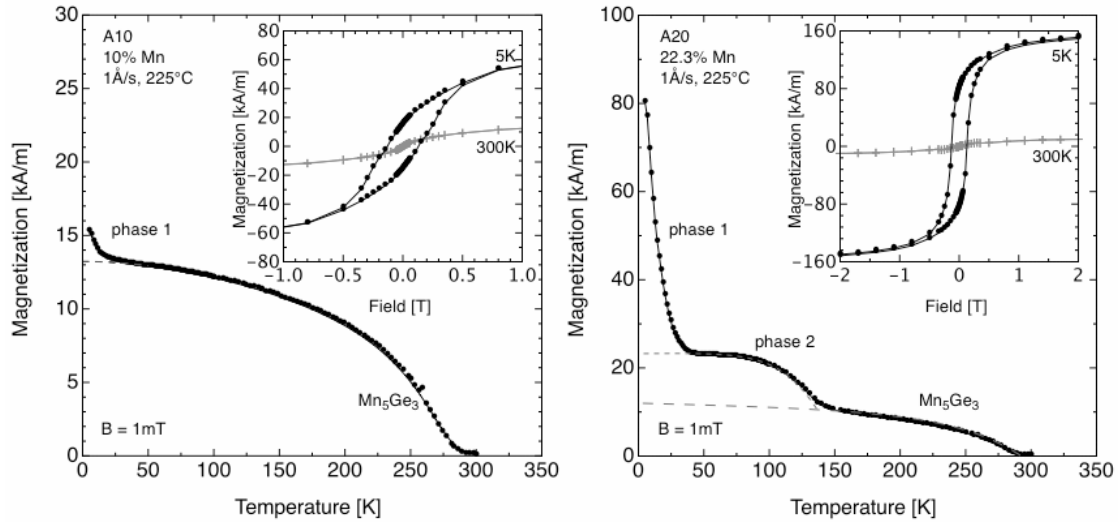


Fig. 2:

SQUID magnetization measurements for samples with a manganese concentration of 10 (left) and 20 at.% (right), grown at 225°C and with a Ge growth rate of 1 Å/s. Both samples exhibit ferromagnetic behavior up to room temperature, which is attributed to the ferromagnetic Mn₅Ge₃ phase. Phases 1 and 2, which are observed below 150 K, are previously unknown magnetic phases.

Temperature dependent SQUID magnetization measurements (Fig. 2) reveal ferromagnetic behavior for samples with manganese concentrations above 1 at.%. The dominant contribution is attributed to metallic ferromagnetic Mn₅Ge₃ clusters. Samples with a high manganese content show a significantly enhanced paramagnetic phase 1 below 30 K. Additionally, a second magnetic phase is found for a manganese concentration of 20 at.%. It shows the characteristic shape of a ferromagnet with a Curie temperature of 140 K and cannot be attributed to any known intermetallic phase in the Ge-Mn material system. The deviation of the hysteresis loops from the ideal ferromagnetic case as well as Raman measurements which show structural inhomogeneities on a micrometer scale indicate the presence of intermetallic magnetic inclusions. Phases 1 and 2 are found to be thermodynamically unstable and transfer to Mn₅Ge₃ clusters upon annealing at 150°C for 166 hours.

In summary, we observe a rich but complicated multi-phase behavior of our GeMn alloys, with no clear proof of a germanium-based DMS. Careful optimization of the growth parameters might avoid the formation of ferromagnetic inclusions and allow the investigation of the bulk properties of dilute magnetic Ge_{1-x}Mn_x.

Hydrosilylation of silicon nanoparticles

Andrea Baumer¹, Martin Stutzmann, and Martin S. Brandt

The continuous trend in electronics and optoelectronics to reduce device sizes down to nanometer scales has led to wide ranging scientific interest in nanoparticles. Especially, the discovery of visible photoluminescence from Si nanoparticles and nanowires attracted a great deal of attention as it renews the hope to integrate light-emitting devices based on Si with the well-established microelectronics technology. Due to the large surface/bulk ratio of nanoparticles, their surface properties are of particular importance for their use in electronic devices. The influence of different surface terminations such as H termination or alkyl termination on the electronic properties of crystalline Si has been known for some time. In this work, we present a study on the surface functionalization of Si nanoparticles by alkyl termination via thermally-induced hydrosilylation which is a well-established chemical method for direct covalent attachment of alkenes on H-terminated Si surfaces [1].

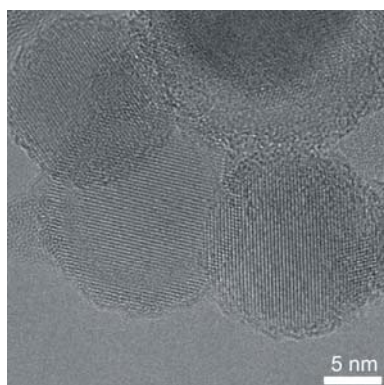


Fig. 1:
TEM image of some characteristic Si nanoparticles produced by plasma deposition. The crystalline Si core is surrounded by an amorphous SiO₂ shell.

The Si nanoparticles were produced by microwave plasma synthesis at the Institut für Verbrennung und Gasdynamik at the Universität Duisburg-Essen. Transmission electron microscopy (TEM) shows that the nanoparticles have a mean diameter of 20 nm and consist of a round, mostly unfaçeted crystalline Si core surrounded by an amorphous shell (Fig. 1). Fourier-transform infrared (FTIR) spectroscopy was performed to study the chemical composition of the as-grown particles. A very broad peak around 1080 cm⁻¹ and a peak at 1180 cm⁻¹ are found in the IR absorbance spectrum (Fig. 2 b)) due to symmetric and asymmetric Si-O-Si stretching vibrations, respectively and indicate the presence of a large amount of oxide. At 2100 cm⁻¹, H-Si-(Si,Si,Si) stretching vibrations are observed. By subsequent substitution of the three backbonded Si atoms by O atoms, this stretching mode is shifted to larger wavenumbers. For three backbonded O atoms

(H-Si-(O,O,O)), the stretching mode is observed at 2250 cm⁻¹. The comparatively large IR absorbance due to H stretching vibrations clearly shows that the as-grown particles are not covered with oxide alone. Rather, there also exist H-terminated Si atoms which are most likely generated during the plasma growth process where an excess of H₂ is used.

To remove the oxide coverage, HF etching was performed. In comparison to the as-grown particles, both the peaks at 1080 cm⁻¹ and at 2250 cm⁻¹ have clearly decreased in intensity but have not disappeared completely indicating some remaining oxide or native oxide freshly grown after the HF treatment on the surface. The most likely origin for the remaining oxide are clustered nanoparticles in which some parts of the particles are protected against the attack by HF. H termination is clearly shown by the increase of the H-Si-(Si,Si,Si) peak at 2100 cm⁻¹ and the appearance of the SiH₂ scissors mode at 906 cm⁻¹.

¹phone: +49-89-289-12769, fax: +49-89-289-12739, email: baumer@wsi.tum.de

For alkyl termination, Si nanoparticles were immersed in a small amount of HF, an excess of 1-octadecene was added and the particles were treated under permanent stirring and bubbling with N₂ for 90 min at 150°C. After careful cleaning, the particles were dried with N₂. Octadecanyl-terminated surfaces also were produced without adding HF during the hydrosilylation. In this case, the as-grown Si nanoparticles were immersed directly in 1-octadecene. The FTIR spectra of the hydrosilylated nanoparticles are shown in Fig. 2 in comparison to the H-terminated and as-grown samples, respectively. Sharp, aliphatic C-H stretching bands in the region of 2850-2960 cm⁻¹ and weaker C-H deformation bands at 1350-1470 cm⁻¹ appear in the spectra, while the H-terminated and as-grown samples just show very small aliphatic bands which can be attributed to carbon contaminations. Further, the Si-H stretching vibration at 2100 cm⁻¹ clearly decreases during hydrosilylation. One can estimate the efficiency of hydrosilylation from the relative consumption of the Si-H groups by comparing the integrals of the Si-H peak at 2100 cm⁻¹ before and after hydrosilylation. For the sample hydrosilylated in the presence of HF (Fig. 2 a), one obtains a hydrosilylation efficiency of 36%. Due to the presence of Si-H bonds, hydrosilylation is also possible on the as-grown, predominantly oxidized nanoparticles. The hydrosilylation efficiency in this case (Fig. 2 b)) is estimated to a similar value of 37%.

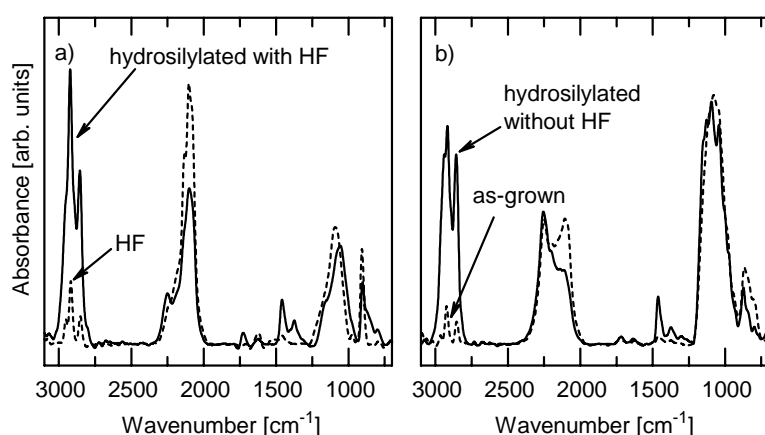


Fig. 2: FTIR spectra of alkyl-terminated Si nanoparticles which were synthesized a) with and b) without the addition of HF. In both cases, peaks due to alkyl chains appear in the spectra while the Si-H peak at 2100 cm⁻¹ decreases.

For use of nanoparticles in electronic devices and in particular for their easy manufacturability, the structural stability of the functionalized surfaces in ambient atmosphere is of enormous importance. Therefore, the behavior of the H-terminated and the alkyl-terminated nanoparticles in air has been studied by successive FTIR measurements. While H termination of the Si nanoparticles was found to be stable in ambient atmosphere for at least some hours, the resistance against oxidation could be further improved by alkyl termination, namely by more than a factor of two. Thus, hydrosilylation might be an interesting method to enhance the resistance against oxidation, while obtaining good electronic properties with low defect densities [2].

In cooperation with F. M. Petrat (Creavis GmbH/ Degussa AG) and H. Wiggers (Univ. Duisburg-Essen).

[1] J. M. Buriak, Chem. Rev. **102**, 1271 (2002)

[2] A. Baumer et al., submitted

Hydrogen/deuterium passivation of Al-doped polycrystalline silicon–germanium alloys

Mario Gjukic¹, Peter Klement, and Martin Stutzmann

The beneficial effects of hydrogen on the structural and electronic properties of semiconductors were first discovered in intrinsic germanium, but most of the experimental work has been performed on hydrogen in silicon. In crystalline silicon, for example, the electrical activity of shallow and deep defects was neutralized up to 99% after exposure to a hydrogen plasma. Moreover, in disordered or partly disordered semiconductors such as amorphous or microcrystalline silicon, atomic hydrogen successfully passivates structural defects and, therefore, improves the optical and electrical properties of the material to a device quality level.

Over the years, an accepted picture concerning the microscopic structure and the electronic states of hydrogen in crystalline silicon has emerged. As an impurity in crystalline silicon, atomic hydrogen can be found in the positive (H^+), the neutral (H^0), and the negative (H^-) charge state, respectively. The interstitial positions of hydrogen within the diamond crystal lattice of silicon have been assessed by a variety of theoretical calculations and muon spin rotation experiments. As a result, H^+ is preferentially located at the bond center (BC) site, building a three-center bond with the two nearest silicon atoms. This also holds for the metastable H^0 , while H^- is preferentially located at the tetrahedral (T) site, a lattice position with low electronic charge density. The energetic position of the $H^{+/-}$ charge transfer level was calculated to be in the middle of the band gap of crystalline silicon, approximately 0.4 eV above the valence band edge. In p -type silicon, hydrogen behaves as a donor (H^+) and in n -type as an acceptor (H^-), leading to a decrease of free charge carrier concentration and, consequently, to a lower sample conductivity.

As for to the passivation of shallow defects in crystalline semiconductors, important differences have been reported for the passivation behavior of acceptors and donors in silicon and germanium, respectively. While hydrogen passivates both donors and acceptors in silicon, only donor passivation was reported for crystalline germanium. Based on steric and electrostatic arguments, Estreicher *et al.* have calculated the relative stability of various interstitial sites for hydrogen in different group IV host materials. As a result, the BC site is lower in energy than the T site in diamond and crystalline silicon. In crystalline germanium, however, the T site becomes the absolute energy minimum. On this lattice position hydrogen is preferentially in the H^0 or H^- charge state and acts rather as an acceptor, leading only to the passivation of donors or deep defect states. A similar conclusion can be drawn from the results of Van de Walle *et al.* Here, the energetic position of the $H^{+/-}$ charge transfer level in germanium was determined to be located at the valence band edge. Thus, for a Fermi position between the valence and the conduction band edge, hydrogen is never in the H^+ charge state and, therefore, not able to passivate shallow acceptor states. Theoretical calculations or experimental information on acceptor passivation in crystalline silicon–germanium alloys is missing completely up to now.

We have investigated the incorporation of deuterium into thin polycrystalline silicon–germanium films from a plasma source as a function of the sample temperature during the plasma treatment and in particular the chemical composition of the binary alloy. The samples under investigation have been prepared on quartz substrates by aluminum-induced

¹phone: +49-89-289-12783, fax: +49-89-289-12739, email: gjukic@wsi.tum.de

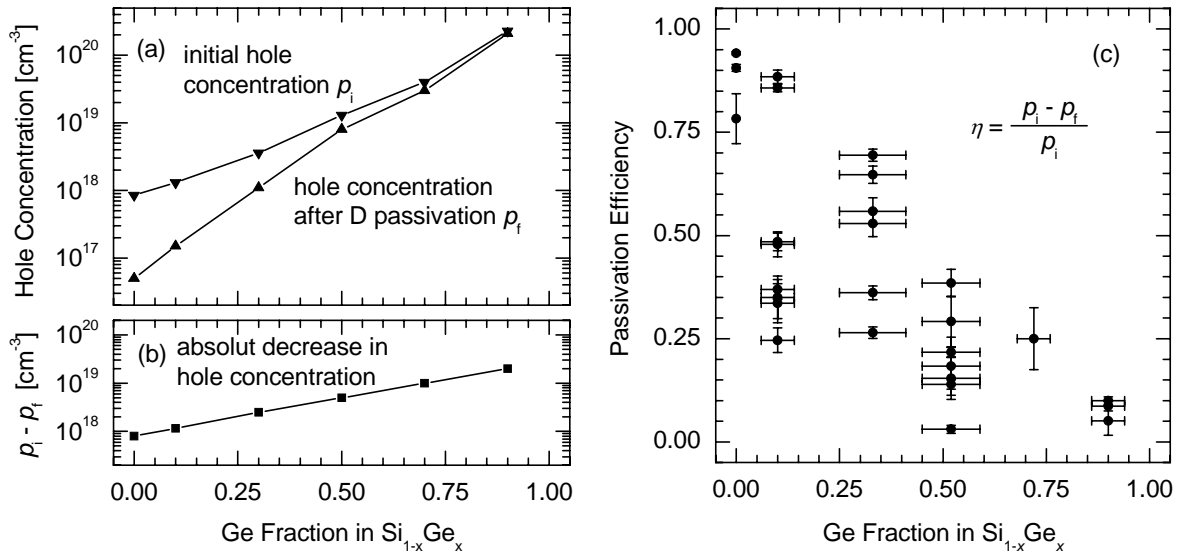


Fig. 1: (a) Room temperature hole concentrations derived from Hall effect measurements for Al-doped poly-Si_{1-x}Ge_x samples before and after deuterium passivation. Shown are the samples where the highest passivation efficiency was achieved. (b) The absolute number of passivated acceptors increases from poly-Si to poly-Si_{0.1}Ge_{0.9}. (c) The right graph shows the results for samples treated under different conditions. The passivation efficiency decreases from 94% for Si to about 10% in the case of Si_{1-x}Ge_x with a germanium concentration of 90 at.%.

crystallization of amorphous silicon–germanium. Due to the intimate contact with aluminum during crystallization, the samples are doped with aluminum, which is a shallow acceptor in silicon–germanium. Some of the data obtained from these measurements are presented in Fig. 1. The initial hole density, p_i , is reduced to a final density, p_f , after passivation, strongly dependent on the germanium content. The absolute amount of acceptors passivated upon deuterium plasma exposure increases with increasing germanium concentration, whereas the relative passivation efficiency, defined as $(p_i - p_f)/p_i$, decreases almost linearly. The results obtained for pure silicon and germanium, respectively are in accordance with previous reports on acceptor passivation in silicon and germanium. The linear decrease of passivation efficiency with increasing germanium concentration, however, is a new result which has to be explained by the different existing models.

Van de Walle *et al.* have also determined the position of the H^{+/-} charge transfer level in a wide range of host materials. According to these calculations, the electronic transition level of hydrogen is almost independent of the host material at an energy of 4.5 eV below the reference vacuum level. A similar dependence was observed for transition metal impurities in III/V semiconductors by Langer and Heinrich. Taking the valence band offset between silicon and germanium, and a constant H^{+/-} charge transfer level into account, a strong decrease of the passivation efficiency would be expected only for germanium concentrations of 45–55 at.%. An alternative interpretation can be made based on the different microscopic environments of aluminum acceptors in a silicon–germanium alloy.

Theoretical study of pH response of electrolyte AlGaN/GaN ion sensors

Michael Bayer, Christian Uhl, Stefan Birner¹, and Peter Vogl

The concept of detecting salt concentrations and charged bio-molecules by semiconductor devices has stimulated a rapidly growing field of semiconductor based ion sensors. Requirements for physiological applications of such devices are chemically inert oxide surfaces and non-toxic materials. Thus a highly promising material system is $\text{Al}_x\text{Ga}_{1-x}\text{N}$ that additionally is extremely sensitive to changes of the surface charge or surface potential due to its high piezo and pyroelectric fields. We have developed a model to explain and predict the sensitivity of solution gate AlGaN/GaN field effect transistors (FET) to charged adsorbates at the semiconductor/electrolyte interface that are controlled by the pH value of the electrolyte. Invoking the site-binding model for the chemical reactions at the oxidic semiconductor-electrolyte interface and taking into account strain, deformation potentials and the piezo- and pyroelectric polarizations that result in interfacial sheet charge densities within the nitride heterostructure (Fig. 1), the spatial charge and potential distribution have been calculated self-consistently both in the semiconductor and the electrolyte. In addition, we calculated the source-drain current and its sensitivity to the electrolyte's pH value.

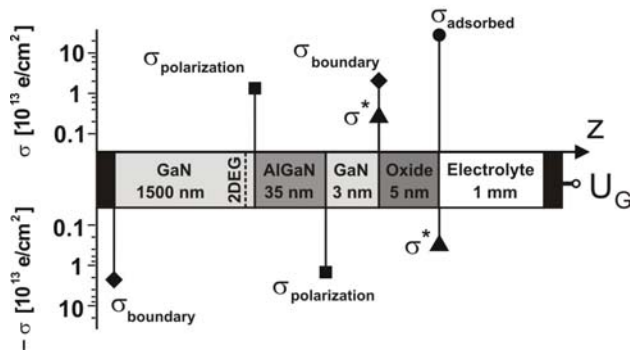


Fig. 1:

Schematic layout of the calculated heterostructure (Ga-face polarity) where the electrolyte is placed on top of a Ga oxide. The interface charge densities and their magnitudes in units of 10^{13} e/cm^2 are indicated by closed symbols and the axis to the left. A gate voltage U_G can be applied to the electrolyte. The position of the 2DEG is indicated.

The charge distribution at any point within the electrolyte solution that may contain several different types of ions is governed by the potential (Fig. 2) that is determined by the Poisson-Boltzmann equation, involving the valency and concentration of each ion species. Because of adsorption or desorption of hydrogen ions at oxide surface sites, the oxide/electrolyte interface gets either positively or negatively charged. To calculate this charge, the site-binding model for amphoteric surfaces was employed. Here, hydroxyl groups at the surface sites get either protonized or deprotonized. The adsorbed oxide/electrolyte interface charge σ_{adsorbed} depends on two dissociation constants for describing the surface reactions, the pH value of the electrolyte and the potential at the oxide/electrolyte interface. Experimental results were used to determine the values of the relevant dissociation constants and the concentration of the sites on the oxide. We varied the pH value of the electrolyte solution and calculated the adsorbed surface charges (Fig. 3a) which influence the electrostatic potential and thus the spatial variation of the conduction band edge. The huge piezo and pyroelectric polarization fields lead to the formation of a two-dimensional electron gas (2DEG) as indicated in Fig. 1 with an integrated sheet density of the order of 10^{13} cm^{-2} . The relevant part in the semiconductor is the density of the 2DEG that responds sensitively to changes in the electrolyte, i.e. changes in the pH value.

¹phone: +49-89-289-12752, fax: +49-89-289-12737, email: stefan.birner@nextnano.de

We calculated the 2DEG density (Fig. 3b) and the source-drain current of this AlGaIn/GaN FET parallel to the interface as a function of the surface charge density that arises from chemical reactions at the Ga oxide layer that is exposed to the electrolyte.

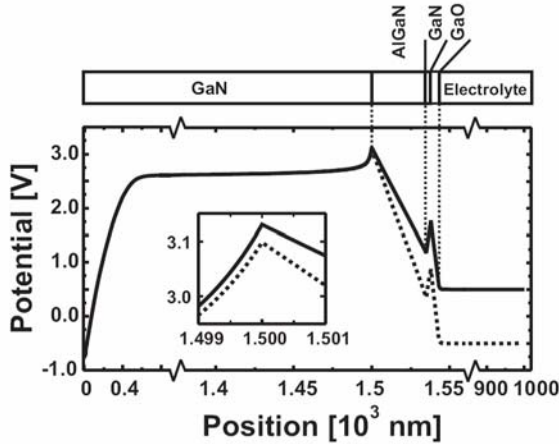


Fig. 2:

Spatial potential distribution for the entire structure with an electrolyte of pH=5.3 as calculated by the Poisson-Boltzmann equation. Depicted are the cases for an electrolyte gate voltage of $U_G=0.5$ V (solid line) and $U_G=-0.5$ V (dotted line), respectively. The inset shows a blow-up of the potential near the position of the 2DEG and illustrates the effect of an externally applied bias.

In order to reproduce recent experimental results we had to take into account an additional charge σ^* (Fig. 1) at the inner oxide surface that is essential for the sensitivity of the device because it effects the 2DEG density. Since experiments on the oxide growth on GaN have indicated voids in the oxide surface, some of the adsorbed ions can reach the inner oxide surface. The best agreement with the experimentally obtained I-V curve was obtained by assuming this charge to be 2% of the actual oxide/electrolyte interface charge. Our model can be used to enhance the efficiency of the sensor systematically by increasing the oxide thickness or by decreasing the Al mole fraction in the AlGaIn layer. For a structure of N-face polarity, we found that the response of the 2DEG density to changes in the pH value as well as the applied voltage is larger and provides a more efficient control of the device. Our calculations show a significant enhancement in the variation of the 2DEG density as a function of the pH value as compared to the Ga-face structure. All computations have been carried out using the nano device simulation tool `nextnano3` [1].

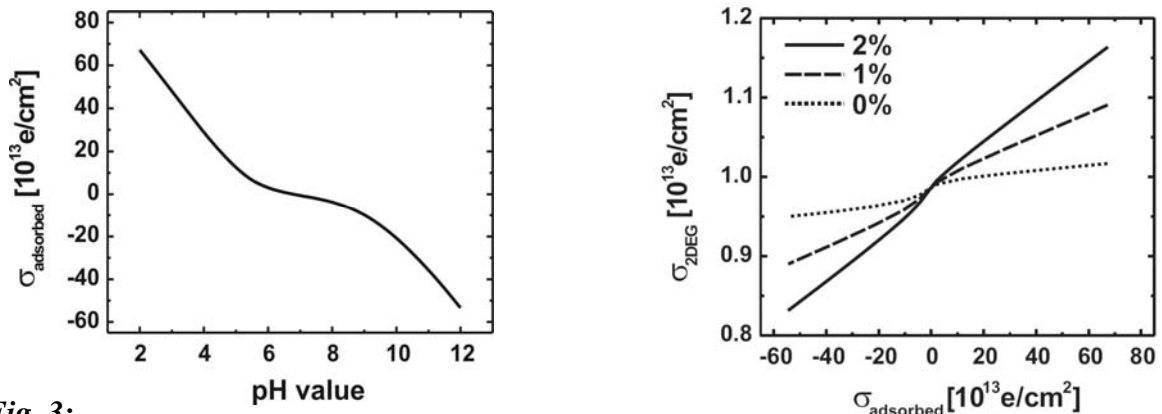


Fig. 3:

a) Calculated variation of the oxide/electrolyte interface charge density σ_{adsorbed} of the amphoteric surface with the pH value. As one can see, there is a range of pH values where the net surface charge is close to zero. Nevertheless, within this range the 2DEG density still varies as it also depends on the surface potential.

b) The 2DEG density as a function of the interface charge σ_{adsorbed} for different values of σ^ .*

[1] The `nextnano3` software package can be downloaded from www.wsi.tum.de/nextnano3. Support is available through www.nextnano.de.

Immobilization of horseradish peroxidase on oxidized nanocrystalline diamond

Jorge Hernando¹, Tahmineh Pourrostami, Jose A. Garrido, and Martin Stutzmann

The availability of conducting nanocrystalline diamond (NCD) at a relatively low cost with nearly the same exceptional properties as single crystal diamond and the successful immobilization of organic molecules on conducting NCD thin films are attracting a lot of interest in the field of diamond-based biosensors. Previous work [1,2] was based on a time-consuming photochemical process to bind an amine-terminated hydrocarbon chain on a hydrogen-terminated surface. Further progress in this field requires new immobilization alternatives to this photochemical process. We propose the use of oxidized NCD surfaces as the starting point of the functionalization. This implies also a new immobilization chemistry, at least for the linker molecule between the surface and the biomolecules. Besides, due to the fabrication of oxidized structures on the nanometer scale with the help of local anodic oxidation assisted with an atomic force microscope, the functionalization of the oxidized surfaces can take advantage of the design of sensors on the nanoscale, which are characterized by a higher sensitivity and the achievement of denser arrays than conventional micro-sized sensor devices.

Here we present the grafting of aminosilane reagents to oxidized NCD, and the further attachment of horseradish peroxidase (HRP) to the amine-terminated NCD. Our interest in HRP is due to the many different applications of this enzyme, such as the detection of peroxides and the development of immunosensors [3]. In our case, we have started with the development of an amperometric biosensor for hydrogen peroxide.

The aminosilane chosen for the activation of the surface is the (3-aminopropyl)diethoxymethylsilane (APDEMS). The coverage obtained with these molecules is expected to have a thickness of only one monolayer [4]. The achievement of the silanization is analyzed by means of water contact angle and fluorescence microscopy. The contact angle increases from 5 ° after oxidation up to 50 ° after the silanization process. In the case of the fluorescence experiments, a fluorophore such as Rhodamine B isothiocyanate is used in order to enable the reaction between the isothiocyanates and the amino groups on the surface. Figure 1 shows the fluorescence of a periodic pattern of APDEMS-modified 4 μm sized squares, surrounded by H-terminated regions, after the reaction with the fluorophore. A clear pattern can be observed due to the reaction of the fluorescent compound with the amine-terminated squares.

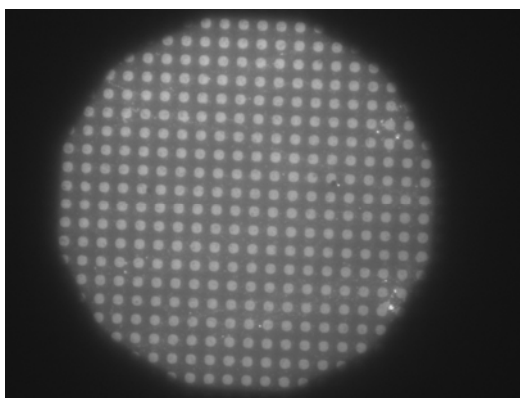


Fig. 1:
Fluorescence of a periodic pattern of APDEMS-modified 4 μm sized squares, surrounded by H-terminated regions, after the reaction with Rhodamine B isothiocyanate.

¹phone: +49-89-289-12765, fax: +49-89-289-12737, email: jorge.hernando@wsi.tum.de

Once the grafting of the APDEMS is under control, the attachment of HRP is accomplished following the procedure of reference 2. The functionalization steps are performed on NCD material with metal contacts, which serve as an electrode for electrochemical measurements. A simple description of the interaction between HRP and H_2O_2 is as follows. HRP can be oxidized by hydrogen peroxide, and then reduced back to the resting state of the native protein. The electrons required for the reduction can be provided by the electrode supporting the proteins (direct electron transfer) or by a mediator (mediated electron transfer). The cathodic current necessary for the reduction of the oxidized state of the protein in the presence of hydrogen peroxide can be correlated with the amount of the peroxide. Figure 2 shows the amperometric response of a HRP/APDEMS-modified NCD electrode on successive addition of H_2O_2 into stirring PBS buffer pH 6.2 at 0 V vs. a Ag/AgCl electrode. The response of an APDEMS-modified electrode is also shown. The larger current observed for the protein-modified electrode is attributed to the direct electron transfer between the protein and the NCD electrode. Further experiments are in progress in order to understand the electronic transfer process between the enzyme and the electrode and to enhance the response with the help of mediators such as ferrocene.

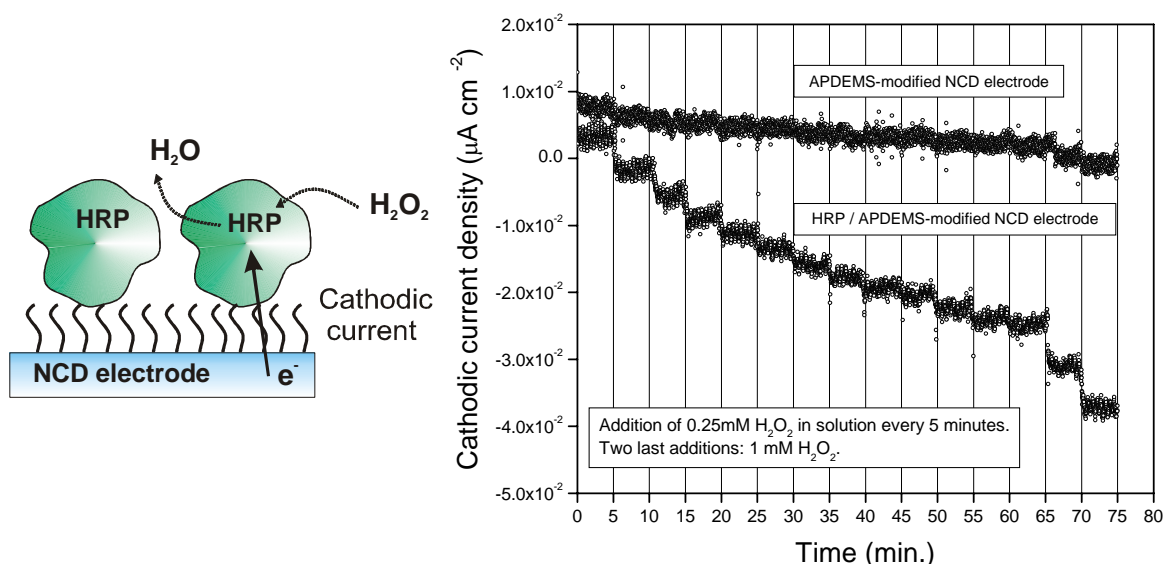


Fig. 2: Amperometric response of a HRP/APDEMS-modified NCD electrode on successive additions of H_2O_2 . The much weaker response of an APDEMS-modified electrode without the peroxidase molecules is also shown for comparison.

- [1] W. Yang, O. Auciello, J. E. Butler, W. Cai, J. A. Carlisle, J. E. Gerbi, D. M. Gruen, T. Knickerbocker, T. L. Lasseter, J. N. Russell, L. M. Smith, and R. J. Hamers, *Nature Materials* **1**, 253 (2002).
- [2] A. Härtl, E. Schmich, A. A. Garrido, J. Hernando, S. C. R. Catharino, S. Walter, P. Feulner, A. Kromka, D. Steinmüller, and M. Stutzmann, *Nature Materials* **3**, 736 (2004).
- [3] T. Ruzgas, E. Csöregi, J. Emnéus, L. Gorton, and G. Marko-Varga, *Anal. Chim. Acta* **330**, 123 (1996).
- [4] J. H. Moon, J. W. Shin, S. Y. Kim, and J. W. Park, *Langmuir* **12**, 4621 (1996).

Jorge Hernando was supported by the Alexander von Humboldt-Stiftung.

Dynamic electrical manipulation of DNA layers on a metal surface

Ulrich Rant¹, Kenji Arinaga^{*}, Gerhard Abstreiter, and Marc Tornow

We report on the dynamic control over the orientation of short oligonucleotide strands which are tethered to gold surfaces in electrolyte solution. By applying alternating electrical bias potentials to the supporting electrodes we are able to induce a switching of the layer conformation between a ‘lying’ and a ‘standing’ state, simultaneously monitored in a contactless mode by fluorescence techniques. We demonstrate that our electro-optical experiments allow for an in-depth investigation of the intriguing molecular dynamics of DNA at surfaces and, moreover, how the dynamic response of these switchable bio-molecule layers opens new prospects in label-free bio-sensing.

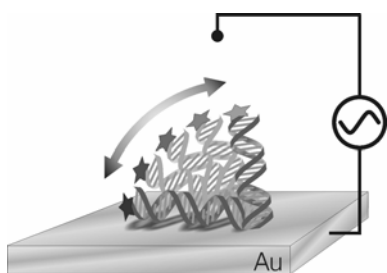
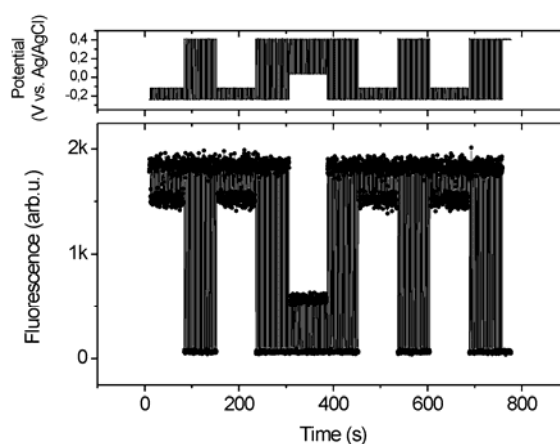


Fig. 1: Schematically depicted switching of a DNA strand which is tethered to a gold surface at one end. Upon reversing the charge on the metallic substrate the negatively charged DNA is either repelled from, or attracted to the surface. The fluorescence emitted from a dye label attached to the DNA is used to probe the distance from its top end to the surface, taking advantage of non-radiative energy transfer to the metal substrate, which quenches the fluorescence gradually as the dye approaches the surface.

Fig. 2: ‘Blinking’ the logo of TUM by electrically controlling the conformation of a layer of double stranded 48mer DNA on a Au surface. Fluorescent light was detected from Cy3 dye labels attached to the distal end of the DNA, the switching frequency was 0.2 Hz. Salt in solution: $[Tris] = 10 \text{ mM}$, surface coverage = $1.7 \times 10^{11} \text{ cm}^{-2}$.



Besides an appropriate choice of electrochemical parameters, considerate tuning of monolayer properties is essential to realize an efficient switching behaviour of the tethered oligonucleotides. Figure 3 shows that the mobility of individual strands is strongly affected by the monolayer packing density. By adjusting the monolayer surface coverage carefully, it is possible to access cooperative layer behaviour as well as to study the dynamics of (an ensemble of) isolated DNA strands.

In order to investigate the dynamic response of the switchable DNA layers, we performed frequency sweeps of the driving AC potentials applied to the supporting Au-electrodes (cf. Fig. 4).

¹phone: +49-89-289-12776, fax: +49-89-3206620, email: rant@wsi.tum.de

^{*}Fujitsu Laboratories Ltd, Japan

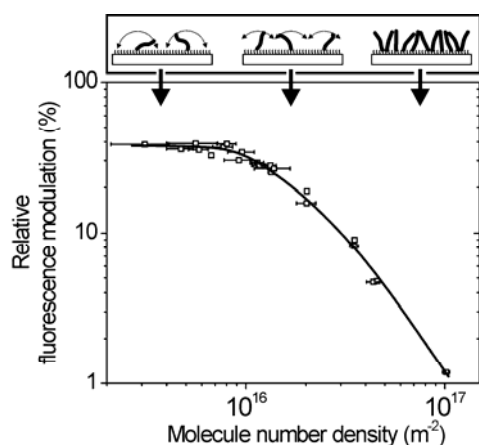


Fig. 3: Influence of the packing density of molecules within layers of 24mer single stranded DNA on the observable fluorescence modulation ($\Delta F/F_{avg}$). The top inset illustrates how steric interactions between adjacent molecules constrain the attainable free gyration of individual strands. The solid line is a guide to the eye; salt in solution: 60mM; $E_{DC}=0.2V$ vs. Ag/AgCl, $E_{AC}=0.2V$, 0.2 Hz square wave.

The appearance of a distinct decline in amplitude in the frequency traces of the DNA switching is intrinsically related to the polarization (-time) of the liquid interface. The alignment of DNA orientations is facilitated by an enhanced electric field in the proximity of the surface that is generated by a thin layer of excess ions which accumulate at the interface from bulk solution. At high frequencies, formation of the ionic layer can not occur, hence electrostatic interactions with the surface are negligible and the DNA's orientation is governed by thermal fluctuations. As a consequence, a manipulation of the layer conformation is not feasible.

Fig. 4: Response of the fluorescence modulation amplitude as a function of the frequency of the driving electrical AC potentials. Upon hybridisation, the double stranded 24mer DNA layer (circles) shows substantially enhanced switching compared to the single stranded conformation (squares), accompanied by a shift of its cut-off frequency to higher values. Monovalent salt in solution: 60 mM; $E_{DC} = 0.2 V$ vs. Ag/AgCl, $E_{AC} = 0.2 V_{rms}$, sine wave. Solid lines are a guide to the eye.

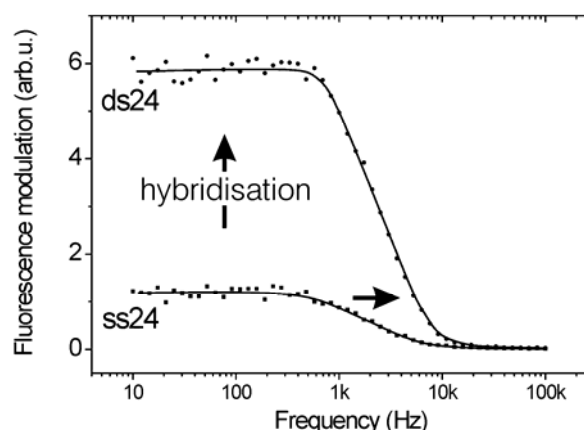


Figure 4 shows a markedly different switching behaviour of single and double stranded DNA, which can be assigned to their dissimilar molecular flexibility. The stiff ds-DNA behaves rod-like, whereas the upper part of the flexible ss-DNA coils on top of the electrically stabilized, surface-near segments. Hence, this suggests the controlled switching of functional polyelectrolyte layers on solid substrates as a novel, label-free, and outstanding method to be employed for bio-sensing purposes. In principle, its applicability is not limited to DNA sensing, but includes all kinds of (bio-) molecules, that, upon specifically binding to the grafted probe layer, would alter its switching dynamics (e.g. by means of the target molecules' charge, size, hydrodynamic properties).

Ref.: U. Rant, K. Arinaga, S. Fujita, N. Yokoyama, G. Abstreiter, M. Tornow, *Langmuir* **20**, 10086 (2004); U. Rant, K. Arinaga, S. Fujita, N. Yokoyama, G. Abstreiter, M. Tornow, *Nano Letters* **4**, 2441 (2004)

Silicon-on-insulator microfluidic device with monolithic sensor integration for μ TAS applications

Sanjiv Sharma, Karin Buchholz¹, Sebastian Luber, Ulrich Rant, Mark Tornow, and Gerhard Abstreiter

Micro Total Analytical Systems (μ TAS) or Lab-on-a-Chip (LOC) are envisaged to unify the preparation and separation of analyte molecules, their monitoring, specific detection and quantification on a single device, preferably with all-electronic in- and output signal processing. Commonly, one of the microfluidic channels functions as the injection unit while the other (perpendicular) one facilitates separation of analytes by electroosmosis and electrophoresis. Within this channel the detection units are integrated. We report on the realization of a novel microfluidic structure concept based on Silicon-on-Insulator (SOI) technology, with monolithic integration of the sensor elements for μ TAS applications. These microstructured sensors are located at the top level of the microfluidic channels in the form of freely suspended silicon bars. Working as surface potential sensitive thin film resistors they are intended to detect bands of charged molecules migrating underneath.

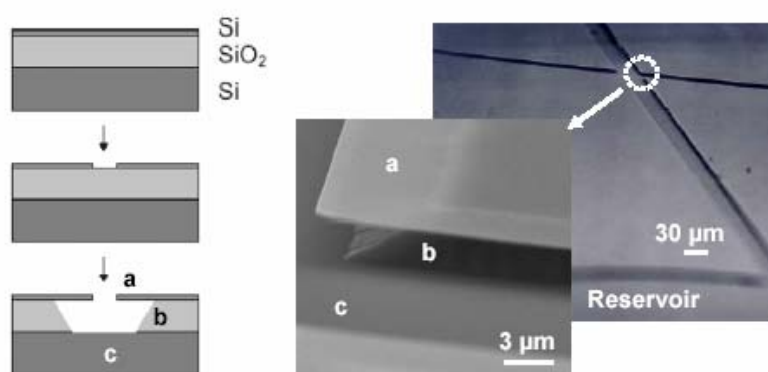


Fig. 1: Left: Basic process steps for channel fabrication from SOI substrates comprising the (a) 205nm thick top Si layer, (b) selectively etched, 3 μ m buried oxide, (c) channel bottom forming Si substrate. Right: Tilted SEM micrograph of a channel cross geometry and close up of the channel intersection region.

We processed devices with a microfluidic cross geometry out of SOI substrates as illustrated in Fig. 1 using a combination of standard photolithographic and etching techniques. At first, the top silicon layer (Boron p-doped, $18 \pm 4 \Omega\text{cm}$) is opened by either wet or dry plasma etching. Subsequently, the buried oxide (BOX) layer is selectively etched in diluted hydrofluoric acid, thereby significantly underetching the top Si layer. The overall device consists of two channels, 5.5mm and 7.5mm in lengths that intersect at right angle and terminate into 1mm diameter reservoirs. The lithographic width of the channels is 30 μ m (55 μ m after underetching) and the channels are 3 μ m deep, as determined by the BOX thickness. After preparation by the etching processes part of the microfabricated structures were passivated by thermally growing 50-200 nm of dry silicon dioxide SiO₂ in order to facilitate electrokinetic experiments. Finally, a 5 mm thick PMMA cover plate having 1 mm diameter access holes (fluid in- and outlets, and electrode insertion) was physically clamped onto the SOI chip sealing the top of the microchannels.

¹ phone : +49-89-289-12776, fax : +49-89-3206620, email: buchholz@wsi.tum.de

To demonstrate the feasibility of fluid manipulation along the channel we performed electroosmotic pumping experiments of a dye-labelled buffer solution (10 mM borate buffer, pH 9.2, rhodamine B)). We recorded electroosmotic flow velocities up to $5\mu\text{m}/\text{sec}$ at an applied voltage of 182 V between two reservoirs.

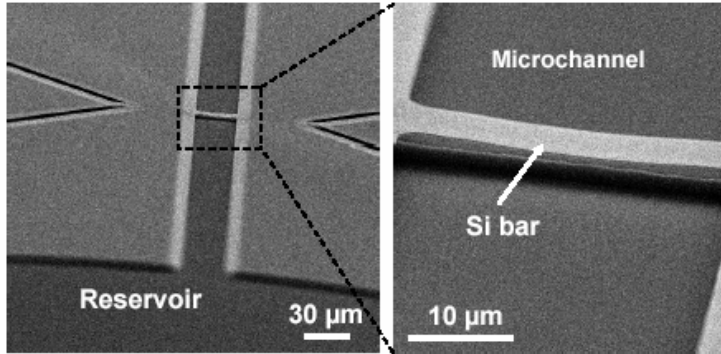


Fig. 2: Tilted SEM micrograph showing a $10\mu\text{m}$ wide, 205nm thick, freely suspended silicon bar crossing a $30\mu\text{m}$ wide microchannel that connects to a reservoir (left), with close-up (right).

Field effect based sensors were monolithically integrated at the channel top level in the form of bridge-like, freely suspended Si bars by sacrificial oxide etching. We characterized the transducing operation of one (unpassivated) Si bar by directly gating it via the electrolyte, recording the I-V characteristic of the sensor device as a function of the reference potential ψ_{ref} .

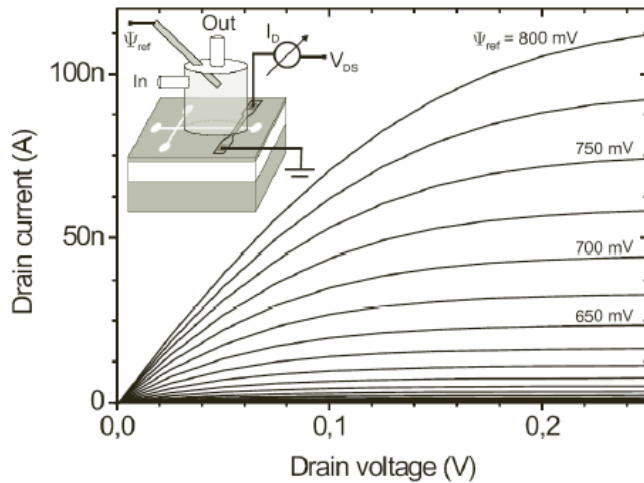


Fig. 3: I-V characteristics of an electrolyte-gated Si-bar that bridges the separation channel. Inset: Schematic sketch of the measurement setup: A test flow chamber exposes the central chip area including the channel at the detection area to a Phosphate Buffered Saline (PBS) solution. The potential of the electrolyte is controlled vs. source by a potentiostat in a standard 3-electrode setup (counter electrode not drawn).

Current-voltage (I-V) characteristics of the Si bar as a function of the electrolyte reference potential are displayed in Fig. 3. In this range of positive reference potential the device is operated as a field effect transistor in the n-channel enhancement mode, i.e., an electron inversion layer is formed within the weakly p-doped Si film close to the Si / SiO₂ interface at all sides of the bar. Below the onset of saturation we estimate a maximal transconductance of $g_m^{\max} = \partial I_D / \partial \psi_{ref} \big|_{V_D=100\text{mV}} \approx 0.36\mu\text{S}$ which for our set-up transforms into smallest detectable surface potential changes of the Si sensor bridge of $\Delta\psi \approx 7.7\text{mV}$.

Quantum-cascade lasers without injector regions

Andrea Friedrich¹, Gerhard Boehm, and Markus-Christian Amann

Quantum-cascade (QC) lasers are quickly becoming the most desirable sources for mid-to far-infrared radiation. Emission-wavelengths between 3 and 160 μm , high output powers in pulsed mode as well as continuous-wave operation above room-temperature (RT) have been demonstrated. In spite of a multiplicity of existing structures, the designs of QC lasers usually share the presence of so called injector regions interleaved with active sections, where the photons are generated. The injector regions allow the relaxation of the electrons into their ground state and ensure their transfer from the lower states of one active section into the upper state of the next section. Due to the doping of these regions, they act as an electron reservoir and provide stable current flow under bias. Apart from these benefits, the main disadvantage of these structures is the lengthening of the active stage with optically passive and slightly absorbing material. Therefore the overlap of the waveguide mode with the active sections is reduced while the optical losses are increased at the same time. Provided that, problems like electron injection can be managed otherwise, QC lasers without injector regions are expected to yield improved performance. Previously, injectorless QC lasers have been realized, but up to now their performances have been low, showing high threshold current densities and a maximum operating temperature of 200 K.

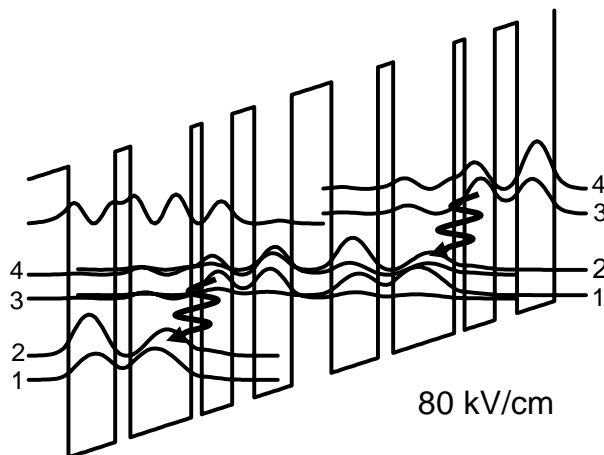


Fig. 1:

Conduction-band profile of two consecutive active sections and moduli squared of the relevant wave functions. The layer thicknesses (in nm) for one active section starting at the left-most barrier are:

3.4/4.0/1.3/5.2/0.9/2.6/1.9/3.2.

The layers in bold are Si-doped to $n=6 \times 10^{16} \text{ cm}^{-3}$.

Recently, we have presented an injectorless QC laser with an improved design, showing low threshold current densities and a maximum operating temperature of 350 K in pulsed mode. In Fig. 1 the conduction-band structure of two successive active sections and the moduli squared of the wave functions of our injectorless QC laser are shown for an applied bias field of 80 kV/cm. The transition energy is calculated to $E_{32}=123 \text{ meV}$ ($\lambda \approx 10 \mu\text{m}$). At a field of 110 kV/cm, where level 1 of one active section is in resonance with level 4 of the following one, $E_{32}=147 \text{ meV}$ ($\lambda \approx 8.4 \mu\text{m}$).

The sample was grown by solid-source molecular beam epitaxy on an n-type InP substrate. The stack of 60 active sections is composed of $\text{Ga}_{0.4}\text{In}_{0.6}\text{As}/\text{Al}_{0.56}\text{In}_{0.44}\text{As}$. The upper cladding consists of a 1.6 μm thick n- $\text{Ga}_{0.47}\text{In}_{0.53}\text{As}$ layer (Si, $6 \times 10^{16} \text{ cm}^{-3}$), followed by a 2 μm thick n-InP (Si, $1 \times 10^{17} \text{ cm}^{-3}$) and a 1 μm thick n⁺- $\text{Ga}_{0.47}\text{In}_{0.53}\text{As}$ (Si, $5 \times 10^{18} \text{ cm}^{-3}$) cap

¹phone: +49-89-289-12767, fax: +49-89-3206620, email: friedrich@wsi.tum.de

layer. A 1.6 μm thick n-Ga_{0.47}In_{0.53}As layer (Si, $6 \times 10^{16} \text{ cm}^{-3}$) and the InP substrate serve as the lower cladding. After growth, ridge-waveguide lasers were fabricated.

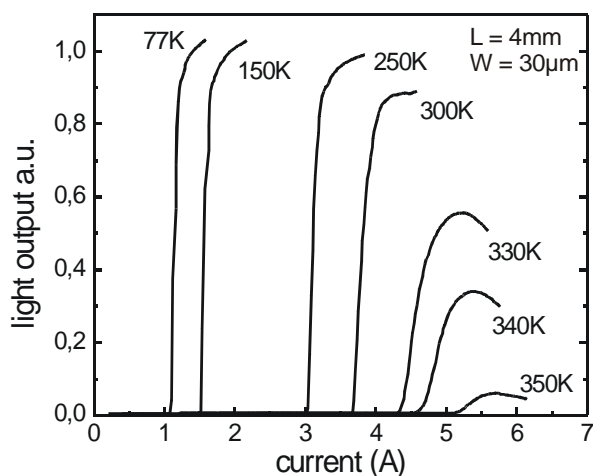


Fig. 2:
Pulsed light output - current characteristics of a 4 mm long and 30 μm wide device at various heat sink temperatures.
Pulsewidth: 250 ns
Repetition rate: 250 Hz

Fig. 2 shows the pulsed light output-current characteristics of a 4 mm long and 30 μm wide representative device for various heat-sink temperatures. The measured values of the threshold current density are 0.9 kA/cm^2 at 77 K, 3.1 kA/cm^2 at 300 K and 4.3 kA/cm^2 at 350 K. The temperature dependence of the threshold current density of a 3 mm long and 30 μm wide laser is shown in Fig. 3. The values for a comparable sample with higher doping in the active regions are also shown. The threshold current densities have been reduced drastically by about 50%.

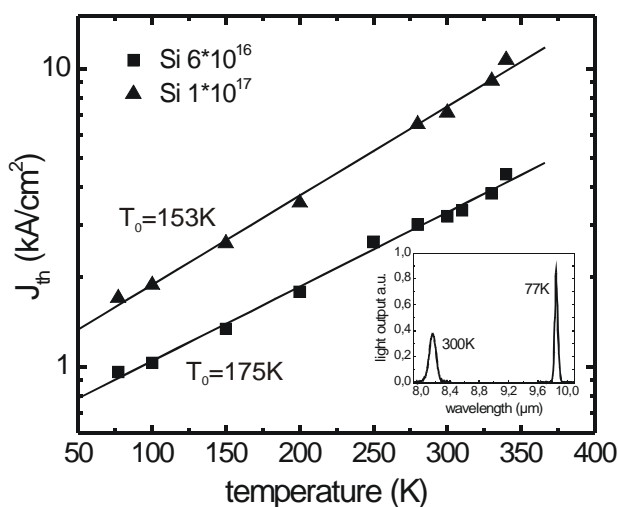


Fig. 3:
Comparison of samples with different active region doping: threshold current density against heat sink temperature.
Inset: Spectra of the low doped sample at 77 K and 300 K.

Compared to former injectorless QC lasers, the threshold current density has been decreased even more ($\sim 70\%$) and the maximum operating temperature has been increased significantly from 200 K to 350 K. The inset of Fig. 3 contains the spectra at 77 K ($\lambda \approx 9.85 \mu\text{m}$) and 300 K ($\lambda \approx 8.16 \mu\text{m}$). A strong shift in the wavelength is observed at higher bias fields and therefore, at high temperatures. This can be explained by a distinctive voltage-induced Stark-effect, according to model calculations.

In conclusion we have demonstrated injectorless QC lasers, for the first time in their performance comparable to conventional QC lasers in the same wavelength region.

ISFETs on single crystalline diamond and their possible applications

Andreas Härtl¹, Jose Garrido, and Martin Stutzmann

A set of exceptional properties makes diamond a particularly suited candidate for bio-sensing. Consisting just of carbon atoms, diamond is known to be per se biocompatible, chemically inert, and it has a large electrochemical potential window and a low background current as an electrode. Covalent attachment of biomolecules like proteins or DNA is possible and seems to be much more stable than on other substrates. In addition, the quasi-two-dimensional conductive layer at the surface of hydrogen terminated diamond offers novel sensing possibilities.

We are investigating Ion-Sensitive Field Effect Transistors (ISFETs) fabricated on CVD grown single crystalline diamond (scd) samples. Conventional ISFETs are based on an insulator (oxide)/semiconductor multilayer system, and their pH sensitivity is attributed to changes of the insulator surface potential which results from ion adsorption/desorption at reactive oxygen surface groups. In the case of the H-terminated diamond surface, the quasi-two dimensional hole accumulation layer at the very surface with conductivities in the order of $10^{-4} \Omega^{-1} \text{ cm}^{-1}$ can be used. As shown before for polycrystalline samples, a perfectly H-terminated surface exhibits nearly no response to a change in the gate voltage and is not sensitive to pH. If, in contrast, the surface is partially oxidized, typical transistor behaviour can be observed. Figure 1 shows typical drain-source current voltage curves for a scd ISFET. Additionally the devices turn pH-sensitive, as can be seen in Figure 2, showing the current, at constant gate and source-drain voltage, versus time while varying the pH. A possible explanation is that a completely hydrogenated surface offers no binding sites for ion adsorption, whereas oxygen sites are known to exhibit amphoteric behaviour: they are capable of becoming protonated or deprotonated, depending on the pH value of the environment.

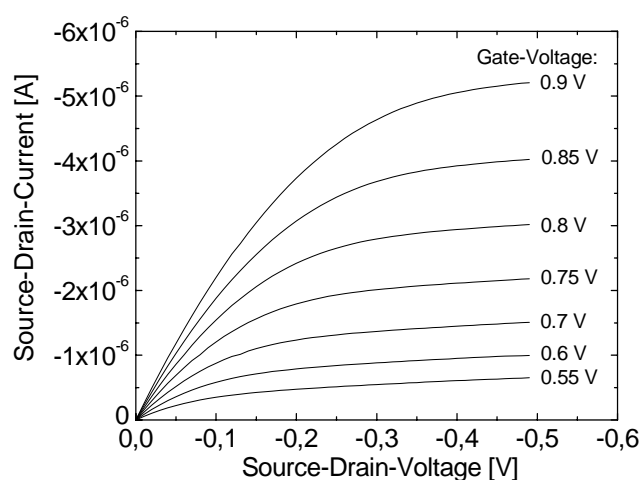


Fig. 1: Transistor characteristics of an ISFET device on single crystalline diamond. The gate voltage is applied via an electrolyte in contact with the diamond surface.

The charges on these active binding sites then can laterally modulate the current under the H-terminated conductive regions. The different performance of samples grown in (100) or (111) crystal orientation (which are expected to have different oxygen surface groups) is currently under investigation, as well as stability and sensitivity enhancement with different oxidation techniques.

Towards the realization of biosensors, a functionalization of the diamond surface with biomolecules has to be established. We have evaluated photochemical surface modifications with different linker molecules to

¹phone: +49-89-289-12768, fax: +49-89-289-12737, email: haertl@wsi.tum.de

which proteins can be attached. Figure 3 shows a simplified flowchart of this procedure. Using nanocrystalline diamond (ncd) films, covalent binding of biomolecules was achieved and concepts of first sensor applications were demonstrated. However, the functionalization of scd appears to be more complicated. Possible reasons are different surface groups in ncd and scd as well as differences in the optical absorption of ncd and scd.

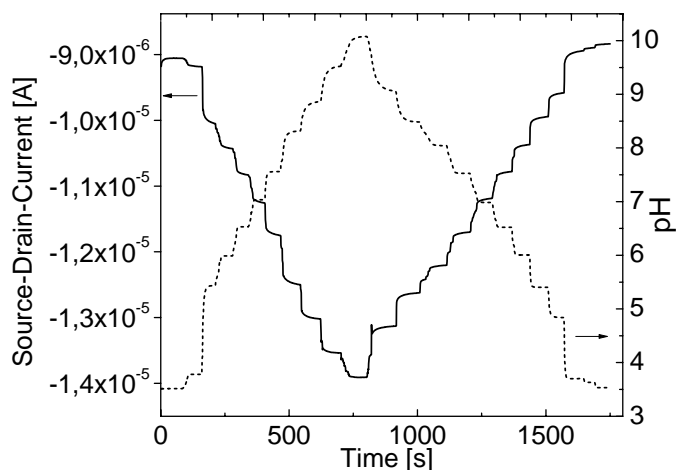


Fig. 2:
SCD ISFET: Source-Drain Current vs. time and variation of the pH.

Future sensor concepts rely on the combination of a stable surface functionalization with biomolecules on the one hand and the exceptional sensing properties of diamond on the other hand. For example, the use of various enzymes which produce local pH-changes after conversion of specific reagents could be possible. With the sensitive detection of these small changes via diamond-based ISFETs various sensor applications in health care and environmental screening are conceivable.

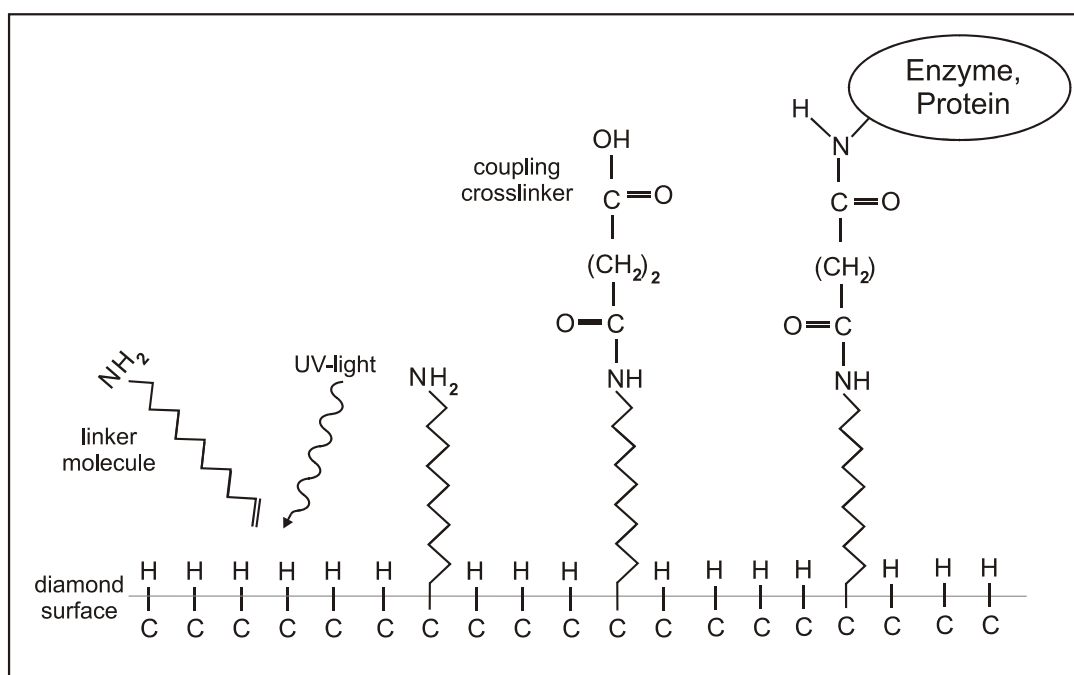


Fig. 3:
Biofunctionalization procedure for H-terminated surfaces: photochemical binding of the linker molecule, coupling of crosslinkers and attachment of biomolecules.

High-speed vertical-cavity laser diodes at 1.55 μm

Werner Hofmann¹, Ning Hua Zhu, Markus Ortsiefer, and Markus-Christian Amann

Vertical cavity surface emitting lasers (VCSELs) feature numerous advantages including single longitudinal mode operation, increased coupling efficiency, reduced power consumption along with low fabrication cost. Furthermore, these devices are particularly qualified for high speed data transmission due to their extremely high intrinsic relaxation oscillation frequencies, low threshold currents and compatible impedance around 50 Ω . Nowadays, 850 nm VCSELs have achieved significant performance as light sources in high-bit-rate data communications. The development of VCSELs in the wavelength ranges around 1.31 and 1.55 μm , however, encountered several technological challenges that have been solved quite recently. GaAs-based approaches using InGaAsN or strained GaAsSb have shown promising results covering the 1.3 μm wavelength range. For 1.55 μm , tunnel-junction VCSELs based on InP show optimal performance. The parasitic capacitance plays an important role with respect to modulation bandwidth. Especially the large capacitances of the n-side contact pads, and space-charge capacitances at the blocking diode around the tunnel-junction have to be taken into account. In order to reduce these parasitics, smaller contact pads and thicker insulation layers were realized. Moreover, to remove the space-charge capacities a dry etching technique was needed that allows the structuring of Indium- and Aluminum-containing semiconductors. Therefore an ECR-process with chlorine was developed, which allows separating the whole VCSEL-structure with vertical sidewalls. Figure 1 shows an SEM-image of an etched sample.

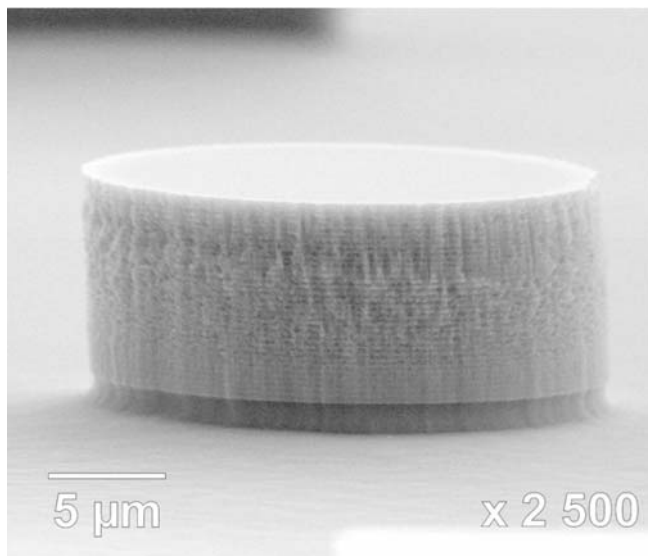


Fig. 1:
InGaAlAs Bragg-mirror etched by electron cyclotron resonance reactive ion etching (ECR-RIE) with Cl_2 .

This technique enables a modified design with an effective reduction in capacitance by replacing the outer parts of the diode by a thick (around 10 μm) insulation layer of BCB (Cyclotene 3022-57). In addition to that the new chip has got two coplanar contact pads in order to enable the direct connection of the VCSEL to a network analyzer using RF-probes. Therefore measurements can be done without the additional influence of parasitic bonding wire inductance.

¹phone: +49-89-289-12786, fax: +49-89-3206620, email: hofmann@wsi.tum.de

From the small signal modulation experiments which are presented in Figure 2 one can deduce a modulation efficiency above $4 \text{ GHz}/(\text{mA})^{1/2}$ and 3dB cut-off frequencies around 8 GHz for reasonable bias currents.

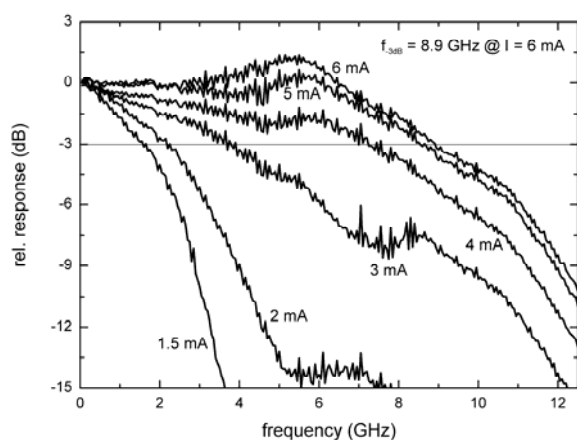
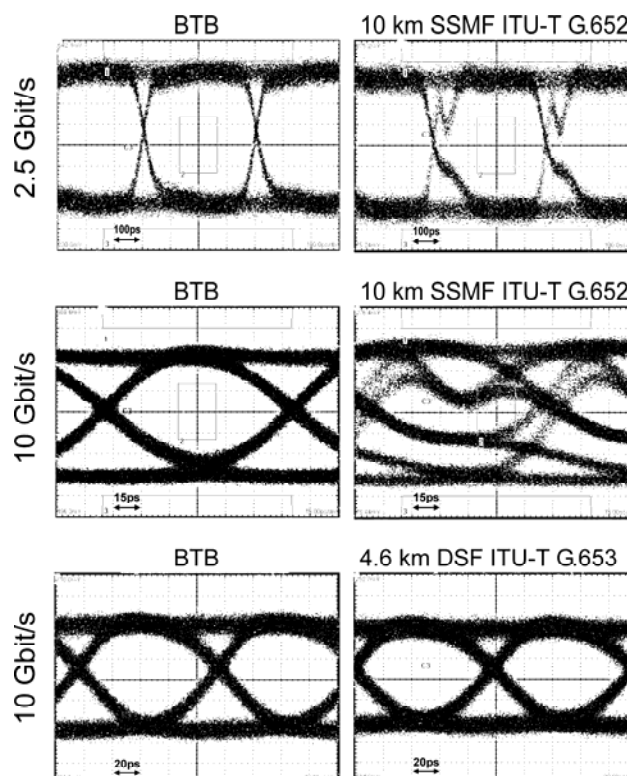


Fig. 2:
Small-signal frequency response of a $3.5 \times 3.5 \mu\text{m}$ VCSEL for various bias currents; $I_{th} = 1.4 \text{ mA}$

Large signal data transmission experiments were done as well. The eye diagrams shown in Figure 3 for back-to-back (BTB) configuration are wide open both for 2.5 Gbit/s and 10 Gbit/s data rates.

Fig. 3:
Eye diagrams recorded with 2.5 Gbit/s and 10 Gbit/s in BTB configuration and data transmission over SSMF and DSF



The oscillation which can be observed in the eye-diagram representing the data transmission over 10 km standard single mode fibre (SSMF) is caused by chirp and the non-

matched dispersion zero at 1.3 μm . As a consequence, the eye closes for 10 Gbit/s data transmission rate. Hence the experiment was repeated using an ITU-T G.653 dispersion shifted fibre (DSF) with its dispersion zero matched to the emission wavelength of 1.55 μm . In this case the eye stayed wide open transmitting data over a distance of more than 4.6 km.

Widely tunable Mach-Zehnder interferometer (VMZ) laser

Thomas Jacke¹, René Todt, Mohamed Rahim, and Markus-Christian Amann

Widely tunable single mode diode lasers in the 1.55 μm wavelength range are key devices in optical data transmission networks, in particular for DWDM-systems. In the presented concept, a Mach-Zehnder interferometer is integrated in the laser resonator and acts as wavelength-selective filtering element. The laser type presented here has the advantage of compactness and simplicity: the wavelength is controlled by one current only and the discrete output spectrum exhibits an appropriate mode spacing for DWDM applications defined by the resonator length.

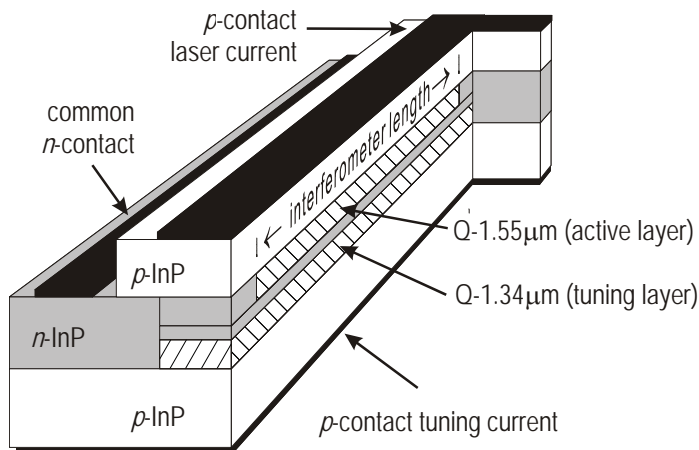


Fig. 1: Schematic view of the VMZ laser

the transmission characteristic of the filter. By injection of carriers into the tuning layer, the phase difference can be varied (plasma effect), and thereby the filter's transmission maxima can be shifted. For an independent control of tuning and laser diode, three independent contacts have to be integrated. The holes are injected transversely by the bottom and top p -contacts, whereas the electrons are injected through the lateral n -InP channel.

The processing of the devices with lateral n -contacts is similar to the tunable twin guide (TTG) laser process. In a first epitaxial step, the InGaAsP double heterostructures are grown by chemical beam epitaxy (CBE). The definition of the mesa and the interferometer is carried out by plasma etching followed by an embedding overgrowth step with n -InP using metal-organic vapor phase epitaxy (MOVPE). Then, the interferometer structure with tapered transitions is etched and regrown with n -InP and, finally, the p -cladding and p -contact layers are grown by CBE. The quality of these interfaces has great impact on the laser performance since bad interface quality can significantly increase the leakage currents. This limits the maximum carrier density in the double heterostructures, and, additionally, the generated heating lowers the refractive index change induced by the plasma effect.

A schematic view of a VMZ laser is shown in Fig. 1. The lateral waveguiding is provided by strong refractive index differences due to the buried heterostructure design. The interferometer is realised by an additional waveguide inserted in the Fabry-Pérot resonator. In the section with two waveguides, two transverse modes are supported. The phase difference of these two modes at the transition to the single-waveguide section determines

¹ phone: +49-89-289-12785, fax: +49-89-3206620, email: jacke@wsi.tum.de

In Fig.2a the emission spectra of a single-VMZ laser is presented without applied tuning current. The Fabry-Pérot resonances can be clearly recognised, the mode spacing is 0.4nm. This mode comb is modulated by the VMZ filter function and the gain curve, which are both effective for the selection of the lasing mode. Since the free spectral range (FSR) of the single-VMZ is smaller than the gain spectrum, filter peaks of different orders are visible in Fig.2a.

During tuning, the periodicity of the filter leads to repeat mode hops in the tuning characteristic, as shown in Fig 2b. From the first repeat mode hop, an FSR of 14nm can be determined for the $L_{VMZ}=688\mu\text{m}$ long VMZ. Within a tuning current range of 20mA, a total filter shift of 19nm towards longer wavelengths can be reached and 80% of the longitudinal resonator modes are accessed. Although the laser current is kept low (50% above threshold), a side-mode suppression ratio SMSR of 14dB is obtained.

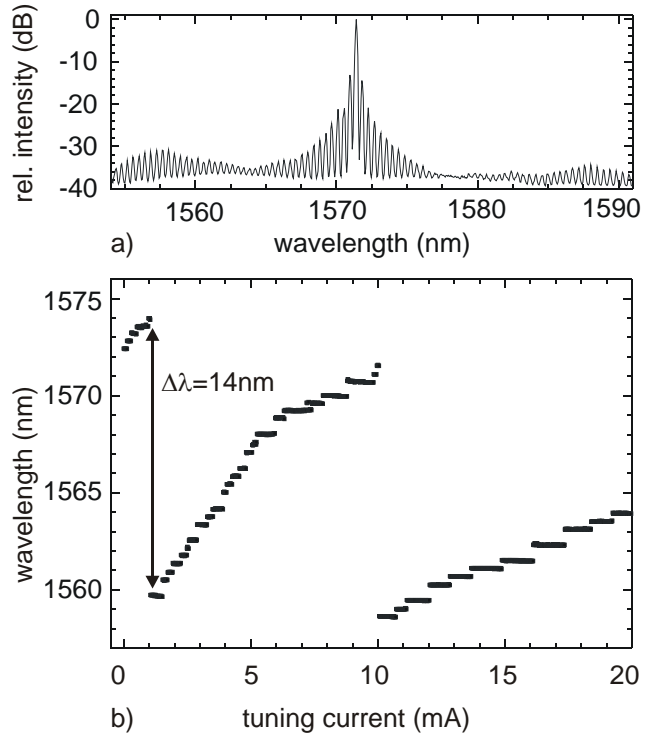


Fig. 2: Tuning characteristics of a single-VMZ laser

In order to extend the FSR, two interferometers of different length are integrated in the resonator of a second laser: The longer

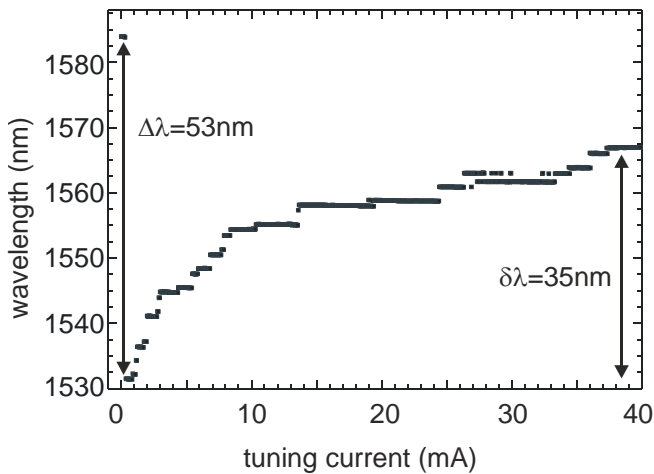


Fig. 3: Tuning scheme of a double-VMZ laser

shown the tuning characteristic of a double-VMZ laser. The FSR of 53nm is in good agreement with the single-VMZ characteristics, since $\text{FSR} \propto 1/L_{VMZ}$. The repeat mode hop occurs already at low tuning currents between the first and second tuning mode. Further on, more than 20 modes can be addressed and a discontinuous tuning range of 35nm is reached.

longer interferometer ($L_{VMZ}=392\mu\text{m}$) enables a high mode selectivity and the short one ($L_{VMZ}=196\mu\text{m}$) with large filter periodicity suppresses the VMZ side maxima of the long interferometer. Both filters shift synchronously when tuned, so that one tuning current is sufficient also for this multi-section device. In the particular configuration employed here, the large filter has double the length of the short filter, subsequently the resulting FSR is that of the short filter. In Fig. 3 is

Novel nonchiral 1D states at corner junctions of two perpendicular quantum Hall systems

Matthew Grayson¹, Lucia Steinke, Michael Huber, Dieter Schuh, Max Bichler, and Gerhard Abstreiter

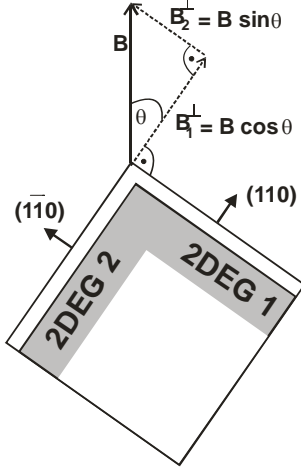


Fig. 1: Schematic of a CQW sample in a tilted magnetic field. The perpendicular fields for both facets are determined by the tilt angle θ .

Previous investigations introduced a high-mobility GaAs/AlGaAs heterostructure bent at an atomically sharp 90° angle, and showed quantum Hall effect on the individual facets. When a quantizing magnetic field is applied to the structure with a tilt angle θ as illustrated in Fig. 1, the system represents a corner junction of two orthogonal quantum Hall systems. Changing the tilt angle allows one to adjust the filling factor ratio $\nu_1/\nu_2 = \tan(\theta) n_1/n_2$, where n_1 and n_2 are the 2D electron densities on the respective facets.

In this work we observe at equal filling factors $\nu_1 = \nu_2$ a finite resistance across the corner connecting the two quantum Hall systems, indicating a conducting 1D channel along the corner. The conductance of this novel 1D system was measured at various filling factors ν , as shown in Fig. 2. For comparison, the longitudinal resistance R_{xx} measured on both facets of the sample is shown in the upper half of Fig. 2. The conductance plots in the lower graph in Fig. 2 are restricted to B -field regions within the quantum Hall minima, where the 1D state is well defined.

At integer filling factors $\nu = 3, 4, 5, 6$ a finite conductance around $1 \mu\text{S}$ is observed, whereas the corner states become insulating at $\nu = 1$ and $\nu = 2$. At the fractional filling factors $\nu = 1/3$ and $\nu = 2/3$, the wire state at the corner be-

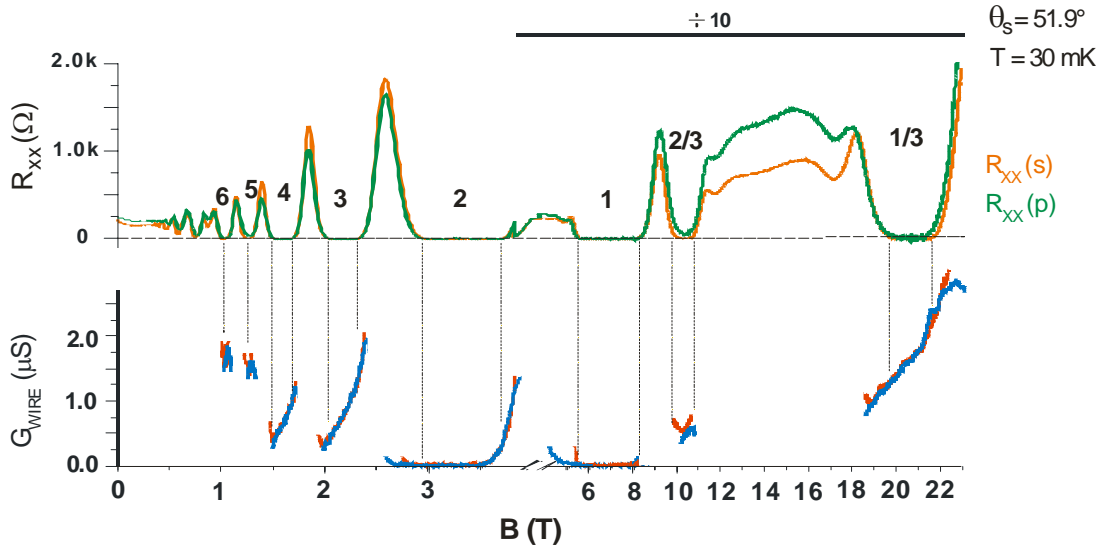


Fig. 2: Conductance measurement of the 1D state at the corner of a CQW sample at various filling factors (below) with R_{xx} -traces added for comparison (above).

¹phone: +49-89-289-12778, fax: +49-89-3206620, email: grayson@wsi.tum.de

comes conducting again, where the conductance of $G \sim 2 \mu\text{S}$ at $\nu = 1/3$ is distinctly larger than at $\nu = 2/3$, where $G \sim 0.5 \mu\text{S}$ is measured.

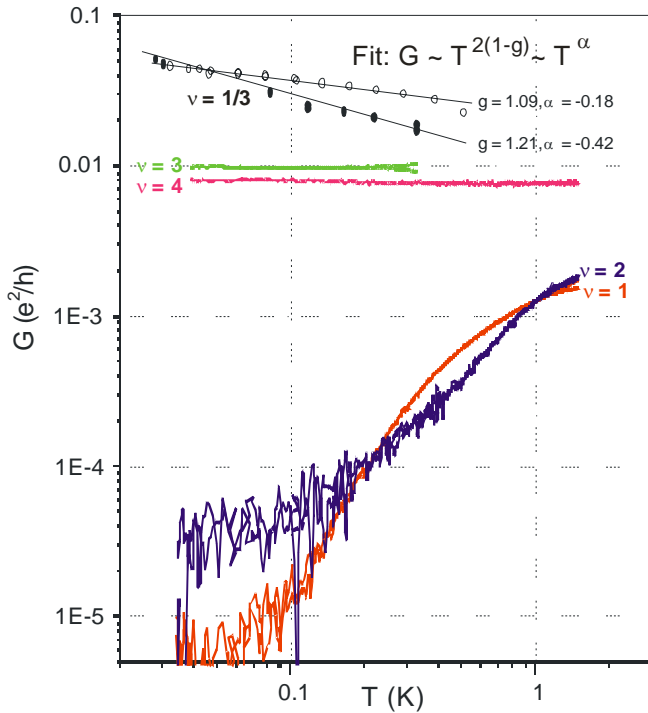


Fig. 3: Temperature dependence of the 1D wire conductance at various filling factors, plotted on a double-log scale.

The temperature dependence of the corner conductance at certain filling factors is shown in Fig. 3 on a double-log scale. The observed conductances range over four orders of magnitude, and show three different behaviors: a 1D insulator at $\nu = 1$ and $\nu = 2$, a 1D metal at $\nu = 3$ and $\nu = 4$ and a 1D disordered superconductor at $\nu = 1/3$.

Spin-unresolved Hartree calculations of the CQW structure showed a charge accumulation along the corner, indicating a bound 1D state (Fig. 4, left). The calculated bandstructure at finite magnetic fields can be interpreted as a hybrid system of two quantum Hall edges and this bound state, as illustrated in Fig. 4 (right), which shows the corner dispersion at $B = 1 \text{ T}$, plotted as energy E vs. cyclotron orbit center, x_c .

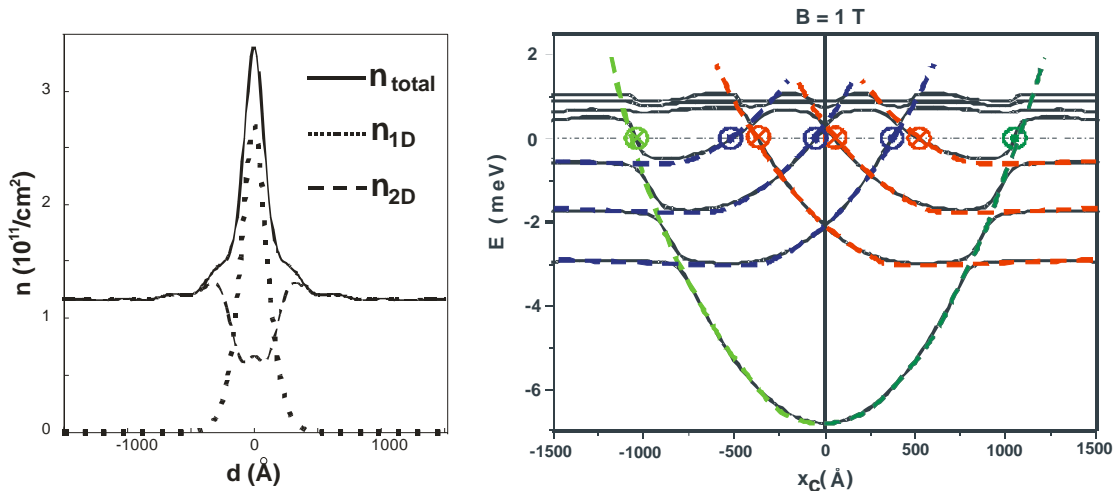


Fig. 4: Hartree charge density distribution for a corner quantum-well device (left). The increased density at the corner ($d = 0$) indicates a bound 1D wire state. The plot on the right shows the calculated bandstructure at $B = 1 \text{ T}$ (black), plotted as Energy E vs. cyclotron orbit center x_c . The additional lines represent the two single quantum Hall edges (blue or red, respectively), and a parabolic dispersion associated with the bound corner state (green).

Photonic crystal nanocavities for solid state quantum optics

Andreas Kress*, Felix Hofbauer, Norbert Reinelt, Max Bichler, Gerhard Böhm, and Jonathan J. Finley

Over the past few years three types of nanostructures have been pursued in the context of solid state based quantum optics experiments using quantum dots: micropillars obtained by etching of monolithic planar microcavities¹, microdisks² and defect resonators in 2D photonic crystals (PCs).^{3,4} Such photonic crystal cavities have particularly strong potential since they offer localized optical modes with high quality factors and low volumes, close to the theoretical limit ($V_{\text{mode}} \sim (\lambda/2n)^3$).

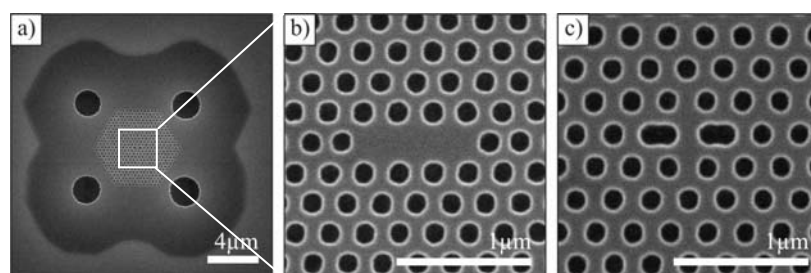


Fig. 1: SEM images of typical PC-cavities investigated. (a) Low spatial resolution overview showing large holes and the region of the free standing GaAs membrane. High resolution images of a L3(b) and Y1(c) PC-cavity designs investigated.

The rapid development of the state of the art PC highlights the swift progress of the field; typical Q-factors have improved from a few hundred to ~ 10000 during the last two years alone. At some level this progress is linked to improved nanofabrication techniques but the major advances are linked to the ability to engineer and tailor the 2D photonic crystal bandstructure leading to a full confinement of the optical field whilst simultaneously suppressing coupling to leaky continuum free space modes surrounding the cavity.

Two cavity designs that have been partly responsible for this significant progress are presented figure 1. Figure 1a is a SEM image of one of our PCs showing an overview of the hexagonal photonic crystal lattice including the large holes to allow the fabrication of free-standing GaAs membranes. Such air-semiconductor-air membranes systems already provide an order of magnitude improvement of the PC-cavity modes. Further advances are based on the novel symmetry breaking cavity designs shown in figure 1b and 1c and fine-tuning the envelope function of

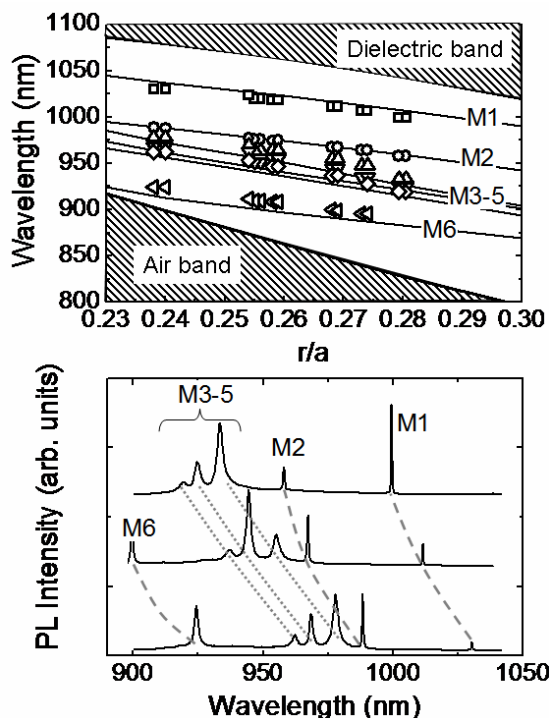


Fig. 2: lower - PL spectra from L3 cavities with different r/a ratios. (upper) Comparison of calculated and experimental mode energies.

*phone: +49-89-289-1278, fax: +49-89-3206620, email: kress@wsi.tum.de

the cavity modes by adjusting the holes immediately surrounding the cavity. The ability to perform this fine-tuning is facilitated by our ability to perform 3D simulations of the photonic modes of our structures. Figure 2 shows typical PL spectra recorded from L3-cavities containing InGaAs quantum dots as a function of the radius r of the air-holes with a fixed period of $a=260\text{nm}$. The upper panel compares the spectral position of the obtained cavity modes with the simulated photonic band-structure. Almost perfect agreement is obtained between calculation and experiment, demonstrating our capabilities to tailor the properties of these photonic devices.

In further work, we have investigated cavity-QED phenomena for small numbers of QD emitters embedded within such PC-defect resonators. In the weak coupling regime, the photon lifetime (τ_{ph}) is determined by the cavity quality factor ($Q=\omega\tau_{\text{ph}}$) but the QD spontaneous radiative decay dynamics can be dramatically modified due to the modified photonic environment, especially close to cavity modes due to the Purcell effect.

Figure 3 shows the spectral dependence of the excitonic decay times for QDs inside (\circ) and outside (\blacksquare) the cavity as a function of detuning from the cavity modes. Both lengthening and shortening of the QD spontaneous emission lifetime is measured relative to their intrinsic values. The lengthening observed is very pronounced (up to 2.5 x) and occurs over a spectral range of $\sim 40\text{nm}$ corresponding to the region of the TE-photonic bandgap. Moreover, on resonance with the cavity modes (solid line fig. 3) the lifetime shortens to $<150\text{ps}$, limited here by our time resolution. By fitting the spectral dependence of the exciton lifetime for QDs located inside the cavity (fig. 3 – inset), we estimate lifetimes as short as $\sim 40\text{ps}$ for QDs spectrally and spatially on-resonances with the cavity modes. Finally, by comparing the dynamics of QDs on- and off-resonance, we measure differences up to a factor ~ 50 suggesting high single mode coupling efficiencies ($\beta\sim 98\%$) for photons emitted into such cavity modes, an essential prerequisite for the realization of efficient single photon sources. Currently our efforts are focussed on single dot experiments and the investigation of quantum correlations in the photon emission statistics and the search for strong light matter coupling with solid state 0D nanostructures.

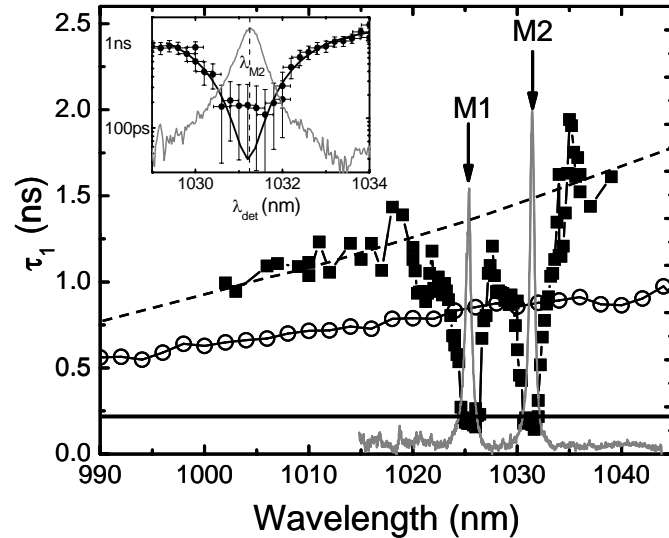


Fig. 3: Spectral dependence of the spontaneous emission decay lifetime for QDs within the photonic crystal (filled squares) and within the unpatterned membrane waveguide (open circles).

Figure 3 shows the spectral dependence of the excitonic decay times for QDs inside (\circ) and outside (\blacksquare) the cavity as a function of detuning from the cavity modes. Both lengthening and shortening of the QD spontaneous emission lifetime is measured relative to their intrinsic values. The lengthening observed is very pronounced (up to 2.5 x) and occurs over a spectral range of $\sim 40\text{nm}$ corresponding to the region of the TE-photonic bandgap. Moreover, on resonance with the cavity modes (solid line fig. 3) the lifetime shortens to $<150\text{ps}$, limited here by our time resolution. By fitting the spectral dependence of the exciton lifetime for QDs located inside the cavity (fig. 3 – inset), we estimate lifetimes as short as $\sim 40\text{ps}$ for QDs spectrally and spatially on-resonances with the cavity modes. Finally, by comparing the dynamics of QDs on- and off-resonance, we measure differences up to a factor ~ 50 suggesting high single mode coupling efficiencies ($\beta\sim 98\%$) for photons emitted into such cavity modes, an essential prerequisite for the realization of efficient single photon sources. Currently our efforts are focussed on single dot experiments and the investigation of quantum correlations in the photon emission statistics and the search for strong light matter coupling with solid state 0D nanostructures.

¹ J-M. Gérard *et al.* Phys. Rev. Lett. **81**, 1110 (1998)

² A. Kiraz *et al.* Appl. Phys. Lett. **78**, 3932 (2001)

³ Y. Akahane *et al.*, Nature, **425**, 944 (2003)

⁴ Y. Yoshie *et al.*, Nature, **432**, 200 (2004)

Calculation of the linewidth broadening in VCSELs and micro-cavities due to temperature fluctuations

Christian Lauer¹ and Markus-Christian Amann

The temperature of a system is classically defined for thermal equilibrium with a heat bath. Nonetheless, a small subsystem, which is in thermodynamical equilibrium with its surroundings, sees fluctuations \mathcal{G} in the local temperature. The variance of these temperature fluctuations in an embedded microsystem of volume V and heat capacity per volume c_V at the classically defined temperature T can be expressed as

$$\langle \mathcal{G}^2 \rangle = \frac{k_B T^2}{c_V V}. \quad (1)$$

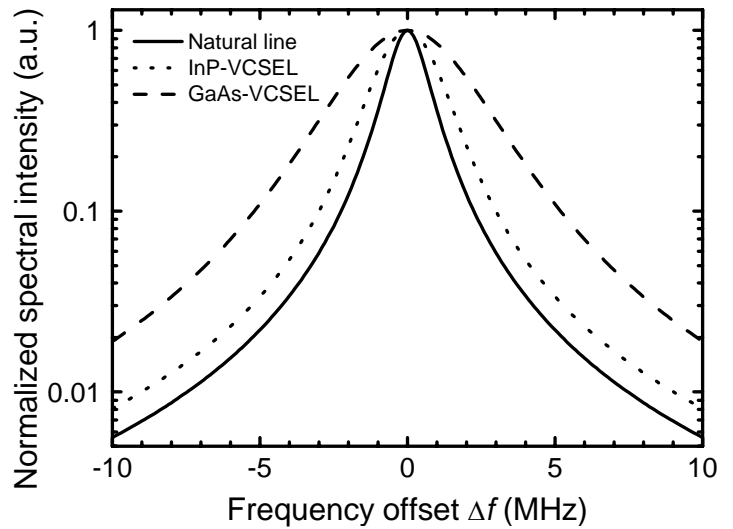
The volume of the relevant microsystem in a laser is the mode volume of the oscillating mode. Vertical-cavity surface-emitting lasers (VCSELs) and micro-cavities, e.g. formed by the tailored waveguiding characteristics of photonic crystals, feature a very small active volume and a small radial extension of the optical mode profile. The small volume implies strong temperature fluctuations in these microsystems, resulting in phase noise and a broadening of the emission line via the temperature dependent index of refraction (thermorefractive effect). The time-dependent phase autocorrelation function ideally only depends on the natural linewidth $\Delta\nu_0$ of the laser, $\langle \Delta\Phi^2(t) \rangle = 2\pi\Delta\nu_0 t$. Now it is augmented by an additional sum term due to the temperature fluctuations,

$$\langle \Delta\Phi_h^2(t) \rangle = \left(\frac{d\omega}{dT} \right)^2 \int_0^t d\tau \int_0^t d\tau' \int d\vec{r} \int d\vec{r}' |E(\vec{r})|^2 |E(\vec{r}')|^2 \langle \mathcal{G}(\vec{r}, \tau) \cdot \mathcal{G}(\vec{r}', \tau') \rangle,$$

with the circular resonance frequency ω , the autocorrelation function of the temperature fluctuations, and the optical intensity profile $|E|^2$. The radial profile of the latter is assumed to be Gaussian with a full width at half maximum (FWHM) of D , equal to the radial mode diameter. To find a solution, we apply the temperature diffusion equation using the appropriate Langevin force with the autocorrelation function

$$\langle F(\vec{r}, t) F(\vec{r}', t') \rangle = \frac{2D_T k_B T^2}{c_V} \nabla_{\vec{r}} \cdot \nabla_{\vec{r}'} \delta^3(\vec{r} - \vec{r}') \delta(t - t').$$

Fig. 1:
Natural Lorentzian line (solid) with a FWHM of 1.5MHz and the corresponding Voigt lines after thermal broadening to 4.4MHz in an InP-VCSEL (dotted) and 2.4MHz in a GaAs-VCSEL (dashed). The mode diameter was assumed to be $6\mu\text{m}$.



¹phone: +49-89-289-12788, fax: +49-89-3206620, email: lauer@wsi.tum.de

We assume a heatsink with constant temperature T at $z = -d_1$ and thermal isolation at $z = d_2$, develop \mathcal{G} into radial and longitudinal modes (wave vectors \vec{k}_i), and apply the Hankel transform mechanism to get

$$\langle \Delta \Phi_{th}^2(t) \rangle = \frac{1}{\chi} \left(\frac{d\omega}{dT} \right)^2 \sum_i S_i(D, L, T, t),$$

with thermal conductivity χ and cavity length $L = d_1 + d_2$. The sum terms S_i are decreasing rapidly with increasing i , only a few have to be taken into account for sufficient accuracy. Finally, a Fourier transform of this phase autocorrelation function yields the emission spectrum and the linewidth (Wiener-Khinchine theorem). The natural term in the total phase autocorrelation function is proportional to time t . The thermal term turns out to be proportional to t^2 , resulting in a spectral Voigt profile. The line broadening strongly increases with decreasing natural linewidth and decreasing mode volume or diameter.

We carried out numerical calculations of the line broadening in GaAs-based and InP-based VCSELs at 850nm and 1550nm, respectively. Practical GaAs-devices feature two epitaxial distributed Bragg reflectors, their InP-based counterparts exchange one of them for a thinner dielectric mirror. This difference was accounted for in the mode volume. In addition, the change of frequency with temperature is more pronounced in GaAs-devices due to the shorter emission wavelength.

Models treating other broadening mechanisms like carrier fluctuations derive natural linewidths of 1-2MHz for a diameter of 6 μ m. Thermal fluctuations transform this Lorentzian line into a significantly broadened Voigt line. Fig. 1 displays the natural line of a mode with a FWHM linewidth of 1.5MHz along with the corresponding thermally broadened lines with FWHMs of 4.4MHz and 2.4MHz for typical parameters of GaAs-based and InP-based VCSELs, respectively.

Fig. 2 shows the line broadening $\Delta v - \Delta v_0$ vs. the natural linewidth Δv_0 for several mode diameters D . The broadening grows stronger for smaller mode volumes, therefore the effect is expected to grow dominant in small devices, like photonic crystal VCSELs or microcavities for the exploitation of the Purcell effect to direct the spontaneous emission.

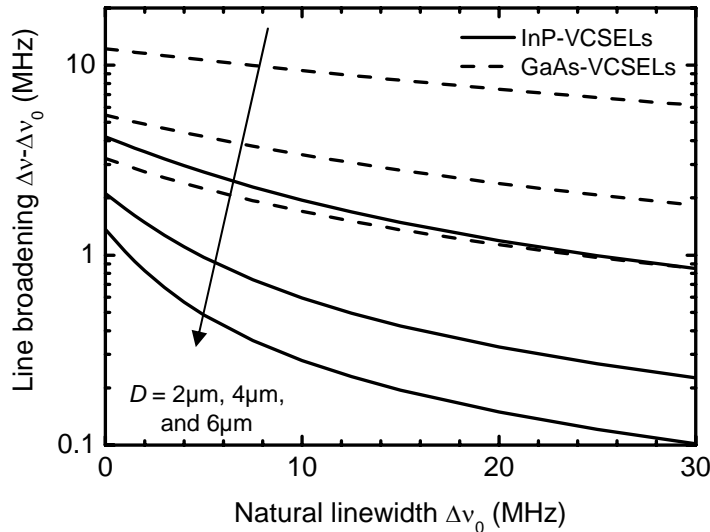


Fig. 2: FWHM line broadening $\Delta v - \Delta v_0$ due to thermal fluctuations calculated for GaAs- and InP-VCSELs for several mode diameters D and an ambient temperature of 300K.

Micro-mechanically tunable long wavelength VCSEL

Markus Maute¹, F. Riemenschneider², Gerhard Böhm, P. Meissner², and Markus-Christian Amann

Widely tunable long-wavelength vertical-cavity surface-emitting lasers (VCSELs) are highly attractive light sources for telecom applications within Dense-Wavelength-Division-Multiplexing (DWDM) systems. Fixed wavelength laser replacement, single transverse-mode operation with high side mode suppression, and high coupling efficiency into an optical fiber are some of the main benefits of those devices. Various monolithic concepts of micro-electro-mechanically tunable VCSELs have been presented to date. Here, we investigate a new approach based on a two-chip concept that allows for a separate optimization of the components. The device (see Fig. 1) consists of a “half-VCSEL” and a movable top mirror membrane.

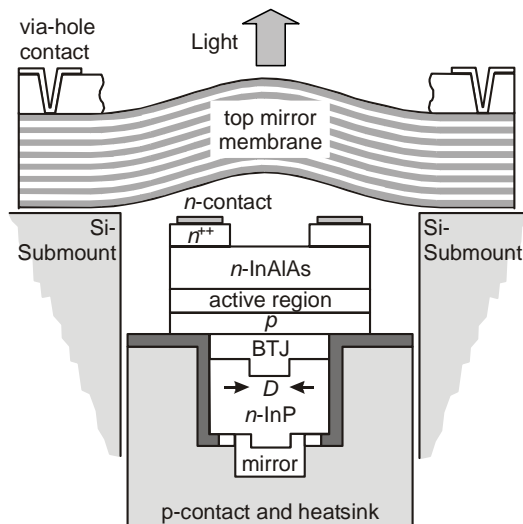


Fig. 1:
Schematic cross section of a tunable two-chip VCSEL.

The current confinement in this structure is realized by the use of a buried tunnel junction (BTJ) of a given diameter D and the back reflector is formed by a dielectric mirror. Since the membrane is much bigger in size compared to the half VCSEL a silicon-submount is used. The micro-mechanically tunable mirror is an MBE-grown $(\text{In}_{0.05})\text{GaAs}/\text{AlGaAs}$ -Bragg-mirror of about 24.5 periods leading to a very high theoretical reflectivity of 99.95%. After defining the shape of the membrane and partial removal of the semi-insulating GaAs substrate the additional 5% indium content in some of the GaAs-layers leads to a stress-gradient and therefore to a rotation-symmetric concave curvature with a radius of about 2mm. Due to this curvature the necessary assembling step of the mirror in respect to the active part is rather insensitive to tilt and the variable air-gap of approximately $6\mu\text{m}$ is formed without the need for additional spacing elements. Deflection of the membrane, i.e. wavelength tuning, can be achieved by electro-thermal heating of the thin suspension beams by injecting a small current using the via-hole contacts through the substrate (see Fig. 1).

A continuous wave spectrum for a VCSEL with $D = 20\mu\text{m}$ is shown in Fig. 2, indicating single-mode operation at room temperature. When the wavelength is tuned, the power

¹phone: +49-89-289-12786, fax: +49-89-3206620, email: maute@wsi.tum.de

²Institute of Microwave Engineering, Darmstadt University of Technology, 64283 Darmstadt

of the laser peak is given by the envelope trace in Fig. 2. As can be seen, a record-breaking tuning range of more than 40nm was accomplished. The maximum output power was found to be around $100\mu\text{W}$. Such a low value can be attributed to the use of a very high reflecting top mirror. By reducing the number of mirror pairs to 16.5 a maximum fiber coupled power for a similar device with $D = 10\mu\text{m}$ of more than 1mW was already observed.

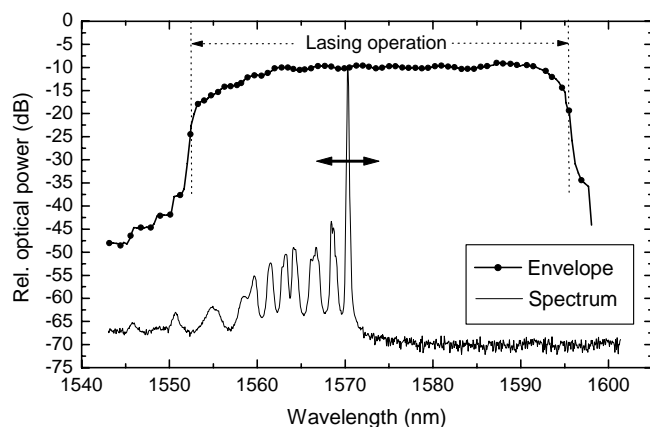


Fig. 2:
Typical laser spectrum. The envelope shows the maximum output power during tuning. The spectrum is single mode over more than 40nm.

To determine the tuning speed, the step response was recorded by modulating the tuning current with a rectangular signal of sufficient low frequency. The temporal wavelength shift of the VCSEL has been measured using an optical Fabry-Pérot filter with a periodic transmission characteristic followed by a receiver connected to an oscilloscope. The moving laser peak scans the well-known filter characteristic which is temporarily visualized on the oscilloscope. Two different amplitudes have been investigated leading to a wavelength jump of 8 and 29nm (Fig. 3). The membrane shows a typical first-order exponential behavior with a $1/e$ -time constant of around 1ms. This value is almost identical for both wavelength shifts and for a rising as well as for a falling edge of the tuning current step.

In conclusion, we have shown a tunable VCSEL based on a two-chip approach with a very wide tuning range and good side mode suppression. Further research is dedicated to the output power and first promising results on the order of 1mW indicate the high potential of this kind of devices.

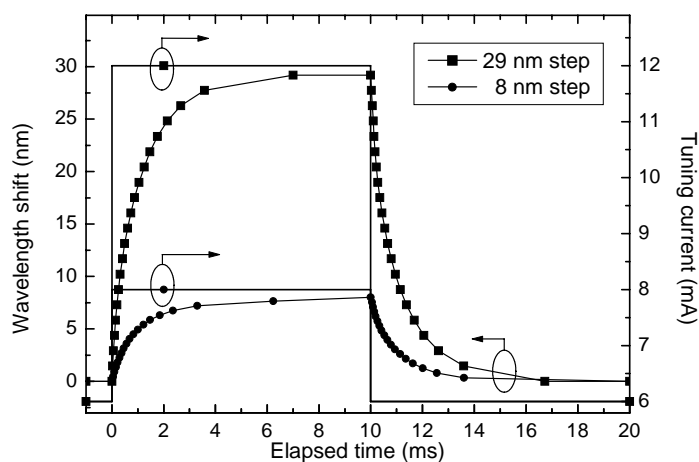


Fig. 3:
Step response of the VCSEL showing the temporal behavior of the laser wavelength as the tuning current is changed rapidly from 6 to 8mA and from 6 to 12mA, respectively.

Towards a new quantum wire structure realizable by double cleaved-edge overgrowth: Characterizing the transfer potential

Sebastian Roth, Matthew Grayson, Max Bichler, Dieter Schuh, and Gerhard Abstreiter

The cleaved-edge overgrowth method makes it possible to fabricate very clean single cleave quantum wires in the GaAs/AlGaAs material system, having atomically precise control over the structural design. An MBE grown heterostructure supplying a potential structure close to a narrow low-dimensional electron gas can modulate the carrier density in the system, because the electron wave function tail is pinched by a high barrier potential. A new approach to fabricate quantum wires next to a transfer potential is double cleaved-edge overgrowth. However, also the barrier material can influence the electron density, independent of the barrier potential. We present basic research on double cleave structures investigating a wide 2DEG, whose density is modulated not from quantum confinement but from the alloy content of a neighboring substrate. We propose that the density difference arises from charged defects in the AlGaAs layer.

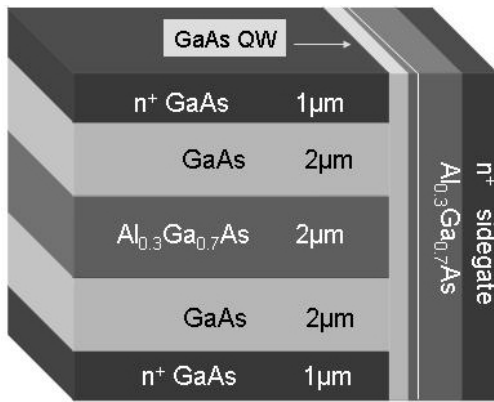


Fig. 1: Sample after 1st CEO

Fig.1 shows the sample structure. First a substrate is grown in [001]-direction, whose layer sequence is sandwiched by two 1 μm thick n^+ -contacts. The sequence consists of two 2 μm thick GaAs layers surrounding an $\text{Al}_x\text{Ga}_{1-x}\text{As}$ layer with an Al-content of $x=0.3$. After cleaving the sample in-situ, a 40nm GaAs quantum well is grown in [110]-direction separated from a n^+ -sidegate by a 0.55 μm thick $\text{Al}_x\text{Ga}_{1-x}\text{As}$ barrier, which contains a Si modulation doping at a distance of 50nm from the quantum well, to supply electrons. A 2DEG develops in the quantum well and the density of it can be tuned by the

sidegate. The sample is completed with a second cleaved-edge overgrowth in the $[1\bar{1}0]$ -direction, which in future devices is necessary to further reduce the dimension of the electron system, however, it plays no active role at the gate bias range used in this work. We characterize all samples by measuring the Shubnikov de Haas (SdH) oscillations of the quantum well 2DEG varying temperature, gate voltage and illumination conditions.

Typical results of the SdH-measurements are shown in Fig.2. Because the samples used are about 3mm wide, but the distance between the n^+ -layers contacting the wide quantum well 2DEG is only 6 μm, the magnetoresistance has different boundary conditions than in commonly used Hall bar samples. The result is reminiscent of a Corbino geometry, with a ring shaped 2DEG with inner and outer contacts, where the quantum Hall states induce maxima rather than minima. In samples of finite width, however, the resistance at integer filling factors takes a peak value of $R_{2\text{pt}} = R_{xy} = h/e^2 i$, for i filled, spin resolved Landau levels. Due to leakage effects the measured $R_{2\text{pt}}$ in Fig.2 is smaller than the quantized value. Two series of peaks, equally spaced in $1/B$, where B is the magnetic field, can be identified in Fig.2. This observation indicates two densities, differing by a value of Δn . Biasing the sidegate positive, shifts the peak structure towards higher magnetic fields as

¹ phone: +49-89-289-12736, fax: +49-89-3206620, email: roth@wsi.tum.de

the densities of the electron systems increase. Fig.3 shows the dependence of the densities with gate voltage and the value of Δn . The slope of the data points can be compared to the slope of the simple capacitive relation:

$$dn/dV_G = \epsilon_0 \epsilon_r / ed$$

where d is the distance between the capacitor plates. The good agreement for $d = 0.55 \mu\text{m}$, the expected growth value, demonstrates that both 2DEG systems are indeed located in the quantum well.

The existence of a high and a low-density 2DEG is at first expected, because of the stronger quantum confinement next to the $\text{Al}_x\text{Ga}_{1-x}\text{As}$ barrier. However, simulations show that the ground-state energies in a 40 nm wide quantum well and an infinitely wide well are identical,

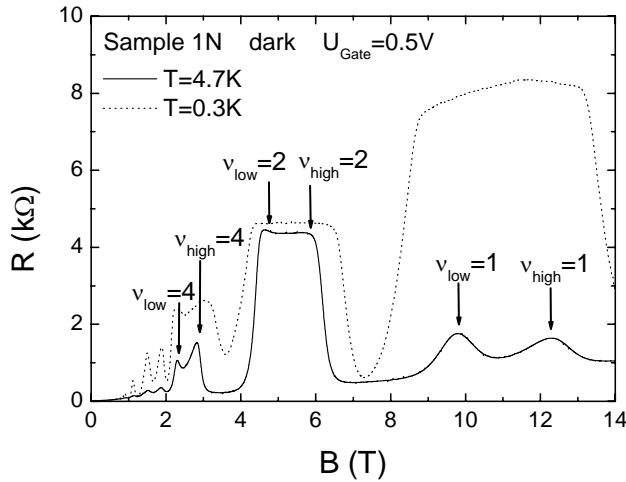


Fig. 2: SdH-measurements of a sample with a 40nm wide quantum well

implying the densities should actually be the same. The result was also observed in the Ph.D. thesis of R. A. Deutschmann (WSI - 2001) for wells of the same thickness, where the wavefunction in the triangular potential drops to zero before reaching the barrier. The remaining possibility is that charge storage from defects in the materials of the GaAs/AlGaAs heterostructure of the adjacent substrate is itself responsible for the effect.

Illumination of the sample with an IR-LED affects the two systems unequally and brings forth a change of the density difference Δn . Furthermore both densities *decrease* with illumination. Hence an argument that the light simply activates the Si-donors of the

modulation doping is not consistent. A possible explanation is provided by an earlier experiment on quantum wells surrounded by $\text{Al}_x\text{Ga}_{1-x}\text{As}$ barriers. Here the density of a 2DEG after illumination depended strongly on the Al-content of the back barrier. Because the growth of $\text{Al}_x\text{Ga}_{1-x}\text{As}$ produces more defects with higher Al content x , more charges can be trapped in these layers. Illumination can rearrange the charges in these traps resulting in a persistent photo-conductivity effect. Accordingly the low-density 2DEG in our samples is related to the underlying AlGaAs substrate layer. This new effect will cause density modulations in addition to any wavefunction confinement effects.

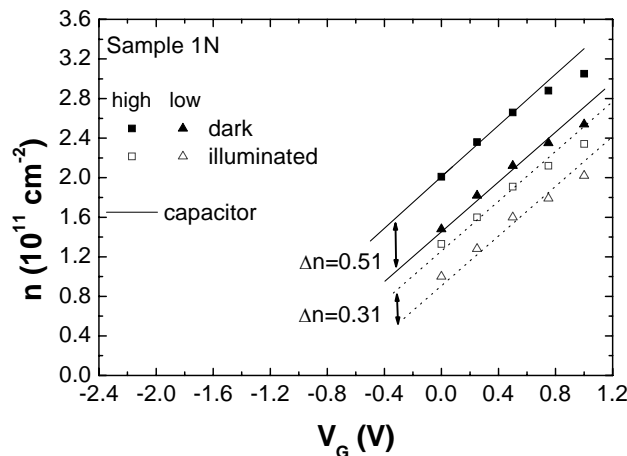


Fig. 3: Densities of the 2DEGs depending on gate voltage and illumination condition

Novel tunable twin-guide laser diodes for wide wavelength tuning at 1.55 μm

René Todt¹, Thomas Jacke, Ralf Meyer, and Markus-Christian Amann

Widely tunable laser diodes with a tuning range of several tens of nanometers are being regarded as key components for future fiber optical communication networks and are highly attractive light sources for gas sensing applications as well as for fiber Bragg grating (FBG) based sensor devices.

Although the first widely tunable lasers have already been presented about a decade ago, even today practically all available devices suffer from several serious drawbacks. For example device characterization is a very common issue: since typically three or even more tuning currents are required to adjust the emission wavelength, the device calibration that is required for every single laser diode becomes time-consuming and, therefore, also expensive. Further drawbacks include limited output power, limited direct modulation capabilities and fabrication complexity.

Recently, the so-called widely tunable twin-guide laser with sampled gratings (SG-TTG) has been suggested in order to overcome many of the aforementioned issues. The

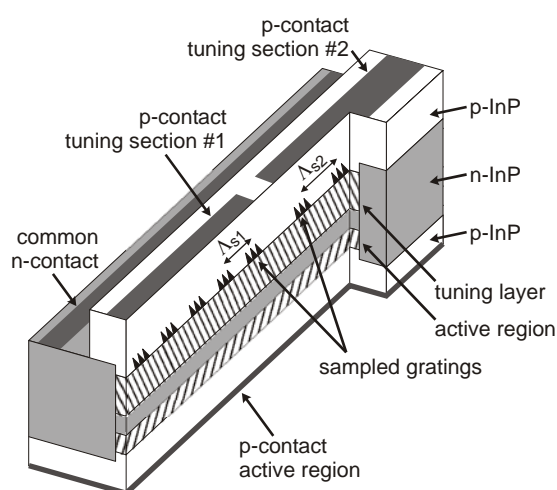


Fig. 1: Schematic of a widely tunable twin-guide laser diode with sampled gratings.

main advantage of this novel device structure is its DFB-like behavior. Due to the vertical integration of active and tuning sections (Fig. 1), a phase tuning section, which is usually required to adjust the cavity mode position in longitudinally integrated devices, is needless. Hence, the SG-TTG laser requires at least one tuning current less than comparable devices. This facilitates efficient characterization.

In a widely tunable TTG laser, as schematically depicted in Fig. 1, the tuning region is split into two parts that contain sampled gratings of different sampling periods ($\Lambda_{S1} \neq \Lambda_{S2}$). Therefore, each tuning section provides a comb-like reflection spectrum of different peak spacing and, thus, Vernier-effect tuning

can be employed to achieve wide wavelength tunability.

The first fabricated devices clearly confirmed the device principle of the SG-TTG laser diode: a tuning range of 28 nm and high side-mode suppression ratio was achieved with only two tuning currents. However, the tuning behavior was observed to be fairly irregular. Although single-mode operation was regularly obtained, supermode changes took frequently place without any systematic pattern and many supermodes were missing. Emission spectra of several supermodes of an SG-TTG laser diode, illustrating the wide tuning range of the device are shown in Fig. 2. Even though one supermode was expected around 1557 nm, it was missing and lasing could not be achieved at this specific wavelength.

¹phone: +49-89-289-12767, fax: +49-89-3206620, email: todt@wsi.tum.de

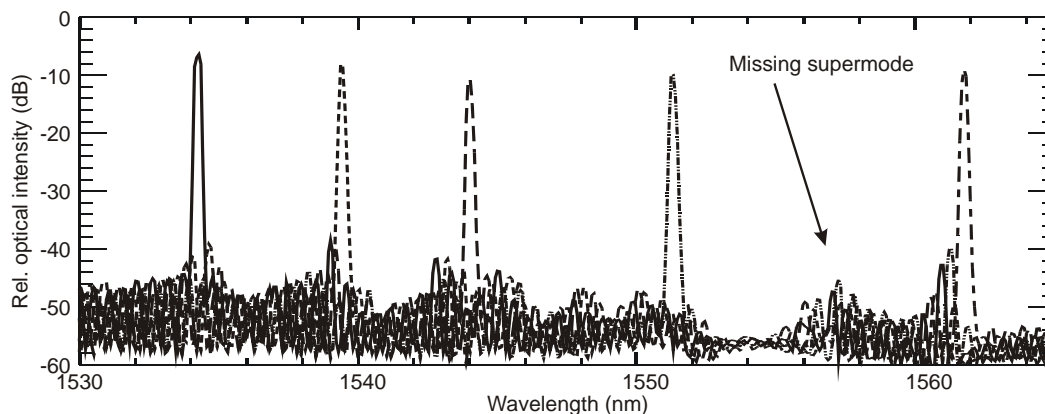


Fig. 2: Spectra showing supermodes of an SG-TTG laser. One supermode to be located at ~ 1557 nm is missing and only strong electroluminescence is observed at this wavelength.

Irregular tuning behavior as well as missing supermodes, causing gaps in the tuning range, are unacceptable and were subject of further investigations. It turned out that a facet reflectivity of below 0.1%, preferably around 0.01%, is required to obtain a regular tuning behavior. However, achieving such a low facet reflectivity over a wide wavelength range of several tens of nanometers is not a trivial task.

This can e.g. be accomplished by terminating the buried waveguide several ten micrometers before the AR-coated facet. These so-called window structures have been implemented in test structures. Comparing the amplified spontaneous emission spectrum of a sampled grating with and without window structures demonstrates the strong influence of the facet reflections. While missing and splitted peaks are observed from the device with as-cleaved facets and AR-coatings, which would lead to missing supermodes and tuning irregularities in an SG-TTG laser, a very uniform emission spectrum is obtained from the device that features window structures. Hence, a regular tuning behavior is expected from future generations of widely tunable twin-guide lasers that will employ these window structures.

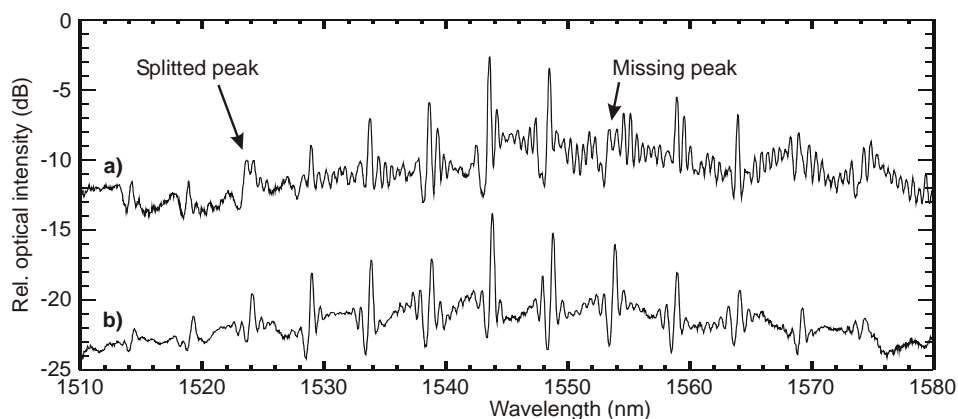


Fig. 3: Amplified spontaneous emission (ASE) spectra of a sampled grating with as-cleaved facets & AR-coatings (a) and with window structures & AR-coatings (b). A very uniform emission spectrum is obtained through the use of window structures in combination with AR-coating.

3. Research Funding and Collaborations

Many of our research projects have benefited from very fruitful collaborations with external groups either via joint projects, individual collaborations, exchange programs, or through direct interaction with visitors. The major external collaborations are based on joint projects which are financially supported by different organizations.

Funded Projects

1. Bundesministerium für Bildung und Forschung (BMBF)

- Kompetenzzentrum Nanoclub Lateral: „Selbstorganisiertes Wachstum auf Si“ (SOWASI, partner: DaimlerChrysler Ulm)
- Kompetenzzentrum Nanop: „Anwendung von Nanostrukturen in der Optoelektronik“
- Kristalline Silizium-Legierungen für Dünnschicht-Solarzellen
- Förderschwerpunkt Elektronenkorrelation und Dissipationsprozesse in Halbleiter-quantenstrukturen: „Vertikale Ultrakurzkanal- und Tunneltransistoren“, „Deterministische Ladungsquelle“
- Förderschwerpunkt MultiTeraNet; „Mikromechanisch abstimmbare VCSEL für den Wellenlängenbereich 1,5 μm “
- Förderschwerpunkt neue Materialien; „Materialien für Infrarotkonverter“
- „Netzwerk „Erneuerbare Energien“: „Photon-Management und Bandstruktur-Design für effizientere Solarzellen“
- „Halbleiter-Nanostrukturen für molekulare Bioelektronik“
- „EXIST-SEED; nextnano³ – Entwicklung von Simulationssoftware“

2. Deutsche Forschungsgemeinschaft (DFG)

- Sonderforschungsbereich „Bioorganische Funktionssysteme auf Festkörpern“ (SFB 563)
- Sonderforschungsbereich „Festkörperbasierte Quanteninformationsverarbeitung“ (SFB 631)
- Schwerpunktprogramm „Quanten-Hall-Systeme“
- Schwerpunktprogramm „Optische Übermittlungsverfahren in der Informationstechnik“
- Forschungsk Kooperation „FORMEDIAN“
- Am 101/6-1: „Transversal integrierte abstimmbare Laserdioden“
- Ei 518/1-1: „Heteroepitaxie von Gruppe III-Nitriden auf Diamantsubstraten für optoelektronische und elektronische Anwendungen“

3. Bayerische Forschungsstiftung

- Langfristprogramm Neue Werkstoffe
- ForNano: Miniaturisierte Analyseverfahren durch Nanotechnologie in Biochemie, Chemie und Physik

- 4. Bayerisch-Französisches Hochschulzentrum / BFHZ-CCUFB**
 - „UV electroluminescent diodes based on AlN/diamond heterojunctions. From materials to devices.“

- 5. Bayerisch-Kalifornisches Hochschulzentrum - BaCaTeC**
 - ”New Materials for Spintronics“

- 6. European Union**
 - COLLECT (Collective electronic states in nanostructures)
 - DRIVE (Diamond Research on Interfaces for Versatile Electronics)
 - EUROPEAN SYNCHROTRON RADIATION FACILITY (ESRF, Grenoble)
 - GANANO(New Generation of GaN-based sensor arrays for nano- and pico-fluidic systems for fast and reliable biomedical testing)
 - NEWTON (New Widely Tunable Lasers for Optical Networks)

- 7. DAAD**
 - Acciones Integradas Hispano-Alemanas – PPP mit Spanien
 - PROCOPE – PPP mit Frankreich

- 8. Office of Naval Research**
 - N00014-01-1-0242: “Modeling and simulation of semiconductor nanostructures”

- 9. Industry**
 - Degussa AG Düsseldorf, Germany:
“Funktionsschichten aus Silizium-Nanopartikeln“
 - EADS Deutschland GmbH, München, Germany:
„NANOS4 (Nano-structured solid-state gas sensors with superior performance)“
 - Fujitsu Laboratories of Europe Ltd., Hayes Park, UK:
“Bio-Nanotechnology”
 - ρ -BeSt, Innsbruck, Austria:
“Nano Diamond Network”:
 - Infineon, München, Germany:
„Zweidimensionale quantenmechanische Simulation“, „Quantenmechanische MOSFET-Simulation“
 - Osram Opto Semiconductors, Regensburg, Germany:
„Prozessierung von GaN Leuchtdioden“
 - Rhode & Schwarz, München, Germany:
„Zero-Bias Schottky-Diodes“
 - Siemens Power Generation, München, Germany:
„Integrierte Gassensoren und UV-Detektoren zur drahtlosen Überwachung von Verbrennungsprozessen“

Other collaborations and project partners:

RWTH Aachen, Arizona State University, University of California at Berkeley, TU Braunschweig, Universität Bremen, Wacker Siltronic Burghausen, MIT Cambridge, TU Darmstadt, TU Delft, Intune Dublin, Universität Duisburg, Universität Erlangen-Nürnberg, FHG IPM Freiburg, Vertilas Garching, General Electric Garching, Vertilas Garching, Walther Meißner Institut Garching, Gayton Photonics (UK), IMEC Gent, Universität Gießen, Universität Graz, Universität Hamburg, Universität Hannover, Foundation for Research and Technology-Hellas (FORTH) Heraklion, University of Crete Heraklion, City University of HongKong, TU Ilmenau, FZ Jülich, Institute of Nuclear Physics Krakow, Universität Leoben, Interuniversitair Micro-Electronica Centrum Leuven, Linköping University, Universität Linz, King's College London, Universidad Politecnica de Madrid, Universität Marburg, Fraunhofer Institut IZM München, Infineon München, LMU München, Rhode & Schwarz München, Siemens München, General Electric Finance Holding GmbH Neu-Isenburg, EADS Deutschland Ottobrunn, Universität Paderborn, Centre National de la Recherche Scientifique Paris, SNS Pisa, Institute of Physics Prague, Universität Regensburg, Weizmann Institute Rehovot, Università Rom II Tor Vergata, UCSB Santa Barbara, ρ -BeSt coating Hartstoffbeschichtungs GmbH Steinach, MPI FKF Stuttgart, Universität Stuttgart, University of Tokyo, Rensselaer Polytechnic Institute Troy, Diamond Research Center Tsukuba, National Institute of Materials Science Tsukuba, Universität Ulm, High Pressure Research Centre (Unipress) Warsaw, TopGaN Ltd. Warsaw, University of Warwick, TU Wien, Nanoplus Würzburg, Universität Würzburg, Bookham Zürich, ETH Zürich.

6. Publications

Amorphous and microcrystalline semiconductors – science and technology
 Proceedings of the 20th International Conference, August 25-29, 2003, Campos do Jordao, Brazil, ed. by F. Alvarez, I. Chambouleyron, M. Stutzmann, and P. Craig Taylor
 J. Non-Cryst. Sol. (2004)

Temperature-induced broadening of the emission lines from a quantum-dot nanostructure
 V. M. Apalkov, T. Chakraborty, N. Ulbrich, D. Schuh, J. Bauer, and G. Abstreiter
 Physica E **24**, 272-277 (2004)

Vertical-mode dependence of coupling between an electron waveguide and reservoirs with two occupied subbands
 G. Apetrii, S. F. Fischer, U. Kunze, D. Schuh, and G. Abstreiter
 Physica E **22**, 398-401 (2004)

Long-range ordered self-assembled InAs quantum dots epitaxially grown on (110) GaAs
 J. Bauer, D. Schuh, E. Uccelli, R. Schulz, A. Kress, F. Hofbauer, J. J. Finley, and G. Abstreiter
 Appl. Phys. Lett. **85**, 4750-4752 (2004)

Paramagnetic defects of silicon nanowires
 A. Baumer, M. Stutzmann, M. S. Brandt, F. C. K. Au, and S. T. Lee
 Appl. Phys. Lett. **85**, 943-945 (2004)

Long relaxation times of holes in Si/SiGe quantum cascade structures with a diagonal intersubband transition
 I. Bormann, K. Brunner, S. Hackenbuchner, H. Riedl, S. Schmult, W. Wegscheider, and G. Abstreiter
 Physica E **21**, 779-782 (2004)

Resonant Raman scattering of discrete hole states in self-assembled Si/Ge quantum dots
 D. Bougeard, P. H. Tan, M. Sabathil, P. Vogl, G. Abstreiter, and K. Brunner
 Physica E **21**, 312-316 (2004)

Passivation of Mn acceptors in GaMnAs
 M. S. Brandt, S. T. B. Gönnerwein, T. A. Wassner, F. Kohl, A. Lehner, H. Hübl, T. Graf, M. Stutzmann, A. Koeder, W. Schoch, and A. Waag
 Appl. Phys. Lett. **84**, 2277 (2004)

Spin-dependent transport in elemental and compound semiconductors and nanostructures

M. S. Brandt, S. T. B. Gönnerwein, T. Graf, H. Hübl, S. Lauterbach, and M. Stutzmann
 phys. stat. sol. (c) **1**, 2056-2078 (2004)

Photoreflectance studies of (Al)Ga- and N-face AlGaIn/GaN heterostructures

C. Buchheim, A.T. Winzer, R. Goldhahn, G. Gobsch, O. Ambacher, A. Link, M. Eickhoff, and M. Stutzmann
 Thin Solid Films **450**, 155 (2004)

Electron injection-induced effects in Mn-doped GaN

W. Burdett, O. Lopatiuk, L. Chernyak, M. Hermann, M. Stutzmann, and M. Eickhoff
 J. Appl. Phys. **96**, 3556-3558 (2004)

Tempern von aktiven Zonen aus GaInAsSb/AlGaAsSb MQWs für GaSb-VCSEL

S. Dachs, O. Dier, M. Grau, C. Lauer, C. Lin, und M.-C. Amann
 in: Deutscher MBE-Workshop 2004, Braunschweig, Germany (2004)

Selective and non-selective wet-chemical etchants for GaSb-based materials

O. Dier, C. Lin, M. Grau, and M.-C. Amann
 Semicond. Sci. Technol. **19**, 1250-1253 (2004)

Tunnel junctions for Ohmic intra-device contacts on GaSb-substrates

O. Dier, M. Sterkel, M. Grau, C. Lin, C. Lauer, and M.-C. Amann
 Appl. Phys. Lett. **85**, 2388-2389 (2004)

Tunnel junctions for Ohmic intra-device contacts on GaSb-substrates

O. Dier, C. Lauer, M. Sterkel, C. Lin, M. Grau, and M.-C. Amann
 in: Deutscher MBE-Workshop 2004, Braunschweig, Germany (2004)

Anomalous spin dephasing in (110) GaAs quantum wells: Anisotropy and intersubband effects

S. Dohrmann, D. Hagele, J. Rudolph, M. Bichler, D. Schuh, and M. Oestreich
 Phys. Rev. Lett. **93**, 147405 (2004)

Electronic transport through a quantum dot network

A. Dorn, T. Ihn, K. Ensslin, W. Wegscheider, and M. Bichler
 Phys. Rev. B **70**, 205306 (2004)

Dynamics of optically stored charges in InGaAs quantum dots

Y. Ducommun, M. Kroutvar, J. J. Finley, M. Bichler, A. Zrenner, and G. Abstreiter
 Physica E **21**, 886-891 (2004)

Redistribution dynamics of optically generated charges in In(Ga)As/GaAs self-assembled quantum dots

Y. Ducommun, M. Kroutvar, M. Reimer, M. Bichler, D. Schuh, G. Abstreiter, and J. J. Finley
 Appl. Phys. Lett. **85**, 2592-2594 (2004)

Piezoresistive properties of single crystalline, polycrystalline, and nanocrystalline n-type 3C-SiC

M. Eickhoff, M. Möller, G. Kroetz, and M. Stutzmann
 J. Appl. Physics **96**, 2872-2877 (2004)

Influence of crystal quality on the electronic properties of n-type 3C-SiC grown by low temperature low pressure chemical vapour deposition

M. Eickhoff, H. Möller, J. Stoemenos, S. Zappe, G. Kroetz, and M. Stutzmann
 J. Appl. Phys. **95**, 7908-7917 (2004)

Influence of crystal defects on the piezoresistive properties of 3C-SiC

M. Eickhoff and M. Stutzmann
 J. Appl. Phys. **96**, 2878-2888 (2004)

Resonant tunneling between parallel 1D quantum wires and adjoining 2D electron reservoirs

F. Ertl, S. Roth, D. Schuh, M. Bichler, and G. Abstreiter
 Physica E **22**, 292-295 (2004)

Atomically precise modulated two-dimensional electron gas exhibiting stable negative differential resistance

T. Feil, B. Rieder, W. Wegscheider, J. Keller, M. Bichler, D. Schuh, and G. Abstreiter
 Physica E **22**, 733-736 (2004)

Transport in weakly and strongly modulated two-dimensional electron systems realized by cleaved-edge-overgrowth

T. Feil, R. A. Deutschmann, W. Wegscheider, M. Rother, D. Schuh, M. Bichler, G. Abstreiter, B. Rieder, and J. Keller
 phys. stat. sol. **1**, 2111 (2004)

Systematic reduction of the permanent exciton dipole for charged excitons in individual self-assembled InGaAs quantum dots

J. J. Finley, M. Sabathil, R. Oulton, A. I. Tartakovskii, D. J. Mowbray, M. S. Skolnick, S. Liew, M. Migliorato, M. Hopkinson, and P. Vogl
 Physica E **21**, 199-203 (2004)

Quantum-confined Stark shifts of charged exciton complexes in quantum dots

J. J. Finley, M. Sabathil, P. Vogl, G. Abstreiter, R. Oulton, A. I. Tartakovskii, D. J. Mowbray, M. S. Skolnick, S. L. Liew, A. G. Cullis, and M. Hopkinson
 Phys. Rev. B **70**, 201308 (2004)

New anisotropic behaviour of quantum Hall resistance in (110) GaAs heterostructures at mK temperatures and fractional filling factors

F. Fischer, M. Grayson, E. Schuberth, D. Schuh, M. Bichler, and G. Abstreiter
Physica E **22**, 108-110 (2004)

High-temperature ($T=490\text{K}$) operation of $5.8\mu\text{m}$ quantum cascade lasers with InP/GaInAs waveguides

A. Friedrich, G. Scarpa, G. Böhm, and M.-C. Amann
Electron. Lett. **40**, 1416-1417 (2004)

Very high temperature operation of $\sim 5.75\mu\text{m}$ quantum-cascade lasers

A. Friedrich, G. Scarpa, G. Böhm, and M.-C. Amann
in: Proc. of 27th International Conference on the Physics of Semiconductors (ICPS), Flagstaff, USA (2004)

Kondo effect in a many-electron quantum ring

A. Fuhrer, T. Ihn, K. Ensslin, W. Wegscheider, and M. Bichler
Phys. Rev. Lett. **93**, 176803 (2004)

Quantum rings as phase coherent detectors

A. Fuhrer, M. Sigrist, L. Meier, T. Ihn, K. Ensslin, W. Wegscheider, and M. Bichler
Physica E **25**, 303-312 (2004)

Diamond-based nanoelectronics: physics and applications

J. A. Garrido, A. Härtl, E. Schmich, J. Hernando, and M. Stutzmann
in: Proc. of the 12th Int. Symp. "Nanostructures: Physics and Technology", St. Petersburg, June 21-25 (2004), Ioffe Institute, St. Petersburg, p. 395-397

Optical properties of Mn-doped GaN

O. Gelhausen, E. Malguth, M. R. Phillips, E. M. Goldys, M. Strassburg, A. Hoffmann, T. Graf, M. Gjukic, and M. Stutzmann
in: Mat. Res. Soc. Symp. Proc. **798** (2004), p. Y8.5.1-6

Aluminum-induced crystallization of amorphous silicon-germanium thin films

M. Gjukic, M. Buschbeck, R. Lechner, and M. Stutzmann
Appl. Phys. Lett. **85**, 2134-2135 (2004)

Hydrogen and magnetism in $\text{Ga}_{1-x}\text{Mn}_x\text{As}$

S. T. B. Gönnenwein, T. A. Wassner, H. Hübl, A. Koeder, W. Schoch, A. Waag, J. B. Philipp, M. Opel, R. Gross, M. Stutzmann, and M. S. Brandt
in: Adv. in Solid State Phys., ed. by B. Kramer, Berlin-Heidelberg: Springer Verlag (2004) **44**, p. 453-465

Hydrogen control of ferromagnetism in a dilute magnetic semiconductor

S. T. B. Gönnenwein, T. A. Wassner, H. Hübl, M. S. Brandt, J. B. Philipp, M. Opel, R. Gross, A. Köder, W. Schoch, and A. Waag
Phys. Rev. Lett. **92**, 227202 (2004)

Optical and structural characteristics of virtually unstrained bulk-like GaN

D. Gogova, A. Kasic, H. Larsson, B. Pécz, R. Yakimova, B. Magnusson, B. Monemar, F. Tuomisto, K. Saarinen, C. Miskys, M. Stutzmann, C. Bundesmann, and M. Schubert
 Jpn. J. Appl. Phys. **43**, 1264-1268 (2004)

Room-temperature operation of GaInAsSb-AlGaAsSb quantum well lasers in the 2.2 to 3 μm wavelength range

M. Grau, C. Lin, O. Dier, and M.-C. Amann

in: Conference on Lasers and Electro-Optics (CLEO), San Francisco, USA (2004)

Room- temperature 2.81 μm continuous wave operation of GaInAsSb/AlGaAsSb-laser

M. Grau, C. Lin, and M.-C. Amann

Photon. Technol. Lett. **16**, 383-385 (2004)

GaInAsSb/AlGaAsSb-lasers in the wavelength range between 2.73 μm and 2.93 μm

M. Grau, C. Lin, O. Dier, and M.-C. Amann

Physica **E 20**, 507-510 (2004)

Electronic correlations at the edge of a quantum Hall liquid

M. Grayson

in: Proc. of the Int. School of Phys. "Enrico Fermi", Course CLVII, ed. by

G. F. Giuliani and G. Vignale, IOS Press, Amsterdam, (2004), p. 515-526

Experimental demonstration of a sharp quantum Hall edge

M. Grayson, M. Huber, M. Rother, W. Bichler, W. Wegscheider, M. Bichler, and G. Abstreiter

Physica E **25**, 212-218 (2004)

Quantum Hall effect in a two-dimensional electron system bent by 90°

M. Grayson, D. Schuh, M. Bichler, M. Huber, G. Abstreiter, L. Hoeppel, J. Smet, and K. v. Klitzing

Physica E **22**, 181-184 (2004)

Quantized transport in ballistic rectifiers: sign reversal and step-like output

S. de Haan, A. Lorke, J. P. Kotthaus, M. Bichler, and W. Wegscheider

Physica E **21**, 916-920 (2004)

Rectification in mesoscopic systems with broken symmetry: Quasiclassical ballistic versus classical transport

S. de Haan, A. Lorke, J. P. Kotthaus, W. Wegscheider, and M. Bichler

Phys. Rev. Lett. **92**, 056806 (2004)

Protein-modified nanocrystalline diamond thin films for biosensor applications

A. Härtl, E. Schmich, J. A. Garrido, J. Hernando, S.C.R. Catharino, S. Walter,

P. Feulner, A. Kromka, D. Steinmüller, and M. Stutzmann

Nature Materials **3**, 736 (2004)

Chirp and linewidth enhancement factor of 1.55 μ m VCSEL with buried tunnel junction
 H. Halbritter, R. Shau, F. Riemenschneider, B. Kögel, M. Ortsiefer, J. Rosskopf,
 G. Böhm, M. Maute, M.-C. Amann, and P. Meissner
 Electron. Lett. **40**, 1266-1267 (2004)

Vertical transport in group III-nitride heterostructures and application in AlN/GaN resonant tunnelling diodes
 M. Hermann, E. Monroy, A. Helmann, B. Baur, M. Albrecht, B. Daudin, O. Ambacher,
 M. Stutzmann, and M. Eickhoff
 phys. stat. sol. (c) **1**, 2210-2227 (2004)

Study of pinholes and nanotubes in AlInGaN films by cathodoluminescence and atomic force microscopy
 M. Herrera, A. Cremades, J. Piqueras, M. Stutzmann, and O. Ambacher
 J. Appl. Phys. **95**, 5305-5310 (2004)

High-speed vertical-cavity laser diodes at 1.55 μ m
 W. Hofmann, N.H. Zhu, M. Ortsiefer, R. Shau, J. Rosskopf, G. Böhm, C. Quian,
 F. Köhler, M. Maute, C. Lauer, and M.-C. Amann
 in: Proc. of the Third Joint Symposium on Opto- and Microelectronic Devices and
 Circuits (SODC), Wuhan, China (2004)

Probing the electrostatics of integer quantum Hall edges with momentum-resolved tunnel spectroscopy
 M. Huber, M. Grayson, D. Schuh, M. Bichler, W. Biberacher, W. Wegscheider, and
 G. Abstreiter
 Physica E **22**, 164-167 (2004)

Tunable InP-based buried heterostructure lasers with vertically integrated Mach-Zehnder interferometer (VMZ)
 Th. Jacke, R. Todt, and M.-C. Amann
 in: Proc. of SPIE **5452** (2004), p. 174-182

Widely tunable lasers with vertically integrated Mach-Zehnder interferometer
 Th. Jacke, R. Todt, R. Meyer, M. Maute, and M.-C. Amann
 in: Proc. of IEEE 19th International Semiconductor Laser Conference 2004,
 Matsue-shi, Japan (2004), p. 473-476

Enhanced carrier lifetime for the tuning region in tunable laser diodes based on type-II quantum wells
 Th. Jacke, G. Rösel, M. Grau, R. Meyer, and M.-C. Amann
 in: Proc. of the Third Joint Symposium on Opto- and Microelectronic Devices and
 Circuits (SODC), Wuhan, China (2004)

The doping efficiency in a-SiO_x:H

A. Janotta, R. Janssen, M. Schmidt, T. Graf, M. Stutzmann, L. Görgens, A. Bergmaier, G. Dollinger, C. Hammerl, S. Schreiber, and B. Stritzker
 Phys. Rev. B **69**, 115206 (2004)

Light-induced modification of a-SiO_x (I): Metastability

A. Janotta, Y. Dikce, S. Linder, M. Schmidt, R. Janssen, and M. Stutzmann
 J. Appl. Phys. **95**, 4046 (2004)

Light-induced modification of a-SiO_x (II): Laser crystallization

A. Janotta, Y. Dikce, M. Schmidt, C. Eisele, M. Stutzmann, M. Luysberg, and L. Houben
 J. Appl. Phys. **95**, 4060 (2004)

Hole spin-relaxation in quantum wells from saturation of inter-subband absorption

J. Kainz, P. Schneider, S. D. Ganichev, U. Rössler, W. Wegscheider, D. Weiss, W. Prettl, V. V. Bel'kov, L. E. Golub, and D. Schuh
 Physica E **22**, 418-421 (2004)

Two-dimensional quantum-mechanical modeling for strained silicon channels of double-gate MOSFETs

K. Kim, O. Kwon, J. Seo, T. Won, S. Birner, R. Oberhuber, and A. Trellakis
 J. Korean Phys. Soc. **45**, S909 (2004)

Two-dimensional quantum effects and structural optimization of FinFETs with two-dimensional Poisson-Schrodinger solvers

K. Kim, O. Kwon, J. Seo, T. Won, S. Birner, and A. Trellakis
 J. Korean Phys. Soc. **45** (5), 1384 (2004)

Capture and release of photonic images in a quantum well

J. Krauss, J. P. Kotthaus, A. Wixforth, M. Hanson, D. C. Driscoll, A. C. Gossard, D. Schuh, and M. Bichler
 Appl. Phys. Lett. **85**, 5830-5832 (2004)

Photoluminescence of one-dimensional electron gases in cleaved-edge overgrowth quantum wires

C. Kristukat, A. R. Goni, M. Bichler, W. Wegscheider, G. Abstreiter, and C. Thomsen
 phys. stat. sol. (b) **241**, No. 5, 1041-1045 (2004)

Optically programmable electron spin memory using semiconductor quantum dots

M. Kroutvar, Y. Ducommun, D. Heiss, M. Bichler, D. Schuh, G. Abstreiter, and J. J. Finley
 Nature **432**, 81-84 (2004)

InP-based long-wavelength vertical-cavity surface-emitting lasers with buried tunnel junction

C. Lauer, M. Ortsiefer, R. Shau, J. Roskopf, G. Böhm, R. Meyer, and M.-C. Amann
phys. stat. sol. (c) **1**, 2183–2209 (2004)

80°C continuous-wave operation of 2.01 μm wavelength InGaAlAs–InP vertical-cavity surface-emitting lasers

C. Lauer, M. Ortsiefer, R. Shau, J. Roskopf, G. Böhm, E. Rönneberg, F. Köhler, and M.-C. Amann
Photon. Technol. Lett. **16**, 2209–2211 (2004)

Thin polycrystalline SiGe films by aluminium-induced layer exchange

R. Lechner, M. Buschbeck, M. Gjukic, and M. Stutzmann
phys. stat. sol. (c) **1**, 1131–1143 (2004)

Advanced study of various characteristics found in RHEED patterns during the growth of InAs quantum dots on GaAs (001) substrate by molecular beam epitaxy

J. W. Lee, D. Schuh, M. Bichler, and G. Abstreiter
Appl. Surface Science **228**, 306–312 (2004)

Low threshold room-temperature continuous-wave operation of 2.24–3.04 μm GaInAsSb/AlGaAsSb quantum-well laser

C. Lin, M. Grau, O. Dier, and M.-C. Amann
Appl. Phys. Lett. **84**, 5088–5090 (2004)

Time and current dependencies of transport at the $\nu=2/3$ phase transition in narrow quantum wells

J. G. S. Lok, S. Kraus, O. Stern, W. Dietsche, K. v. Klitzing, W. Wegscheider, M. Bichler, and D. Schuh
Physica E **22**, 138–141 (2004)

Liquid phase sensors based on chemically functionalized GaAs/AlGaAs heterostructures

S. M. Lubber, K. Adlkofer, U. Rant, A. Ulmann, A. Götzhäuser, M. Grunze, D. Schuh, M. Tanaka, M. Tornow, and G. Abstreiter
Physica E **21**, 1111–1115 (2004)

Advances in the theory of electronic structures of semiconductors

J. A. Majewski, S. Birner, A. Trellakis, M. Sabathil, and P. Vogl
phys. stat. sol. (c) **1**, 2003 (2004)

Contact block reduction method and its application to a 10 nm MOSFET device

D. Mamaluy, A. Mannargudi, D. Vasileska, M. Sabathil, and P. Vogl
Semicond. Sci. Technol. **19**, S118 (2004)

Localization of fractionally charged quasi-particles

J. Martin, S. Ilani, B. Verdene, J. Smet, V. Umansky, D. Mahalu, D. Schuh, G. Abstreiter, and A. Yacoby
 Science **305**, 980-983 (2004)

Single-electron effects in a coupled dot-ring system

L. Meier, A. Fuhrer, T. Ihn, K. Ensslin, W. Wegscheider, and M. Bichler
 Phys. Rev. B **69**, 241302 (2004)

Coulomb drag as a probe of the nature of compressible states in a magnetic field

K. Muraki, J. G. S. Lok, S. Kraus, W. Dietsche, K. v. Klitzing, D. Schuh, M. Bichler, and W. Wegscheider
 Phys. Rev. Lett. **92**, 246801 (2004)

Two-dimensional electron gas recombination in undoped AlGaIn/GaN heterostructures

G. Martinez-Criado, C. Miskys, U. Karrer, O. Ambacher, and M. Stutzmann
 Jpn. J. Appl. Phys. **43**, 3360-3366 (2004)

Direct observation of Mn clusters in GaN by X-ray scanning microscopy

G. Martinez-Criado, A. Somogyi, M. Hermann, M. Eickhoff, and M. Stutzmann
 Jpn. J. Appl. Phys. **43**, L695-L697 (2004)

Long-wavelength VCSELS

M. Maute and M.-C. Amann

in: Proc. of 16th International Conference on Indium Phosphide and Related Materials (IPRM), Kagoshima, Japan (2004), p. 695-699

Novel 2-chip-concept for micro-mechanically tunable long-wavelength VCSELS for the 1.55 μ m wavelength range

M. Maute, M.-C. Amann, M. Ortsiefer, R. Shau, F. Riemenschneider, and P. Meissner
 in: Proc. of SPIE Conference Photonics Europe 2004, Strasbourg, France (2004), p. 240-248

Long wavelength VCSEL for optical access networks

M. Maute, M.-C. Amann, J. Vathke, D. Kassner, M. Ortsiefer, and R. Shau
 in: Proc. of 13th International Plastic Optical Fibres Conference (POF) 2004, Nürnberg, Germany (2004), p. 19-26

Micro-mechanically and widely tunable long-wavelength VCSELS

M. Maute, G. Böhm, M.-C. Amann, F. Riemenschneider, H. Halbritter, and P. Meissner
 in: Proc. of IEEE 19th International Semiconductor Laser Conference 2004, Matsue-shi, Japan (2004)

Micro-mechanically tunable long-wavelength VCSELS

M. Maute, G. Böhm, O. Dier, F. Riemenschneider, P. Meissner, M. Ortsiefer, R. Shau, and M.-C. Amann

in: IEEE Laser Workshop, San Francisco, USA (2004)

Micro-mechanically tunable long wavelength VCSEL with buried tunnel junction

M. Maute, F. Riemenschneider, G. Böhm, H. Halbritter, M. Ortsiefer, R. Shau, P. Meissner, and M.-C. Amann

Electron. Lett. **40**, 430-431 (2004)

Structural and interface properties of an AlN diamond ultraviolet light emitting diode

C. R. Miskys, J. A. Garrido, G. Vogg, M. Hermann, M. Eickhoff, C. E. Nebel, and M. Stutzmann

Appl. Phys. Lett. **85**, 3699 (2004)

Wurtzite to cubic polytype inversion of N-face GaN by Mg doping

E. Monroy, M. Hermann, E. Sarigiannidou, T. Andreev, P. Holliger, S. Monnoye, H. Mank, B. Daudin, and M. Eickhoff

J. Appl. Phys. **96**, 3709 (2004)

New widely tunable edge-emitting laser diodes at 1.55 μ m developed in the European IST-project NEWTON

G. Morthier, R. Laroy, I. Christiaens, R. Todt, Th. Jacke, M.-C. Amann, J.-O. Wesstrom, S. Hammerfeldt, T. Mullane, N. Ryan, and M. Todd

in: Proc. of SPIE Conference Asia-Pacific Optical Communications 2004, Beijing, China (2004)

High-temperature operated field-effect gas sensors

G. Müller, J. Schalwig, P. Kreisl, A. Helwig, E. Obermeier, O. Weidemann, M. Stutzmann, and M. Eickhoff

Encyclopedia of SENSORS (2004)

Oxidation lift-off method for layer transfer of GaAs-AlAs-based structures

S. Oktyabrsky, A. Katsnelson, V. Tokranov, R. Todt, and M. Yakimov

Appl. Phys. Lett. **85**, 151-153 (2005)

Electric field control of exciton states in quantum dot molecules

G. Ortner, M. Bayer, A. Kress, A. Forchel, Y. B. Lyanda-Geller, and T. L. Reinecke
Physica E **21**, 171-174 (2004)

Temperature-induced carrier escape processes studied in absorption of individual In_xGa_{1-x}As quantum dots

R. Oulton, A. I. Tartakovskii, A. Ebbens, J. Cahill, J. J. Finley, D. J. Mowbray, M. S. Skolnick, and M. Hopkinson

Phys. Rev. B **69**, 155323 (2004)

Electronic and optical properties of [N11] grown nanostructures

M. Povolotskiy, A. Di Carlo, and S. Birner
 phys. stat. sol. (c) **1**, 1511 (2004)

Tuning the piezoelectric fields in quantum dots: microscopic description of dots grown on (N11) surfaces

M. Povolotskiy, A. Di Carlo, P. Lugli, S. Birner, and P. Vogl
 IEEE Transactions on Nanotechnology **3**, 124 (2004)

Non-linear optical properties of InGaAs/AlGaAs nanostructures grown on (N11) surfaces

M. Povolotskiy, J. Gleize, A. Di Carlo, P. Lugli, S. Birner, P. Vogl, D. Alderighi, M. Gurioli, A. Vinattieri, M. Colocci, S. Sanguinetti, and R. Nötzel
 Semicond. Sci. Technol. **19**, S351 (2004)

Compact expression for the angular dependence of tight-binding Hamiltonian matrix elements

A. V. Podolskiy and P. Vogl
 Phys. Rev. B **69**, 233101 (2004)

Dynamic electrical switching of DNA layers on a metal surface

U. Rant, K. Arinaga, S. Fujita, N. Yokoyama, G. Abstreiter, and M. Tornow
 Nano Lett. **4**, 2441-2445 (2004)

Structural properties of oligonucleotide monolayers on gold surfaces probed by fluorescence investigations

U. Rant, K. Arinaga, S. Fujita, N. Yokoyama, G. Abstreiter, and M. Tornow
 Langmuir **20**, 10086-10092 (2004)

Hydrogenated diamond surfaces studied by atomic and Kelvin force microscopy

B. Rezek, C. E. Nebel, and M. Stutzmann
 Diam. & Rel. Mat. **13**, 740-745 (2004)

Continuously tunable long-wavelength MEMS-VCSEL with over 40 nm tuning range

F. Riemenschneider, M. Maute, H. Halbritter, G. Böhm, M.-C. Amann, and P. Meissner
 Photon. Technol. Lett. **16**, 2212-2214 (2004)

A new concept for micro-mechanically tunable long wavelength VCSELs

F. Riemenschneider, M. Maute, H. Halbritter, M. Ortsiefer, R. Shau, M.-C. Amann, and P. Meissner
 in: Conference on Lasers and Electro-Optics (CLEO), San Francisco, USA (2004)

AlGaAsSb / AlGaInAs type-II superlattices for tuning regions in tunable laser diodes

G. Rösel, Th. Jacke, M. Grau, R. Meyer, and M.-C. Amann
 in: Proc. of SPIE **5452** (2004), p. 163-173

Enhanced tuning efficiency in tunable laser diodes using type-II superlattices

G. Rösel, Th. Jacke, M. Grau, R. Meyer, and M.-C. Amann

Photon. Technol. Lett. **16**, 738-740 (2004)*Fabrication of double quantum dots by combining AFM and e-beam lithography*

M. C. Rogge, C. Fühner, U. F. Keyser, M. Bichler, G. Abstreiter, W. Wegscheider, and R. J. Haug

Physica E **21**, 483-486 (2004)*Prediction of a realistic quantum logic gate using the contact block reduction method*

M. Sabathil, D. Mamaluy, and P. Vogl

Semicond. Sci. Technol. **19**, S137 (2004)*Non-equilibrium electronic distribution within one period of InP-based quantum cascade lasers*

G. Scarpa, P. Lugli, N. Ulbrich, G. Abstreiter, and M.-C. Amann

Semicond. Sci. Technol. **19**, 342-344 (2004)*Mid infrared emission of quantum wire cascade structures*

S. Schmult, I. Keck, T. Herrle, W. Wegscheider, A. P. Mayer, M. Bichler, D. Schuh, and G. Abstreiter

Physica E **21**, 223-229 (2004)*Spin relaxation times of two-dimensional holes from spin sensitive bleaching of intersubband absorption*

P. Schneider, J. Kainz, S. D. Ganichev, S. N. Danilov, U. Rössler, W. Wegscheider, D. Weiss, W. Prettl, V. V. Bel'kov, M. M. Glazov, L. E. Golub, and D. Schuh

J. Appl. Phys. **96**, 420-424 (2004)*Heterostructures overgrown on GaAs corner substrates*

D. Schuh, M. Grayson, M. Bichler, and G. Abstreiter

Physica E **23**, 293-297 (2004)*How to probe a fractionally charged quasihole?*

C. Schuller, K.-B. Broocks, P. Schröter, Ch. Heyn, D. Heitmann, M. Bichler, W. Wegscheider, T. Chakraborty, and V. M. Apalkov

Physica E **22**, 131-134 (2004)*Charged excitons in the quantum hall regime*

C. Schuller, K. B. Broocks, P. Schroter, C. Heyn, D. Heitmann, M. Bichler, W. Wegscheider, V. M. Apalkov, and T. Chakraborty

Acta Physica Polonica A **106**, 341-353 (2004)*Morphology and optical properties of InAs(N) quantum dots*

O. Schumann, L. Geelhaar, H. Riechert, H. Cerva, and G. Abstreiter

J. Appl. Phys. **96**, 2832-2840 (2004)

Optical properties of low-dimensional semiconductor systems fabricated by cleaved edge overgrowth

R. Schuster, H. Hajak, M. Reinwald, W. Wegscheider, G. Schedelbeck, S. Sedlmaier, M. Stopa, S. Birner, P. Vogl, J. Bauer, D. Schuh, M. Bichler, and G. Abstreiter
phys. stat. sol. (c) **1**, 2028 (2004)

Strongly confined quantum wire states in strained T-shaped GaAs/InAlAs structures

R. Schuster, H. Hajak, M. Reinwald, W. Wegscheider, D. Schuh, M. Bichler, and G. Abstreiter
Physica E **21**, 236-240 (2004)

Strong charge carrier confinement in purely strain induced GaAs/InAlAs single quantum wires

R. Schuster, H. Hajak, M. Reinwald, W. Wegscheider, D. Schuh, M. Bichler, and G. Abstreiter
Appl. Phys. Lett. **85**, 3672-3674 (2004)

Long-wavelength InP-based VCSELs with buried tunnel junctions: properties and applications

R. Shau, M. Ortsiefer, J. Roskopf, G. Böhm, C. Lauer, M. Maute, and M.-C. Amann
in: Proc. of SPIE **5364**, 1-15 (2004)

Temperature-dependent electric fields in GaN Schottky diodes studied by electro-reflectance

S. Shokhovets, D. Fuhrmann, R. Goldhahn, G. Gobsch, O. Ambacher, M. Hermann, and M. Eickhoff
Thin Solid Films **450**, 163 (2004)

Transmission phase through two quantum dots embedded in a four-terminal quantum ring

M. Sigrist, A. Fuhrer, T. Ihn, K. Ensslin, W. Wegscheider, and M. Bichler
Physica E **22**, 530-533 (2004)

Magnetic-field-dependent transmission phase of a double-dot system in a quantum ring

M. Sigrist, A. Fuhrer, T. Ihn, K. Ensslin, S. E. Ulloa, W. Wegscheider, and M. Bichler
Phys. Rev. Lett. **93**, 066802 (2004)

Anomalous-filling-factor-dependent nuclear-spin polarization in a 2D electron system

J. M. Smet, R. A. Deutschmann, F. Ertl, W. Wegscheider, G. Abstreiter, and K. v. Klitzing
Phys. Rev. Lett. **92**, 086802 (2004)

Improved 3C-SiC films epitaxially grown on Si by flash lamp processing

J. Stoemenos, D. Panknin, M. Eickhoff, V. Heera, and W. Skorupa
J. Electrochem. Soc. **151**, G136 (2004)

Novel AlGaIn heterostructures for UV sensors and LEDs

M. Stutzmann

in: UV Solid-State Light Emitters and Detectors, ed. by M. S. Shur and A. Zukauskas, Kluwer (2004), p. 143-159 (Nato Adv. Study Inst., Vilnius - June 2003)

*Observation of electrostatically released DNA from gold electrodes with controlled threshold voltages*S. Takeishi, U. Rant, T. Fujiwara, K. Buchholz, T. Usuki, K. Arinaga, K. Takemoto, Y. Yamaguchi, M. Tornow, S. Fujita, G. Abstreiter, and N. Yokoyama
J. Chem. Phys. **120**, 5501-5504 (2004)*Raman scattering of folded acoustic phonons in self-assembled Si/Ge dot superlattices*P. H. Tan, D. Bougeard, G. Abstreiter, and K. Brunner
Appl. Phys. Lett. **84**, 2632-2634 (2004)*Design and fabrication of widely tunable twin-guide laser diodes*R. Todt, Th. Jacke, R. Meyer, M.-C. Amann, R. Laroy, and G. Morthier
in: Semiconductor and Integrated Opto-Electronics Conference (SIOE), Cardiff, UK (2004)*Tunable twin-guide laser diodes for wide wavelength tuning at 1.55 μ m*R. Todt, Th. Jacke, R. Meyer, M.-C. Amann, R. Laroy, and G. Morthier
in: Proc. of SPIE Conference Optics East 2004, Philadelphia, USA (2004)*Tuning performance of widely tunable twin-guide laser diodes*R. Todt, Th. Jacke, R. Meyer, M.-C. Amann, R. Laroy, and G. Morthier
in: Proc. of 28th WOCS-DICE, Smolenice Castle, Slovakia (2004), p. 99-100*Wide wavelength tuning of sampled grating tunable twin-guide laser diodes*R. Todt, Th. Jacke, R. Meyer, R. Laroy, G. Morthier, and M.-C. Amann
Electron. Lett. **40**, 1491-1492 (2004)*Wide wavelength tuning of sampled-grating tunable twin-guide laser diodes*R. Todt, Th. Jacke, R. Meyer, M.-C. Amann, R. Laroy, and G. Morthier
in: European Semiconductor Laser Workshop 2004, Säröhus, Sweden*Directional effects on bound quantum states for trench oxide quantum wires on (100)-silicon*A. Trellakis and U. Ravaioli
Solid-State Electronics **48**, 367 (2004)*High quality heteroepitaxial AlN films on diamond*G. Vogg, C. R. Miskys, J. A. Garrido, M. Hermann, M. Eickhoff, and M. Stutzmann
J. Appl. Phys. **96**, 895-902 (2004)

Single-electron-phonon interaction in a suspended quantum dot phonon cavity

E. M. Weig, R. H. Blick, T. Brandes, J. Kirschbaum, W. Wegscheider, M. Bichler, and J. P. Kotthaus

Phys. Rev. Lett. **92**, 046804 (2004)

Activated transport in the separate layers that form the $\nu_T = 1$ excitation condensate

R. D. Wiersma, J. G. S. Lok, S. Kraus, W. Dietsche, K. v. Klitzing, D. Schuh, M. Bichler, H.-P. Tranitz, and W. Wegscheider

Phys. Rev. Lett. **93**, 266805 (2004)

Direct observation of controlled tunneling coupling in individual quantum dot molecules

Hubert J. Krenner¹, Emily C. Clark, Michael Reimer, Matthias Sabathil, Dieter Schuh, Max Bichler, Gerhard Abstreiter, and Jonathan J. Finley

The realization of robust and scalable hardware for quantum information processing is one of the most challenging goals in modern solid-state physics. Single charge excitations (excitons) in semiconductor quantum dots represent a particularly attractive quantum bit (qubit) since they can be coherently manipulated using ultrafast laser pulses over time-scales much shorter than their decoherence time. However, for an isolated dot such approaches are fundamentally limited to one or two qubit operations with little or no prospects for further scalability. As a result, attention has recently shifted towards few dot nanostructures that have potential for building more complex quantum processors. One of the most promising systems for implementing two qubits is a "quantum dot molecule" (QDM) consisting of a vertically stacked pair of InGaAs islands formed via strain-driven self-assembly in a GaAs matrix. In order to explore the potential these systems provide for scalability and demonstration of quantum conditional logic, a fundamental prerequisite is the *controllable coupling* of individual QDMs.

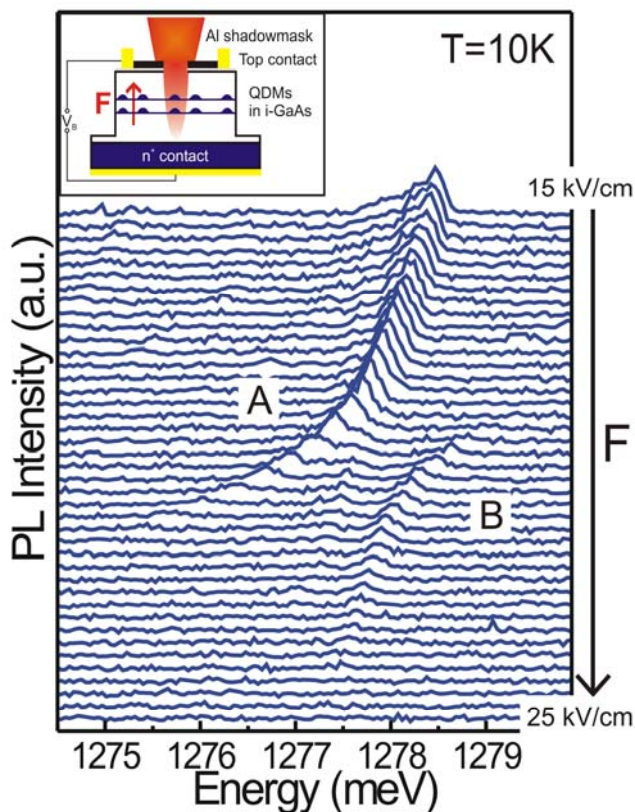


Fig. 1: PL spectra of an individual QDM as a function of the electric field (main panel). Schematic of the investigated device (inset).

In this report we present the first direct experimental observation of controlled tunneling coupling in individual QDMs. These findings are found to be in good agreement with theoretical calculations. The investigated samples contained two layers of stacked QDs nominally separated by a 10nm barrier were embedded at the center of the intrinsic region of an electrically active *n-i*- Schottky junction. This device enables us to tune the electric field (F) oriented along the stacking axis of the QDM via bias voltage applied between the n-contact and the Schottky-gate. The samples were processed into photodiodes equipped with opaque shadowmasks with sub- μm -sized apertures for isolation of individual QDMs, as shown schematically in the inset of Fig. 1.

The sample was mounted in a He-flow cryostat and we performed electric field dependent low-temperature ($T=10\text{K}$) μ -photoluminescence (PL). Carriers were generated non-

¹phone: +49-89-289-12736, fax: +49-89-3206620, email: krenner@wsi.tum.de

resonantly using a HeNe laser and the PL emitted by the QDMs was dispersed in a 0.9m triple monochromator and detected by a N_2 -cooled CCD detector. Figure 1 shows electric field dependent PL spectra of a single QDM at low excitation density, where the QDM is occupied by only one electron-hole pair (exciton). Two exciton branches, A and B, are resolved and show a clear anti-crossing as F is tuned.

The extracted spectral positions and the relative intensities of branches A and B, as a function of F , are shown in Fig. 2 together with the energetic splitting ΔE . The minimum splitting and equal relative intensities occur at the same electric field manifesting the anti-crossing.

To explain this experimental observation we performed realistic theoretical calculations of the exciton absorption spectrum of QDMs under electric field perturbations.

In QDMs two exciton species can be distinguished: Spatially *direct* (e and h in the same QD) and *indirect* (e and h in different QDs). Direct excitons are optically active due to their high e - h overlap whereas indirect excitons are not optically active. Additionally they differ in the excitonic dipole moment: The dipole moment of direct excitons is similar to single QDs. In contrast, indirect excitons have a much larger dipole moment given by the inter-QD separation $p_{ind} = e \cdot d_{QD/QD}$. Therefore, the Stark shift, given by $\Delta E = p \cdot F$, is weak and quadratic for direct excitons and strong and linear for indirect excitons. This leads to an independent tuning of these exciton species by the electric field. With increasing F the indirect exciton with the hole localized in the upper QD shifts towards the direct exciton localized in the upper QD. At the resonance field the electron part of the exciton wavefunction hybridizes into bonding and anti-bonding molecular states split by the coupling energy giving rise to the observed anti-crossing. For further increasing F the nature of the ground-state develops from direct to indirect character leading to the pronounced quenching behavior of the PL signal of branch A. The calculated Stark shifts for a QDM (lines in Fig. 2(a)) are found to be in good agreement with experiment. Furthermore, coupling energies of eight different QDMs indicate a mean QD distance of ~ 9 nm corresponding well with the nominal separation of 10nm set during growth.

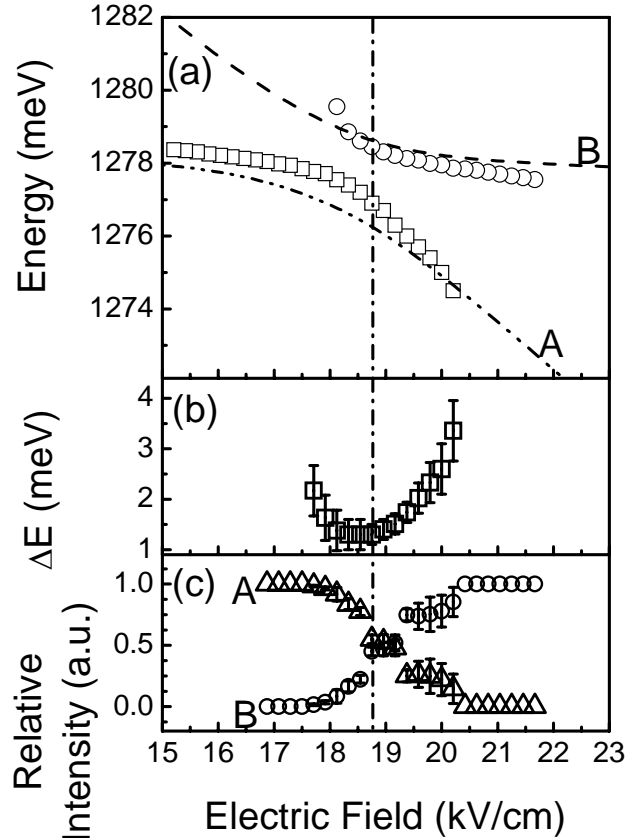


Fig. 2: (a) Experimental (symbols) and theoretical (lines) spectral positions, (b) energetic splitting and (c) relative intensities of A and B.

Ref: H. J. Krenner et al., Phys. Rev. Lett. **94**, 057402 (2005)